Title
Toward Resolving Model-Measurement Discrepancies of Radon Entry into Houses

Permalink
https://escholarship.org/uc/item/7zs9g65h

Author
Garbesi, K.

Publication Date
1993-06-01

LBL-34244
UC-350, 402

Lawrence Berkeley Laboratory
UNIVERSITY OF CALIFORNIA

ENERGY & ENVIRONMENT
DIVISION

Toward Resolving Model-Measurement Discrepancies of Radon Entry into Houses

K. Garbesi
(Ph.D. Thesis)

June 1993

**ENERGY & ENVIRONMENT
DIVISION**

Prepared for the U.S. Department of Energy under Contract Number DE-AC03-76SF00098

LBL-34244

TOWARD RESOLVING MODEL-MEASUREMENT DISCREPANCIES OF RADON ENTRY INTO HOUSES

Karina Garbesi
Ph.D. Thesis

Energy and Resources Group
University of California

and

Energy and Environment Division
Lawrence Berkeley Laboratory
University of California
Berkeley, CA 94720

June 1993

This work was supported by the Director, Office of Energy Research, Office of Health and Environmental Research, Environmental Sciences Division, and by the Assistant Secretary for Conservation and Renewable Energy, Office of Building and Community Systems, Building Systems and Materials Division of the U.S. Department of Energy (DOE), under Contract DE-AC03-76SF00098. The Association of Western Universities and DOE and the Switzer Foundation also provided fellowship support to the author.

Abstract

Analysis of the literature indicated that radon transport models significantly and consistently underpredict the advective entry into houses of soil-gas borne radon. Advective entry is the dominant mechanism resulting in high concentrations of radon indoors. My dissertation research investigated the source of the model-measurement discrepancy via carefully controlled field experiments conducted at an experimental basement located in natural soil in Ben Lomond, California.

Early experiments at the structure (Chapter II) confirmed the existence and magnitude of the model-measurement discrepancy, ensuring that it was not merely an artifact of inherently complex and poorly understood field sites. The measured soil-gas entry rate during structure depressurization was found to be an order of magnitude larger than predicted by a current three-dimensional numerical model of radon transport. The exact magnitude of the discrepancy depends on whether the arithmetic or geometric mean of the small-scale measurements of permeability is used to estimate the effective permeability of the soil. This factor is a critical empirical input to the model and was determined for the Ben Lomond site in the typical fashion using single-probe static depressurization measurements at multiple locations.

The remainder of the dissertation research tests a hypothesis to explain the observed discrepancy: that soil permeability assessed using relatively small-scale probe measurements (0.1 - 0.5 m) does not reflect bulk soil permeability for flows that is likely to occur at larger scales of several meters or more in real houses and in the test structure. The idea is that soil heterogeneity is of a nature that, as flows occur over larger scales, larger scales of heterogeneity are encountered that facilitate larger flux rates, resulting in a scale dependence of effective soil permeability.

In Chapter III I describe the development of a dual-probe dynamic pressure technique to measure soil permeability to air (and anisotropy of permeability) at various length scales. Preliminary field tests of the apparatus indicated that soil permeability was indeed scale dependent. In addition, the tests indicated that soil permeability was anisotropic, with horizontal permeability exceeding vertical by about a factor of 2. Laboratory soil column

experiments (Chapter IV) provided a partial test of the theory of dynamic-pressure signal propagation and of the interpretation of the field tests.

Chapter V describes a complete set of permeability measurements made over different length scales and spatial orientations at the Ben Lomond site. Over the range of scales investigated (0.1 - 3.5 m), effective permeability was found to increase by more than a factor of 40. The smaller-scale static permeability measurements were consistent with the dynamic measurements given the observed trend in permeability with scale. Given the new estimates of soil permeability for the ~3 m scale, the model over-estimation of the radon entry rate was reduced from a factor of ~9 to less than a factor of 2.5 (Chapter VI). Measurements of soil radon depletion with increasing structure depressurization provide an independent check of the larger-scale soil permeability, and corroborate the dynamic pressure measurements on that scale.

The finding of scale-dependent soil permeability to air has important implications for both modeling and field assessment of gas-phase transport of radon and other soil contaminants. With respect to modeling radon transport through soil, the implication is that scale dependence of permeability must be explicitly incorporated into the models unless it is known that the system operates only over a very narrow range of scales. The results also indicate that, in order for models to produce reasonably accurate results, considerably more information about the soil permeability field is required than was previously believed. A complete set of measurements covering the possible range of scales over which the system might operate is necessary. The technique developed in Chapter II is suitable for such a purpose.

to Marc

...without whom it would have

been significantly less fun!

Table of Contents

Chapter I. Introduction 1
- Overview 1
- Background 2
- Overview of Research 7
- Outline of Dissertation 7
- References 11
- Figures 17

Chapter II. Soil-Gas Entry into an Experimental Basement: Model-Measurement Comparisons and Seasonal Effects 18
- Synopsis 18
- Introduction 19
- Experimental Methods and Results 21
  - Site and Structure Characterization 21
  - Soil Moisture and Soil Air-Permeability 23
  - Pressure Field 25
  - Soil-Gas Entry 27
- Numerical Modeling and Comparison with Experiments 29
- Discussions 33
- Conclusions 35
- References 38
- Tables 41
- Figures 43
- Appendix: Effective Leakage Area of Structure 48

Chapter III. A Dynamic Pressure Technique for Estimating Permeability and Anisotropy of Soil to Air Flow Over Variable Length Scales 50
- Synopsis 50
- Introduction 51
- Theory 53
  - Model Development 53
  - Model Application 62

Field Test 63
Experimental Design 63
Data Analysis 65
Results 65
Discussion 67
Conclusions 70
References 72
Table 75
Figures 76
Appendix: Derivation of the Green's Function Solution for the One-Dimensional Diffusion Equation with a Time-Dependent Boundary Condition 82

Chapter IV. Soil Column Verification of the Dual-Probe Dynamic Pressure Technique for Measuring Soil Permeability to Air 89
Synopsis 89
Introduction 90
Theory 90
Model Development 90
Experimental Methods 97
Description of the Soil Column 97
Steady-state permeability measurements 98
Dynamic pressure measurements 99
Results 99
Discussion 100
Conclusions 101
Reference 102
Tables 103
Figure 105

Chapter V. A Field Study of the Scale Dependence of Soil Permeability to Air 106
Synopsis 106
Introduction 107
Experiment and Results 108

Discussion 110
Conclusions 112
References 114
Table 116
Figures 118

Chapter VI. Resolving the Model-Measurement Discrepancy of Radon and Soil-Gas Entry into the Experimental Structure 122
- Synopsis 122
- Introduction 123
- Methods 124
  - Experimental 124
  - Numerical Modeling 125
- Results 128
- Discussion 132
- Conclusions 133
- References 135
- Tables 137
- Figures 141
- Appendix: Diffusion as a source of ^{222}Rn in the Ben Lomond West Structure 148

Chapter VII. Conclusions 158
- Overview 158
- The Dual-Probe Dynamic Pressure Technique 159
- Resolving the Model-Measurement Discrepancy of Radon Entry into Houses 160
- Implications for Site Assessment and Modeling 162
- Future Research Directions 165
- References 167

List of Figures

Chapter I

Figure 1.	Radioactive decay series of ^{238}U	17

Chapter II

Figure 1.	Grab samples and continuous measurements of soil moisture around the Ben Lomond structure.	43
Figure 2.	Seasonal trends in average air permeabilities of the soil in the high-wall, mid-wall, low-wall, and subslab regions.	44
Figure 3.	North/south cross section of the Ben Lomond site showing measured and predicted pressure coupling at the probe locations.	45
Figure 4.	East/west cross section of the Ben Lomond site showing measured and predicted pressure coupling at the probe locations.	46
Figure 5.	Soil-gas entry rate vs. structure depressurization in the Ben Lomond west structure.	47

Chapter III

Figure 1.	Geometry for the real and image sources for the model of the dual-probe dynamic pressure measurements of soil permeability to air.	76
Figure 2.	Sample theoretical curves of time lag vs. permeability for a source at depth (L) = 2 m.	77
Figure 3.	Locations and results of static and dynamic permeability measurements.	78
Figure 4.	Schematic of apparatus for dual-probe dynamic pressure measurement of soil permeabilities.	79
Figure 5a.	Predicted lag time of signal vs. distance from source signal along a horizontal ray ($\theta = 0^o$, Figure 1) and a vertical ray ($\theta = 90^o$).	80

Figure 5b. Same as Figure 5a, except for a soil with permeability 8.5x10-12 m2. 80
Figure 6. Weighting factors of soil permeability as a function of distance from the source probe. 81

Chapter IV

Figure 1. Schematic of soil column. 105

Chapter V

Figure 1. Plan view of Ben Lomond site showing locations of static and dynamic permeability measurements. 118
Figure 2. Experiment configuration for representative dual-probe dynamic pressure measurements of soil permeability. 119
Figure 3. Results of dual-probe dynamic measurements and static measurements made over different integration lengths 120
Figure 4. Conceptual model of soil, yielding scale dependent permeability. 121

Chapter VI

Figure 1. Soil regions used for modeling soil-gas and radon entry into the structure. 141
Figure 2. Radon entry rates vs. structure depressurization: model-measurement comparison. 142
Figure 3a. North/south cross section of the site showing measured and predicted radon concentrations, normalized with respect to the concentration measured in the deepest probe. 143
Figure 3b. East/west cross section of the site showing measured and predicted radon concentrations, normalized with respect to the concentration measured in the deepest probe. 144
Figures 4a and 4b. Model-measurement comparison of soil-gas radon depletion with structure depressurization. 145

Figures 4c and 4d. Model-measurement comparison of soil-gas radon depletion with structure depressurization. 146
Figure 5. North/south cross section of the site showing measured and predicted coupling at the indicated probe locations. 147

List of Tables

Chapter II

Table I. A comparison of measurements of permeability of soil to air made at 30 probes on the two dates with the highest and lowest average measured permeabilities. 41

Table A-I. Leakage equations and effective leakage area of the structure. 49

Chapter III

Table I. Permeabilities (k) at individual probes using static techniques and between the reference and detector probes using the dual-probe dynamic technique. 75

Chapter IV

Table I. Soil permeabilities measured across different lengths of soil in the soil column suing steady-state measurements. 103

Table II. Soil permeabilities measured across different lengths of soil in the soil column using dynamic pressure measurements. 104

Chapter V

Table I. Permeabilities made over integration distances between 0.1 and 3.5 m using various measurement techniques. 116

Chapter VI

Table I. Soil characteristic assigned to different regions in the soil. 137

Table II. Soil permeability configurations for different model runs. 138

Table III. Soil-gas entry rates measured and modeled given different assumptions about soil permeability characteristics. 139
Table IV. Static depressurization experiments used to determine the soil radon concentration indicated in Figures 4a–d. 140
Table A.I. Uranium content and emanation fraction of core samples of concrete. 151
Table A.II. Diffusive radon fluxes from the interior walls of the east structure. 154
Table A.III. Estimation of ^{222}Rn diffusion across the slot 156
Table A.IV. Comparison of radon entry into the structure by advection and diffusion. 156

Acknowledgments

I cannot thank my two advisors, Richard Sextro and Bill Nazaroff, enough. They have been a great pleasure to work with. They have both treated me as a colleague and have advised me fairly and conscientiously. They have also provided me with fantastically complementary support in my quest for the elusive Ph.D.!

Rich lured me back to indoor air and to the Small Structures Project with his good humor and great willingness to work side by side, in the lab, or out in the field, at all hours, kept going only by a thermos of Pete's. Rich truly has been a mentor...with a voltmeter, a 9/16" wrench (not that damn crescent!), or a white board covered with toxic, polluting pens! We've both gotten a bit grayer over the past 7 years, but it's been fun!

Bill is the strategic planner. I would complain about an intransigent partial differential equation and he would pull me back to the big picture: "Where are you in your research? Where are you going to publish? What is your goal with all of this anyway?" Bill has kept me honest when I got carried away with the really *hot* results and he bolstered me in my disappointment when the reviewers just didn't seem to get it. Bill's guidance and meticulous review of my results have been invaluable. Thanks for the insights—and the help with the partial differential equation!

This dissertation reflects the contributions of many people. Mark Modera was responsible for the initial design of the data acquisition and control system for the small structures. Tim Nuzum and Claude Khalizadeh provided technical support at the structures. In the later stages, John Wooley worked with me on experiments in the field and the laboratory. Ashok Gadgil, Bill Fisk, and Yvonne Tsang reviewed several rounds of manuscripts and offered advice. Harold Wollenberg, Steve Flexser, and Al Smith conducted geological analysis of the Ben Lomond site.

Claus Andersen and I field tested the experimental structure together. I will always remember how we alternately sealed each other into the sepulcher of the depressurized structure (attached to the outside world only via the air hose of our breathing apparatus) to perform leak tests with our faithful 'plumbers friend' and the bastardized CRM. I don't know what I would have done without those 'pity chocolates' and 'success raisins'!

Ken Revzan contributed in a number of ways: initially in helping to organize the initial handling and processing of the raw-data (a formidable task at ~1 Mbyte per day ongoing for years!), and later in modifying and helping run the three-dimensional radon transport model. In the end, I drove him to such distraction that he attempted to end his life by cutting off his toe with a lawn-mower! He has promised henceforth to stick to the manly art of computing.

I am grateful for the financial support I received during my graduate career. Early in the process the Associated Western Universities and the Department of Energy provided me with three years of fellowship support. In my last year I was honored with a Switzer Environmental Fellowship. LBL's Indoor Environment Program has supported me as a Graduate Research Assistant, both financially and generously with equipment, materials, and technical assistance.

Special thanks go to my friends at ERG, especially to Kate Blake who, even unto the end, was willing to do battle for me against the forces of evil at UC, and to Donna Bridges for all her love and the inside scoop! I thank my sister Linda for helping me, in my last-minute panic, to review and produce this document—done while I was recovering from pneumonia so that UC would not charge me an extra couple thousand dollars for late filin g! I also thank all of my friends who have helped make graduate school the best time of my life: especially Jeni and Neo (white-water mountain biking!), Bill and Laura (chocolate cake and lizards!), and Dave (mandolin!).

Most of all, I must thank Marc Fischer, my consistent, loving partner. He has always had time for me and has helped in uncountable ways on this project. He has worked with me in the field, read manuscripts, and provided a sounding board when I was near despair. But most important, he insisted I have fun despite it all!

CHAPTER I

Introduction

OVERVIEW

This research began with my observation that models of radon entry into houses appeared to consistently and significantly underestimate entry rates measured at real houses. These models simulate the dominant mechanism responsible for high concentrations of radon indoors, pressure driven entry of radon-bearing soil gas caused by depressurization of the building substructure relative to the surrounding soil. This is the case, for example, when heated indoor air rises causing air from the surrounding soil to be drawn in through penetrations in the substructure. A critical input to these models is an empirical assessment of soil permeability — the factor that typically controls the entry rate of soil gas into houses.

In the past, the model-measurement discrepancies had been attributed to poor understanding of inherently complex field sites. Neither our measurement techniques for assessing transport nor our conceptual models of radon transport through soil were in question. Yet, with each new measurement consistently revealing higher entry rates than predicted by our models, my confidence in the foundations of our understanding of radon entry was eroded.

The first step was to ensure that the model-measurement discrepancy was in fact real and not merely an artifact of poorly understood field sites. This required careful and complete controlled experiments at a well-characterized basement-like structure, to reduce uncertainty as much as possible in our knowledge of the structure and the surrounding soil. The structure was designed to have simple geometry to facilitate comparisons between measurements and model predictions.

Confirmation of the discrepancy at the experimental structure indicated that there had to be something wrong, either with our empirical techniques for assessing transport, with our conceptual model of transport, or both. The most interesting and promising hypothesis was that both our conceptual model of the soil and our technique for assessing regional soil permeabilities was in error. In particular, typical assessments of regional soil permeability, from multiple small-scale measurements, systematically underestimate effective soil permeability at the larger scale of several m at which flows are expected to occur in real houses (or the experimental structure).

To test this hypothesis, I designed a technique to measure soil permeability to air *in situ* over different length scales and spatial orientations. (The latter was necessary to test a secondary hypothesis that anisotropy of permeability explained observed anomalies in the soil pressure field.) The bulk of this dissertation (Chapter III - VI) describes the development and testing of the new dual-probe dynamic pressure technique for measuring soil permeabilities and the use of the technique in the field to investigate the scale dependence of soil permeability to air. The field tests confirm the hypothesis that soil permeability at the site of the experimental basement is indeed strongly scale dependent over a range of scales between 0.1 and 3.5 m (Chapter V). In addition, measurements of soil radon depletion with structure depressurization are used as an independent confirmation of soil permeability at the several m scale (Chapter VI). When the new assessments of soil permeability at the 'structure scale' where used as input to the numerical model, the model overestimation of the radon entry rate was reduced from a factor of ~7 to less than a factor of 2.

BACKGROUND

"Bergkrankheit" (or mountain sickness), among sixteenth century pitchblende (radium) miners in the Erz Mountains of Germany, was the earliest evidence of the health hazard of inhaled radon and its progeny. Apparently labor rights were not strong in Germany at the time, since studies of miners in these same mines three hundred years later revealed that life expectancy after beginning work in the mines was only 20 years, with lung diseases accounting for 75% of all deaths. It was not until the 1920's that the lung disease was attributed to radiation, as opposed to inhaled arsenic [1]. And it was not until the 1970's that residential exposure to indoor radon began to be considered as a potential public health risk [2].

Currently, the majority of scientific opinion considers indoor radon exposure a significant public health risk [3-8]. Based on epidemiological studies of miners, and correcting for differences in the environmental conditions, occupancy levels, and activity levels of the mining vs. the residential populations, the excess lung cancer risk associated with the average radon concentration found in US homes (52 Bq/m^3) is estimated to be 0.7% [7, 8], yielding about 15,000 radon-induced lung cancer deaths per year [8-10].[1] Because of the lognormal distribution of indoor radon concentrations, large numbers of people experience radon concentrations — and therefore radon-induced lung cancer risks — far above the average level [11, 12]

The isotope primarily responsible for the radon-associated lung cancer risk is believed to be ^{222}Rn — a decay product of ^{238}U, which is ubiquitous in the earth's crust. (See Figure 1 for the ^{238}U decay series.) ^{220}Rn was not considered. Because of its relatively short half life, the time for transport of that isotope from its source is limited, effectively limiting the source region from which ^{220}Rn can be drawn into the indoor environment [2]. In addition, details of the ^{220}Rn decay series appear to limit the concentrations present in air and the dose delivered to the lungs [2]. For these reasons, my research focuses exclusively on the ^{222}Rn isotope. Therefore, when I refer to 'radon' in this dissertation, I am referring to that isotope.

The majority of the radiation dose comes from the α-decay of two progeny of ^{222}Rn, ^{218}Po and ^{214}Po. Both of these species are chemically

---

[1] This is the average risk for the general population including smokers and non-smokers. Note, however, that this *average* health risk might be a somewhat misleading indicator. A number of studies indicate that a majority of the risk is incurred among smokers because of an apparent synergism between smoking and radon exposure. The study of the National Research Council [7] finds the strongest synergism, reporting a barely sub-multiplicative effect of smoking on the baseline radon risk. According to that report, non-smokers exposed to the same radon concentrations as smokers have about a factor of ten lower radon-induced lung-cancer risk. Given that the total population risk (R) = fraction of population who are smokers (f_s) x the risk to smokers (r_s) + fraction of population who are non-smokers ($1-f_s$) x risk to non-smokers ($0.1\ r_s$), that is

$$R = f_s\, r_s + (1 - f_s)\,(0.1\, r_s)\,,$$

and taking f_s ~0.3, we find that the radon induced risk to smokers is ~ 2% and the risk to non-smokers is about 0.2%. This agrees with the most recent estimates of the US EPA ([11], pg. 8) active, tending to adhere to particles in the air and to lung tissue. Because of their relatively short half lives (~30 minutes or less), inhaled ^{218}Po and ^{214}Po tend to α-decay before they can be cleared from the lungs. Because ^{222}Rn is itself an inert gas with a relatively long half life of 3.82 days, if inhaled it is less to be retained by the lung or to decay while in close proximity to lung tissue.

Early studies on the source of indoor radon focused on uranium-mill tailings used as landfill at building sites and on building materials with high radium content [13-15]. Soon, however, it was discovered that these sources could not explain the high levels found in many homes. Attention turned to naturally occurring radon in soil gas. A series of tests carried out by DSMA ATCON Ltd. [16-18] on high radon houses in Elliot Lake, Ontario, in Canada, indicated that, in order to explain the high concentrations found indoors, radon must have been entering by advection of soil gas rather than by diffusion from the soil. The history and conclusions drawn from those studies is reported by Scott [19].

Since that time a number of studies have confirmed that pressure-driven (advective) flow is the dominant source of radon in houses with elevated concentrations [15, 20-28]. Advective flow of radon-bearing soil gas into a house results from a pressure deficit at the base of the house relative to the surrounding soil. Causal mechanisms include: temperature differences between indoors and out, wind on the house superstructure, unbalanced building ventilation [29], and temporal variations in barometric pressure [30-33].

The dominant conceptual model for assessing advective entry has been a house sitting in relatively permeable, homogeneous soil that draws soil-gas inside via penetrations in an otherwise impermeable building substructure. Entry via permeable below-grade walls also has been considered and might be important in houses with substructures constructed of hollow or back-filled cement-block walls [34]. Much research has focused on houses with basements, because of the large interfacial area between the substructure and the soil and because the radon concentration at the assumed entry location (the floor) is higher because of the deeper soil location.[2] Penetrations that

---

[2] Crawl-space and slab-on-grade houses have also been studied. Many of the results of studies in one type of structure apply to other types [15, 35].

allow soil-gas entry include a shrinkage gap around a poured-concrete slab floor, gaps left around service entrances such as sewer pipes, or cracks from soil-movement [19, 29, 36, 37].

Penetrations in the building substructure are typically large enough that the soil, not the building shell, provides the major resistance to soil gas flow [29]. The permeability of soil to air is therefore a critical parameter in predicting radon transport and entry rates. Soil permeability can vary over eight orders of magnitude (10^{-16} - 10^{-8} m^2) from clay to gravel. Given the homogeneous soil assumption, theoretical calculation suggests that advective entry is important for soil permeabilities greater than about 10^{-12} m^2 [29].

Several steady-state models have been developed to study radon and soil gas entry, most in accordance with the conceptual model outlined above. These include analytical (closed form) models that assume idealized leakage geometries [20, 38, 39] and more flexible numerical models. The earliest numerical model was used to study advective entry into houses with basements under the assumption of uniform, isotropic soil [15, 40-42]. A 2-dimensional finite-difference model was developed to study the effects of exhaust ventilation on radon entry into houses with crawl spaces or basements [37, 39, 43]. Loureiro *et al.* [36, 44] developed a 3-dimensional code that simulates entry by advection and diffusion and allows for two soil types. This model was later modified to include thermal effects and a different structure and grid geometry [45, 46]. A similar model has been recently made available through Rogers and Associates Engineering Corporation [47, 48]. An addition, a 3-dimensional, dynamic model of multi-phase fluid flow has been used to effects of barometric pressure fluctuations on soil-gas and radon entry into a basement [32, 33].

While the environmental and structural complexity of the radon entry problem necessitates the use of numerical models, this very complexity has made it impossible to validate them rigorously with the relatively simple field-monitoring studies conducted to date. Comparisons that have been made between measured and modeled radon entry rates have, however, indicated a persistent, large discrepancy. Significant model-measurement discrepancies have also been observed in the pressure coupling between the house and the soil.[3]

These findings suggest an error in our conceptual model of radon entry, an error in the empirical inputs to the radon transport models (particularly in site assessments of soil permeability to air), or both. In any case, the discrepancies undermine confidence in our ability to assess accurately radon entry potential, to use the models as tools to design radon mitigation systems, or to develop building-construction guidelines to ensure low indoor radon concentrations.

A number of examples indicate the magnitude and scope of the model-measurement discrepancies. The electrical analog model of Nazaroff *et al.* [20] underpredicted pressure coupling measured between the soil and basement of a study house by more than a factor of 10. The modeling of Revzan *et al.* [45] underpredicted soil gas entry by a factor of 4, when compared to the mean entry rate measured in seven homes in the Spokane River Valley by Turk *et al.* [28, 49]. Garbesi and Sextro [34] found a similar discrepancy when comparing measurements made at a single-story house with a basement to predictions of a simple analytical model of soil-gas entry and with numerical models of the pressure field. Soil-gas entry was underpredicted by an order of magnitude, and pressure coupling was underpredicted by a factor of ~3. In that case the discrepancy might have been explained in part by permeable basement walls and layered soil.

Unfortunately, the large uncertainties inherent in these field studies prevent their use in determining the source of the model-measurements discrepancies. This fact led to arguments that it was a lack of understanding of the exact nature of the field sites, rather than inaccurate models or measurements, that created the discrepancies. One large source of uncertainty in measurements made at houses is inadequate knowledge of the location(s) at which soil enters the structure. This leads to uncertainty in the radon concentration of soil-gas entering the house, and therefore to uncertainty in the radon-based-mass-balance estimate of the soil-gas entry rate. Limitations in the ability to probe the soil sufficiently to determine its macrostructure

---

[3] Pressure coupling is the fraction of the total depressurization of the structure that is seen at a given point in the soil, and is an indication of the field of influence of the structure (*i.e.*, from how far it can draw radon-laden soil gas).

(and therefore the nature of air flow through the soil) also leads to uncertainties about the appropriate empirical inputs to the models. In a couple of studies, soil-layering was suggested as a possible source of the observed model-measurement discrepancy [20, 34], but the hypothesis was not substantiated.

OVERVIEW OF THE RESEARCH

The research described here is part of a larger effort, known as the Small Structures Project, being conducted in the Indoor Environment Program of the Lawrence Berkeley Laboratory, and described by Fisk *et al.* [43, 50]. The broad aims of this research are to improve our understanding of radon entry into houses under different environmental conditions and for different types of structures, and to validate existing mathematical models of advective transport of radon into house. The numerical models are critical tools to aid in the design of radon-mitigation systems and building-construction guidelines that minimize indoor radon concentrations. The flexibility and low operating cost of these models make them indispensable tools for simulating the many possible environmental conditions and housing designs that can effect radon entry.

Within the broader framework of this project, my research has two main objectives: (1) to establish, using controlled experiments, whether the model-measurement discrepancies observed in field studies of houses are real or simply an artifact of incomplete understanding of complex field sites; and (2) if they are real, to determine the source(s) of the discrepancies. Technical objectives include developing a technique for making accurate site assessments of radon entry potential and validating a numerical model used to study radon transport and entry into houses.

OUTLINE OF DISSERTATION

In Chapter II, the model-measurement discrepancies observed at real houses are validated by controlled measurements made over a two-year period in a thoroughly instrumented experimental basement located in the

Santa Cruz Mountains, in Ben Lomond, California. The experimental basement, one of two at that site, is situated in natural granitic soil on a plot surrounded by mature Coast Live Oaks (*Quercus agrifolia,* also known as California Live Oak). The structure is geometrically simple, to facilitate simulation of the experiments with a numerical model, but designed to capture salient features of standard building practices. Advective entry of soil gas is restricted to occur through precisely machined slots in the concrete slab floor, simulating the shrinkage gap that can form around a poured concrete floor. The slab floor in the structure under consideration is underlain by a layer of gravel. (This is a common building practice to facilitate drainage.)

The results of the experiments described in Chapter II show a large discrepancy between the measured and model-predicted rate of soil-gas entry into the structure at fixed structure depressurization—the measured entry rate being an order of magnitude larger than the predicted rate. In addition, the pressure field in the soil surrounding the structure is observed to extend farther from the structure, with larger magnitude, than predicted by the model. A number of hypotheses are raised to explain these discrepancies. Regarding the soil-gas entry discrepancy, the most promising among them is the possibility that assessments of soil permeability, obtained by averaging standard static depressurization measurements that integrate over a length scale of ~0.5 m or less, do not reflect effective permeabilities for flows that are expected to occur on a scale of several meters (or more) at real houses and at the experimental structure.

Chapter III describes a dual-probe dynamic pressure technique that was developed to test the hypothesis described above. The technique measures soil permeabilities at different length scales, spanning the range from which static probes measure permeability up to the scales at which houses tend to interact with the soil. The technique imposes a sinusoidally oscillating pressure signal at a source probe. This signal is detected at a second probe. The signal propagation time is used as a measure of the effective permeability of the path between the probes. Because the detector probe can be located at any position relative to the source probe, the technique also can be used unambiguously to detect anisotropy (which is impossible with a single probe).

A mathematical model is developed to interpret the experimental results of the dual-probe dynamic pressure measurements and preliminary field tests are conducted. A comparison of the small-scale static measurements with the longer-scale dynamic measurements appears to indicate that soil permeability is scale dependent. The potentially controversial finding of scale-dependent permeability motivated the work in the next two chapters.

Chapter IV describes laboratory experiments used to validate the dual-probe dynamic pressure technique. A 2.5-m long soil-column is developed in which both static and one-dimensional dynamic measurements of permeability are made at different length scales. In addition, dynamic measurements are run at different source-signal frequencies. The techniques agree to within 20% in their predictions of permeability, which is adequate for use in the field studies. More important, in the homogeneous sand used as the porous medium in the column, no scale-dependence was observed with either technique over a range of lengths over which strong scale dependence was apparent in the field. This assures us that the scale dependence observed in the field is unlikely to be an artifact of the dynamic measurement technique. Furthermore, these tests give us confidence in the assumptions of the mathematical model that is used to interpret the dynamic measurements.

Chapter V describes a thorough investigation of the scale dependence of soil permeability at the Ben Lomond site, in the soil adjacent to the experimental basement. Single-probe static measurements are made using two probe designs that integrate over different length scales (0.1 and 0.5 m). Dual-probe dynamic measurements are made over a range of scales between 0.5 and 3.5 m. Soil air-permeability at this site is found to depend strongly on length scale with permeability increasing by more than a factor of 40 when length scale is increased by a factor of 35.

Chapter VI evaluates the extent to which scale-dependent permeability resolves the model-measurement discrepancy observed at the Ben Lomond site. The 3-dimensional numerical model is revised to incorporate the anisotropy observed at the site and the soil is assigned a permeability for scale of ~3 m. Strictly speaking, the finding of scale-dependent permeability indicates that a homogeneous model of soil is not appropriate, because a homogeneous medium will not reproduce scale dependence. Nevertheless, it is possible in this case to use the homogeneous model to estimate the contribution of scale-dependent permeability to the model-measurement discrepancy, because the scale dependence of permeability appears to approach asymptotically a constant value at about the scale at which the structure interacts with the soil. The modeling results indicate that scale-dependent permeability reduces the observed discrepancy in soil-gas entry from a factor of ~9 to a factor of 2.5. The remaining discrepancy may be due to an imperfect interface at the soil-wall boundary of the structure, which would enhance flow relative to the model description of the interface.

Chapter VII summarizes the findings and discusses the implications of the results for assessment and modeling of radon entry. It is pointed out that many of the results are directly applicable to understanding the transport of other gas-phase contaminants in soils. For example, the off-site migration and subsequent entry into houses of contaminated landfill gas is almost a direct analog of the radon transport problem, and is currently the focus of considerable study and litigation. The finding of scale-dependent permeability of soil to air also appears to support current hydrogeological research on flow through heterogeneous porous media, and extends the relevance of that work to gas-phase flow through near-surface soil.

REFERENCES

1. Miller, E.W., Radon Hazard: A Historical Perspective. In: *Environmental Radon: Occurrence, Control, and Health Hazards,* Majumdar, S. K., Schmalz, R. G. and Miller, W. E., Ed. The Pennsylvania Academy of Science: Easton, PA, 1990, 1-12.

2. Nero, A.V., Radon and Its Decay Products in Indoor Air: An Overview. In: *Radon and It's Decay Products in Indoor Air,* Nazaroff, W. W. and Nero, A. V., Ed. John Wiley and Sons: New York, 1988, 1-53.

3. United Nations Scientific Committee on the Effects of Atomic Radiation, *Sources, Effects and Risks of Ionizing Radiation,* United Nations: New York, 1988.

4. United Nations Scientific Committee on the Effects of Atomic Radiation, *Ionizing Radiation: Sources and Biological Effects,* United Nations: New York, 1982.

5. National Council on Radiation Protection and Measurements (NCRP), *Evaluation of Occupational and Environmental Exposure to Radon and Radon Daughters in the United States.* NCRP Report No. 78, National Council on Radiation Protection and Measurements, Bethesda, Md: 1984.

6. International Commission on Radiological Protection (ICRP), *Lung Cancer Risk from Indoor Exposures to Radon Daughters,* ICRP Publ. No. 50, Pergamon Press: Oxford, 1987.

7. National Research Council, *Health Risks of Radon and Other Internally Deposited Alpha-Emitters. BEIR IV,* National Academy Press: Washington, DC, 1988.

8. National Research Council, *Comparative Dosimetry of Radon in Mines and Homes,* Panel on Dosimetric Assumptions Affecting the

Application of Radon Risk Estimates, National Academy Press: Washington, DC, 1991.

9. Lubin, J.H. and Boice Jr., J.D., Estimating Rn induced lung cancer in the United States, *Health Physics*, 1989, 57: 417-427.

10. Samet, J.M., Radon and lung cancer, *Journal of the National Cancer Institute*, 1989, 81: 745-757.

11. US Environmental Protection Agency, *National Residential Radon Survey*. EPA 402-R-92-011, US Environmental Protection Agency: 1992.

12. Nero, A.V., Schwehr, M.B., Nazaroff, W.W. and Revzan, K.L., Distribution of airborne radon-222 in U.S. homes, *Science*, 1986, 234: 992-997.

13. Cothern, R.C. and Smith Jr., J.E., Ed. *Environmental Radon*. 1987, Plenum Press: New York, N.Y.

14. Nero, A.V., Gadgil, A.J., Nazaroff, W.W. and Revzan, K.L., *Indoor Radon and Decay Products: Concentrations, Causes, and Control Strategies*. DOE/ER-0480P, Department of Energy, Washington, D.C.: 1990.

15. Scott, A.G., *Computer modeling of radon movement*. In: EML Indoor Radon Workshop, 1982. Report EML-416, Environmental Measurements Laboratory, New York: 1983.

16. DSMA ATCON Ltd. and Acres Consulting Services Ltd., *Variation of Radon Concentration in Soil Gas*. DSMA ATCON Ltd., Toronto: 1979.

17. DSMA ATCON Ltd., *The source of Radon at Elliot Lake*. In: First Workshop on Radon and Radon Daughters in Urban Communities. Report AECB-1164-1, Atomic Energy Control Board, Ottawa: 1978.

18. DSMA ATCON Ltd. and Acres Consulting Services Ltd., *Report on Investigation and Implementation of Remedial Measures for the Radiation Reduction and Radioactive Decontamination of Elliot Lake, Ontario.* Atomic Energy Control Board. Ottawa: 1978.

19. Scott, A.G., Preventing radon entry. In: *Radon and Its Decay Products in Indoor Air,* Nazaroff, W. W. and Nero, A. V., Ed. John Wiley and Sons: New York, N.Y., 1988, 407-433.

20. Nazaroff, W.W., Lewis, S.R., Doyle, S.M., Moed, B.A. and Nero, A.V., Experiments on pollutant transport from soil into residential basements by pressure-driven airflow, *Environmental Science and Technology,* 1987, 21: 459-466.

21. Nazaroff, W.W., Entry by pressure-driven flow or molecular diffusion? A reassessment of ^{222}Rn concentrations measured in an energy efficient house, *Health Physics,* 1988, 55: 1005-1009.

22. Nazaroff, W.W., Boegel, M.L. and Nero, A.V., *Measuring radon source magnitude in residential buildings.* In: Proceedings of the International Meeting on Radon-Radon Progeny Measurements. EPA 520/5-83/021., US Environmental Protection Agency, Washington, DC: 1981.

23. Nero, A.V. and Nazaroff, W.W., Characterizing the source of radon indoors, *Radiation Protection and Dosimetry,* 1984, 7: 23-39.

24. Nazaroff, W.W., Feustel, H., Nero, A.V., Revzan, K.L., Grimsrud, D.T., Essling, M.A. and Toohey, R.E., Radon transport into a detached one-story house with a basement, *Atmospheric Environment,* 1985, 19: 31-43.

25. Bruno, R.C., Sources of indoor radon in houses: A review, *Journal of the Air Pollution Control Association,* 1983, 33: 105-109.

26. Åkerblom, G., Anderson, P. and Clavensjo, B., Soil gas radon—A source of indoor radon daughters, *Radiation Protection Dosimetry*, 1984, 7: 49-54.

27. Sextro, R.G., Moed, B.A., Nazaroff, W.W., Revzan, K.L. and Nero, A.V., Investigations of soil as a source of indoor radon. In: *Radon and Its Decay Products: Occurrences, Properties, and Health Effects*, Hopke, P. K., Ed. American Chemical Society: Washington, DC, 1987, 10-29.

28. Turk, B.H., Prill, R.J., Grimsrud, D.R., Moed, B.A. and Sextro, R.G., Characterizing the occurrence, sources and variability of radon in Pacific Northwest homes, *Journal of the Air and Waste Management Association*, 1990, 40: 498-506.

29. Nazaroff, W.W., Moed, B.A. and Sextro, R.G., Soil as a source of indoor radon: Generation, migration, and entry. In: *Radon and Its Decay Products in Indoor Air*, Nazaroff, W. W. and Nero, A. V. J., Ed. John Wiley and Sons: New York, 1988, 57-112.

30. Hintenlang, D.E. and Al-Ahmady, K.K., Pressure differentials for radon entry coupled to periodic atmospheric pressure variations, *Indoor Air*, 1992, 2: 208-215.

31. Hernandez, T.L., Ring, J.W. and Sachs, H.M., The variation of basement radon concentrations with barometric pressure, *Health Physics*, 1984, 46: 440-445.

32. Narasimhan, T.N., Tsang, Y.W. and Holman, H.Y., On the potential importance of transient air flow in advective radon entry into buildings, *Geophysical Research Letters*, 1990, 17: 821-824.

33. Tsang, Y.W. and Narasimhan, T.N., Effects of periodic atmospheric pressure variation on radon entry into buildings, *Journal of Geophysical Research*, 1992, 97: 9161-9170.

34. Garbesi, K. and Sextro, R.G., Modeling and field evidence of pressure-driven entry of soil gas into a house through permeable below-grade walls, *Environmental Science and Technology*, 1989, 23: 1481-1487.

35. Nazaroff, W.W. and Doyle, S.M., Radon entry into houses having a crawl space, *Health Physics*, 1985, 48: 265-281.

36. Loureiro, C.O., *Simulation of the Steady-State Transport of Radon from Soil into Houses with Basements under Constant Negative Pressure.* LBL-24378, Lawrence Berkeley Laboratory, Berkeley, CA: 1987.

37. Mowris, R., *Analytical and numerical models for estimating the effect of exhaust ventilation on radon entry in houses with basements or crawl spaces.* LBL-22067, Lawrence Berkeley Laboratory, Berkeley, CA.: 1986.

38. Nazaroff, W.W., Predicting the rate of ^{222}Rn entry from soil into the basement of a dwelling due to pressure-driven air flow, *Radiation Protection Dosimetry*, 1988, 24: 199-202.

39. Mowris, R.J. and Fisk, W.J., Modeling the effects of exhaust ventilation on ^{222}Rn entry rates and indoor ^{222}Rn concentrations, *Health Physics*, 1988, 54: 491-501.

40. DSMA Atcon, L., *Review of Existing Information and Evaluation for Possibilities of Research and Development of Instrumentation to Determine Future Levels of Radon at a Proposed Building Site.* INFO-0096, Atomic Energy Control Board, Ottawa, Canada: 1983.

41. DSMA Atcon Ltd., *A Computer Study of Soil Gas Movement into Buildings.* Report 1389/1333, Department of Health and Welfare, Ottawa, Canada: 1985.

42. Eaton, R.S. and Scott, A.G., Understanding radon transport into houses, *Radiation Protection and Dosimetry*, 1984, 7: 251.

43. Fisk, W.J., Flexser, S., Gadgil, A.J., Holman, H.Y., Modera, M.P., Narasimhan, T.N., Nuzum, T., Revzan, K.L., Sextro, R.G., Smith, A.R., Tsang, Y.W. and Wollenberg, H.A., *Monitoring and Modeling for Radon Entry into Basements: A Status Report for the Small Structures Project.* LBL-27692, Lawrence Berkeley Laboratory: Berkeley, CA: 1989.

44. Loureiro, C.O., Abriola, L.M., Martin, J.E. and Sextro, R.G., Environmental Science and Technology, 1990, 24: 1338-1348.

45. Revzan, K.L., Fisk, W.J. and Gadgil, A.J., Modeling radon entry into houses with basements: Model description and verification, *Indoor Air,* 1991, 1: 173-189.

46. Revzan, K. and Fisk, W., Modeling radon entry into houses with basements: The influence of structural factors, *Indoor Air,* 1992, 2: 40-48.

47. Nielson, K.K., Rogers, V. and Rogers, V.C., *RAETRAD: Version 3.1 User Manual.* RAE-9127/10-1, Rogers & Associates Engineering Corp., Salt Lake City, UT: 1992.

48. Nielson, K.K., Rogers, V.C., Rogers, V. and Holt, R.B., *The RAETRAD Model of Radon Gas Generation, Transport, and Indoor Entry.* RAE-9127/10-1, Rogers & Associates Engineering Corp., Salt Lake City, UT: 1992.

49. Turk, B.H., Prill, R.J., Grimsrud, D.T., Moed, B.A. and Sextro, R.G., *Radon and Remedial Action in Spokane Valley Homes, Volume I: Experimental Design and Data Analysis.* LBL-23430, Lawrence Berkeley Laboratory, Berkeley, CA: 1987.

50. Fisk, W.J., Modera, M.P., Sextro, R.G., Garbesi, K., Wollenberg, H.A., Narasimhan, T.N., Nuzum, T. and Tsang, Y.W., *Radon Entry into Basements: Approach, Experimental Structures, and Instrumentation of the Small Structures Project.* LBL-31864, Lawrence Berkeley Laboratory: Berkeley, CA: 1992.

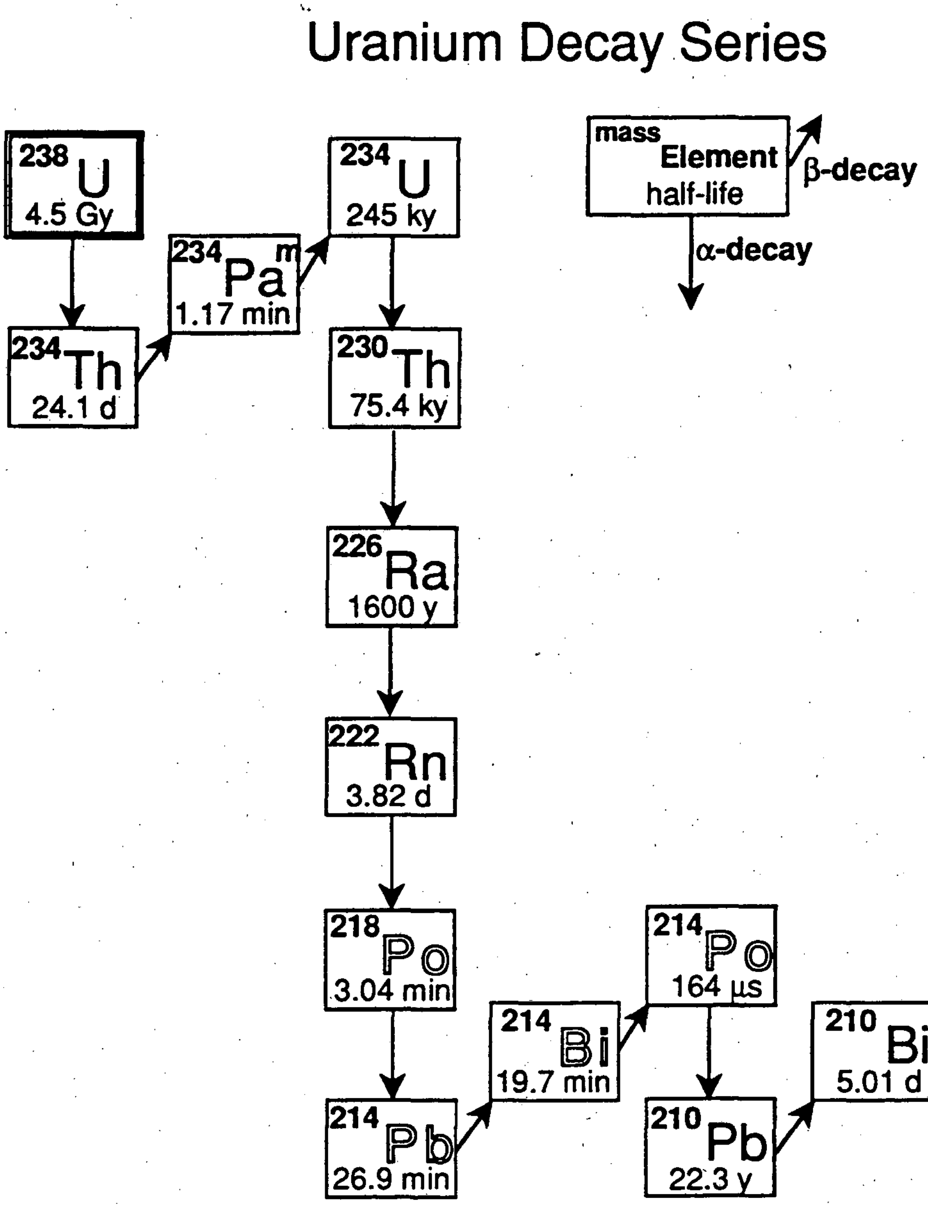

Figure 1. Radioactive decay series of ^{238}U. It is the α-decays associated with ^{218}Po and ^{214}Po that are primarily responsible for radon-induced lung cancers.

CHAPTER II

Soil-Gas Entry into an Experimental Basement: Model-Measurement Comparisons and Seasonal Effects[*]

SYNOPSIS

Previous studies have reported a large and persistent discrepancy between field measurements and model predictions of pressure-driven entry of soil-gas into houses—the phenomenon that causes high concentrations of radon indoors. The discrepancy is often attributed to poor understanding of inherently complex field sites. This chapter compares measurements of soil-gas entry made at a full-scale test basement, located in natural soil, with predictions of a three-dimensional finite-difference model. The results corroborate the earlier findings. The model underpredicts the soil-gas entry rate by a factor of 7, given an empirical estimate of the effective soil permeability to air based on an arithmetic mean of multiple measurements made at different locations in the soil surrounding the basement.[1] The effect of seasonal changes in soil conditions on soil-gas entry is also examined. Despite large seasonal changes in near-surface soil moisture content and air permeability, there is no observable effect on soil-gas entry, apparently because critical soil conditions near the soil-gas entry location in the structure floor remain relatively constant.

---

[*] This Chapter was taken from the published paper: Garbesi, K., Sextro, R.G., Fisk, W.J., Modera, M.P., and K.L. Revzan, Soil-gas entry into an experimental basement: Model-measurement comparisons and seasonal effects, *Environmental Science and Technology,* 1993, 27: 466 - 473. Minor revisions have been made in the chapter for clarity. The modeling of soil-gas entry into the structure has been slightly revised in Chapter VI, based on data that became available subsequent to publication of the paper. Those changes were not incorporated into this chapter in order to keep it as closed to the published form as possible.

[1] In Chapter VI, the modeling of the bulk soil was revised based on data that became available after the publication of this Chapter as a paper. Based on that analysis, the model estimate of soil-gas entry rate exceeds the measured value by a factor of ~9 (rather than 7).

INTRODUCTION

Soil-gas entry into houses has been studied in relation to indoor exposures of humans to radon progeny and volatile organic chemicals (VOC). Advective entry of soil gas is believed to be the dominant source of excessive indoor radon concentrations [1-6], and may be a significant source of indoor exposure to toxic VOC in houses near landfills [7], near leaky gasoline storage tanks, or near other chemical storage or disposal sites. A number of mechanisms can cause the indoor-outdoor pressure difference that drives advective entry: thermal differences between indoors and out, wind loading on the building superstructure, imbalanced building ventilation systems, and barometric pressure fluctuations [8-11].

Numerical modeling and field studies at existing houses have been the main methods for investigating soil-gas entry. Although a great deal has been learned from these studies, large uncertainties remain. In field studies at real houses, the large size and complex geometries lead to significant uncertainties regarding the transport pathways through the soil and into the structure; significant entry points may even be concealed from view. The pressure differences that drive soil-gas entry are uncontrolled and temporally variable. In addition, at occupied sites, detailed studies are generally impossible because of the invasive nature of the instrumentation required to fully probe the site for necessary information on soil, structure, and atmospheric and meteorological conditions.

This paucity of data from thoroughly characterized sites has made it impossible to test rigorously the conceptual model of contaminant entry from soil or to validate rigorously the numerical models. Yet, without the understanding that could be gained therefrom, the ability to achieve a number of public-health-related policy goals is impaired. Regarding the indoor radon problem in particular, improved understanding would help us to locate houses with the potential for high radon concentrations (obviating the need for costly testing in all homes), to design effective radon mitigation systems for different environments and structures, and to develop rational and cost-effective building regulations for new structures that minimize indoor exposures.

Yet, there is evidence from a number of studies that our understanding of soil-gas entry into houses might have serious flaws. Comparisons between measurements and the results of numerical and analytical models have indicated significant discrepancies. Nazaroff *et al.* [5] found disturbance pressures in the soil due to house depressurization 10 times greater than predicted with their analytical model. The numerical modeling of Revzan *et al.* [12] found that average soil-gas entry measured by Turk *et al.* [6] exceeded their modeled values by a factor of 4. Similarly, Garbesi and Sextro [13] found measured soil-gas entry rates to be high by a factor of 10 and far-field pressure coupling to be high by a factor of 3, when compared to the model predictions, when the model employed the standard assumptions that walls and floor are impermeable to gas flow, the soil is homogeneous, and soil-gas is restricted to a gap in the wall-floor interface. That work indicated that the assumed soil-gas entry pathway and the macroscopic structure of the soil permeability field can have a large effect on the predicted entry rate and pressure field.

To overcome the large uncertainties inherent in field studies, we designed and built room-sized experimental structures for the detailed study of radon and soil-gas entry into basements [14, 15]. These primarily below-grade structures are thoroughly instrumented and controlled and have a simple geometry suitable for testing existing numerical models employing the standard assumptions about soil-gas entry. In particular, the structures have impermeable walls and floors, with pressure-driven entry of soil gas restricted to precisely engineered slots in the floors.

This chapter discusses research on soil-gas entry carried out at the westernmost of two basement structures located in the Santa Cruz Mountains, near Ben Lomond, California. There were two goals: to compare detailed measurements of soil-gas entry determined from radon mass-balance calculations with predictions of a three-dimensional finite-difference model and to investigate the effects of seasonal changes in soil conditions on soil-gas entry into the structure. The experiments use controlled artificial depressurization of the structure in the range of -20 to -70 Pa below atmospheric pressure. Because transport of soil gas into the structure is governed by Darcy's law (*i.e.,* is a linear function of pressure)[2], the results of

---

[2] Darcy actually studyied the flow of liquids in porous media. However, the driving equation for gas flow induced by small enough disturbance pressures has the mathematical formulation ([16], pg. 271). I therefore use Darcy's law to refer to low-Reynolds-number gas flow through soils throughout the dissertation.

these experiments can be extrapolated down to the few Pascal depressurization typical of real houses under ordinary operating conditions.[3]

EXPERIMENTAL METHODS AND RESULTS

This section describes site characterization and depressurization experiments carried out at the basement structure to assess pressure coupling between the structure and the soil (an indicator of the field of influence of the structure) and to study pressure-driven entry of soil gas into the structure at different times of year.

Site and Structure Characterization

The experimental structures are located in natural soil, beneath a canopy of oak trees. The region experiences an average 1.5 m of rainfall annually. A groundwater monitoring well at the site indicates typical groundwater levels of 15 m below the soil surface, although, in one measurement made in July 1991 the water level was only 10 m below the surface. Details on the structure design and instrumentation may be found in Fisk *et al.* [14]. Geological details of the site are described in Flexser *et al.* [17]. Important points are summarized below.

The structure is a single chamber with width, depth, and height of 2.0, 3.2, and 1.9 m, respectively (inner dimensions), ~0.1 m of the walls lying above grade. It is built of poured concrete with 0.15-m-thick walls and floor. A 12-cm-thick gravel layer underlies the floor slab. Inclusion of a gravel layer is a customary construction practice in some areas to facilitate water drainage away from the substructure. After the structure was built, the excavated region outside the structure walls was refilled with the natural soil; this region is referred to as the *backfill*. Care was taken to repack the backfill soil evenly and similarly to the surrounding soil.

The structure was designed to have minimum uncontrolled leakage from the surface and the soil, having an effective leakage area (ELA) of 0.12 cm^2 as measured on September 29, 1990, with all intentional openings to the

---

[3] For porous media in which flow has a Reynolds number less than order 1, fluid flow is governed by Darcy's law [8], given by Eq. 3, Chapter 3, in Cartesian coordinates for a 3-dimensional system.

soil sealed (see appendix to this chapter). ELA is a measure of the equivalent open area that would yield the observed leakage at 4-Pa depressurization [18].

The structure floor includes six slots that simulate the shrinkage gap that can develop in real houses at the periphery of poured concrete floors. The smooth-walled slots are 1 m long, 0.003 m wide, 0.15 m deep, and are inset 0.34 m from, and parallel to, the walls, inboard of the wall footer. There are two slots along the longer east and west walls and one each along the north and south walls.

Soil probes, described in Fisk *et al.* [15], penetrate the structure at 32 locations and are used for measuring pressure differences between the soil and the structure, for sampling ^{222}Rn, and for measuring the permeability of the soil to air. The probes are lengths of steel pipe with a cylindrical well screen of the same diameter welded near the solid, pointed end for soil-gas sampling and pressure measurements. Short, medium, and long probes, having lengths from the outside of the wall to the middle of the sampling screen of 0.50, 1.71, and 2.39 m, penetrate the walls horizontally at three depths below the soil surface: 0.18, 0.8, and 1.6 m, with eight probes of various lengths at each depth. These are referred to as *high-wall, mid-wall,* and *low-wall* probes, respectively. Eight probes of different lengths are installed vertically through the floor slab; their sampling screens are located 0.24, 0.50, 1.71, and 2.39 m below the bottom of the slab.

Data acquisition and control (DAC) of the structure were handled using commercially available software running on a personal computer (AST-286). DAC software was used to control the structure pressure and the multiplexed sampling of soil radon concentrations and soil gas pressures measured at up to 32 probe locations. It was also used to monitor and log numerous measurements of environmental variables such as soil and air temperatures, wind speed and direction, barometric pressure, structure-to-outside pressure differences, and soil and structure radon concentrations.

The structure pressure was controlled by adjusting exhaust air flow from the structure through 50 L/min mass flow controller using a proportional-integral-differential (PID) software control loop provided by the DAC system. Mass flow controllers were also used to control soil-gas sampling rates for radon measurements and for controlling the extraction of soil air during soil air-permeability measurements. The mass flow controllers independently control and monitor the flow rate. The flow-rate monitoring signals were all logged by the DAC system.

Naturally occurring ^{222}Rn in the soil is used as a soil-gas tracer to determine the soil-gas entry rate. Three continuous radon monitors (CRMs) are used to sample ^{222}Rn from air in the structure, slots, and soil probes. Structure air is maintained well-mixed by the use of an oscillating fan. This allows sampling to occur at a single location. Slot air is drawn from all six slots simultaneously, delivering a single sample to the CRM. Soil air samples are multiplexed from the probes to one CRM. We use the method of Busigin *et al.* [19] to interpret the CRM data. This is particularly important for the multiplexed probe samples in which large concentration changes are seen by the CRM, since the method corrects for α decays from radon daughters left in the scintillation cell from previous gas samples.

There are eight thermocouples sensing soil temperatures, one at each of four depths (0.20, 1.04, 1.83, and 2.44 m below the surface) in the backfill region, and four similarly placed sensors located 5 m from the structure. Temperatures inside and outside of the structure are also recorded, along with wind speed, wind direction, and barometric pressure.

Soil Moisture and Soil Air-Permeability

Soil moisture measurements are made using a time domain reflectometer (TDR) (Trase System I, Soil Moisture Equipment Corp.) sampling in two different modes. Grab samples are made at different locations on the same date to determine spatial heterogeneity using both 30-cm- and 15-cm-long probes. In other measurements, temporal changes are captured by leaving the 30-cm probe in place and recording soil moisture twice daily. Based on the manufacturer's specifications, the TDR averages soil moisture in a cylindrical volume (determined by the length of the probe and the distance between the two wave guides) to an accuracy of ± 2%.

Figure 1 shows soil-moisture data from measurements made between November 2, 1990 and October 1, 1991, at a location 6 m north of the structure. The vertical bars indicate the spatial variability in soil moisture, as determined by the sample standard deviation of the measurements made with the same length probe at different locations around the structure on a given date. The solid dots indicate continuous sampling with the 30-cm probe. There is considerable spatial variability in soil moisture content, reflecting heterogeneous drainage characteristics of the soil and soil surface conditions. Greater spatial variability is observed during the drier time of year, probably reflecting heterogeneity in the soil's capacity to retain water, although this interpretation is somewhat uncertain due to the limited number of grab samples taken during the wetter periods.

The continuous soil moisture data show a clear seasonal trend. The wet season, from about December to March, has elevated soil moisture at ~35%. Soil moisture then almost monotonically decreases to a dry season low of ~8%, except for the obvious rainfall event on June 26, 1991, during which 1.7 cm of rain fell in 1 day.

The permeability of the soil to air was measured at each of the soil-probe locations on a number of occasions between October 13, 1989, and January 7, 1992. The technique involves drawing a steady flow of soil air from a probe while recording the induced disturbance-pressure difference between the probe and the soil surface. The disturbance pressure is the absolute pressure difference between a point and an undisturbed reference location minus the hydrostatic component of pressure. That is

$$(1) \qquad P_d(h) = P(h) - P_{ref}(0) - \int_0^h \rho g \, dz$$

where the reference pressure, P_{ref}, is established at $z = 0$, at the soil surface; the disturbance pressure, $P_d(h)$, is measured at some point in the soil at depth $z = h$, z being positive downward; $P(h)$ is the absolute pressure at the same point; $\rho(z)$ is the density of air at depth z, and g is the gravitational constant at the earth's surface.

Assuming Darcy flow of soil gas, the soil permeability (k, in m^2) is determined from the relationship

$$(2) \qquad k = \frac{Q\mu}{S\Delta P}$$

where Q is the rate at which soil gas is drawn from the probe (in m^3/s), μ is the dynamic viscosity of air (1.75×10^{-5} Pa s at ambient conditions), ΔP is the disturbance pressure difference between the probe tip and the soil surface (in Pa), and S is the shape factor. The shape factor was determined by numerical modeling to be independent of depth and proximity to the structure to within 10% for the given locations of the probes [15] and has a value of 0.3 m.

Table I indicates the spatial variability in soil permeability and the effect of seasonal changes in soil conditions. The table gives absolute magnitudes of soil permeabilities for two dates: October 1, 1991, for which we found the highest average permeabilities, and January 7, 1992, for which we found the lowest. The uncertainties in the permeabilities are dominated by environmental noise in the measured disturbance pressures. The data are sorted according to location in the soil, demonstrating that there is some structure in the permeability field. Soil in the backfill region has, on average, somewhat lower permeability than the natural soil, and the near-surface natural soil has somewhat lower permeability than the rest of the natural soil. The range in permeability due to spatial variation is considerably larger than that due to seasonal variation (a factor of ~200 vs. a factor of ~4).

To capture how soil permeabilities change with time at different elevations in the soil, the permeabilities in each region (high-wall, mid-wall, low-wall, and subslab) are averaged for each date; the averages are then normalized with respect to their April 24, 1991, value. The seasonal trends are plotted in Figure 2.

During the period of decreasing moisture content in the surface soil (April to October) average soil permeability in the high-wall and mid-wall increased. Due to evaporative losses from the surface, the effect is largest in the near-surface soil, where average permeability in October peaked at 1.5 times its April value. In the final measurement made during the rainy season in January 1992, the near-surface soil permeability drops to 0.34 its initial value. The same effect, but of smaller magnitude, is seen in the mid-wall soil. Little seasonality is seen in the low-wall or subslab regions.

Pressure Field

To better understand the soil-gas transport pathways, we measured the disturbance pressure between the structure and the soil at the probe locations during artificial depressurization of the structure. The reference depressurization (total structure depressurization relative to the undisturbed state) is determined at the slab level using a 5-m long horizontal probe measuring the pressure difference between the soil and the structure.

We define *pressure coupling* as the percentage of the total structure depressurization that is seen at a given point in the soil (the disturbance pressure in the soil divided by the disturbance pressure at slab level in the structure). We report pressure coupling rather than disturbance pressures, since, given Darcy flow and negligible flow resistance through the slots relative to the soil, pressure coupling should be independent of the applied pressure in the structure.

The percent pressure coupling (PC) for a probe at level j is calculated using

$$(3) \qquad PC_j = \frac{100\left(\Delta P_{ref} - \Delta P_j - \left[\rho(T_{soil})_{h_j/2} - \rho(T_{in})\right] g h_j\right)}{\Delta P_{ref}} .$$

In this case the reference (z = 0) is taken at slab level with z positive upwards. The reference pressure-difference (ΔP_{ref}), in Pascal, is measured at slab level between the structure and a point in the soil sufficiently far away not to be disturbed by the structure and is equal to $P_{in,z=0} - P_{\infty,z=0}$. The soil-to-structure pressure difference (ΔP_j) measured at a probe on level j is equal to $P_{in,z=j} - P_{soil,z=j}$. The elevation of the jth level above z = 0 is given by h_j; $\rho(T_{soil})_{h_j/2}$ is the density of air at the soil temperature at elevation $h_j/2$ at the probe's distance from the structure (kg/m^3); $\rho(T_{in})$ is the density of air at the structure temperature (kg/m^3); and g is the gravitational acceleration at the earth's surface (9.8 m/s^2).

In practice, P_{ref} of Eq. 3 is corrected for potential pressure coupling in the reference probe itself by comparison with a time-averaged signal of the structure-to-outdoor pressure difference at the soil surface. We do not simply use the surface pressure difference as a reference because the PID control is unstable if referenced to the surface signal, which has large variability due to barometric pressure fluctuations and wind.

Figures 3 and 4 show north-south and east-west cross sections of the Ben Lomond site, indicating the pressure coupling measured on May 4, 1991, and on September 25, 1991. To reduce uncertainties due to the effect of wind on the near-surface pressure transducers, the data were taken from periods with the same low, average wind speeds (0.3 m/s). For these wind speeds the accuracy of the measurement is limited by the instrumental uncertainty of the pressure transducers and is 4% or less for all measurements.

Two features of the pressure fields stand out. First, the pressure coupling in the two experiments is remarkably similar. This implies that the pressure field is insensitive to significant seasonal changes, on the order of 60%, in near-surface soil permeability. Second, overall, the pressure field appears quite symmetric around the structure, indicating that the soil permeability field and the soil-gas flow field are also relatively symmetric on the large scale. A notable exception to the large-scale symmetry is observed in the medium length, low-wall probe on the west side of the structure, which showed significantly larger coupling (52%) than its neighbor nearer the structure wall (~28%). This result has appeared consistently in numerous pressure measurements made in the past 2 years. It suggests the existence of a preferred flow path running between or near the probe tip and the gravel.

Soil-gas Entry

A number of experiments were conducted to investigate advective entry of soil gas into the structure during constant structure depressurization. A steady-state mass balance of ^{222}Rn in the structure was used to calculate the soil-gas entry rate. Radon sources include advective entry through the slots, diffusive entry from and through the walls and through the slots, and unintentional, nonslot leakage below grade. The contribution of radon from outdoor air is negligible. Sinks include losses by ventilation and decay. With the sources and sinks given in the order mentioned, the mass-balance equation is

$$(4) \qquad Q_{sl}R_{sl} + S_d + Q_{ns}R_{ns} = R_{in}\,Q_{ex} + R_{in}\lambda\,V$$

where Q_{sl} and Q_{ns} are the soil-gas flow rates through the slots and nonslot leaks (m^3/s), R_{sl} and R_{ns} are the associated ^{222}Rn concentrations (Bq/m^3); S_d is the radon entry by diffusive from the walls and through the slots (Bq/s^1), R_{in} is the ^{222}Rn concentration in the structure (Bq/m^3), Q_{ex} is the exhaust flow from the structure (m^3/s); λ is the decay constant of ^{222}Rn (2.1×10^{-6} s^{-1}), and V is the structure volume (13.4 m^3).

Some of the parameters in Eq. 4 (R_{in}, R_{sl}, Q_{ex}) are measured during the advection experiments; others are determined from earlier measurements. Rn entering by diffusion through or from the walls is estimated to be 300 Bq/hr from diffusion canister measurements made in the east structure at the Ben Lomond site. The contribution of diffusion through the slots is calculated using Fick's law and the measured concentration difference across the slots. In general, the total contribution from diffusion during an advective entry experiment is small relative to the advective component. For example, in an experiment discussed below in which the structure was held at -21 Pa, ~20 Bq/s entered by advection of ^{222}Rn, while only about 0.09 and 0.001 Bq/s entered by diffusion of ^{222}Rn through and from the walls and through slots, respectively. See Chapter VI Appendix for a complete discussion of radon diffusion from and through the walls.

The soil-gas entry rate is given by the sum of Q_{sl} and Q_{ns}. An upper bound was determined for Q_{ns} by an experiment in which we depressurized the structure by 100 Pa with the slots sealed. In that case, Q_{sl} in Eq. 4 is zero, and we can solve for Q_{ns} given R_{ns}. Since we have no way of knowing the spatial distribution of possible nonslot leaks we make two assumptions. Our best estimate assumes that nonslot leakage is distributed uniformly over the walls and floors, so that R_{ns} is given by the area-weighted average of ^{222}Rn concentrations measured in the high-wall, mid-wall, low-wall, and subslab probes nearest the structure. A highest estimate of the nonslot entry is obtained by assuming that all leakage occurs in the high-wall region where the ^{222}Rn concentrations are lowest. The best and maximum estimates of nonslot leakage *with the slots sealed* are 0.13 and 0.40 L min^{-1} Pa^{-1} (2.2 x 10^{-6} and 6.7 x 10^{-6} m^3 s^{-1} Pa^{-1}), respectively.

The values of Q_{ns} and R_{ns} for the advection experiments with the slots open are modified to account for the change in the across-shell driving pressures relative to when the slots are sealed. Because of the mitigating effect of flow through the slots, given the same structure depressurization, points closer to the slots have considerably reduced driving pressures with the slots open. Therefore, the best estimates of Q_{ns} and R_{ns} during depressurization with slots open are obtained by weighting the relative driving pressures and concentrations measured in each of the four regions (high-wall, mid-wall, low-wall, and subslab) assuming that the leakage area is uniformly distributed over the four regions. Given our best estimates of Q_{ns} and Q_{sl}, nonslot below-grade entry constitutes ~8% of total soil-gas entry.

Figure 5 shows the maximum, minimum, and best estimates of soil-gas entry rate vs. depressurization based on the radon balance given in Eq. 4. The maximum and minimum values of Q_{sl} incorporate both the maximum uncertainty in Q_{ns} and the propagation of error from other measured parameters. As expected for Darcy flow through soil, the relationship is linear ($r^2 = 0.995$ for the weighted fit shown in the figure). Notice that there is no significant difference between the entry measured in May and September, 1991. We conclude, therefore, that at this site seasonal changes in soil characteristics do not result in significant changes in soil-gas entry that are sustained over time. However, at sites that receive sufficiently heavy and frequent rain, such that much of the soil horizon becomes saturated at once, significant suppression of soil-gas entry might occur.

NUMERICAL MODELING AND COMPARISON WITH EXPERIMENTS

This section describes the use of a three-dimensional finite-difference model to simulate the conditions of the advective entry experiment of September 25, 1991, given the average regional soil permeabilities measured on October 1, 1991, as inputs. (The September 25 data were for a low-wind period during the experiment begun on September 19, 1991, as indicated on Figure 5.) The model predictions of pressure coupling and soil-gas entry are compared with the results of experiments described in the previous section.

Based on a code written by Loureiro *et al.* [20], the model was designed to simulate soil-gas and radon transport under steady-state conditions, in three dimensions, providing predictions of the soil pressure field and soil-gas entry rate. The model assumes isothermal conditions and Darcy flow, and restricts soil-gas entry to occur via gaps in the structure floor (the walls and floors being otherwise impermeable). The gaps are assumed to provide no resistance to flow, a reasonable assumption given the slot width in the structure. The soil is assumed to be piecewise homogeneous and isotropic. The porosity, permeability, and soil density can vary among regions.

To check the physics of the numerical model, we compared the soil-gas entry prediction of a simplified, cylindrical version of the three-dimensional Cartesian model used here with the analytical solution for flow into a horizontal buried cylinder. The cylindrical numerical-model is described in

Revzan *et al.* [12]. The analytical solution, using bipolar coordinates, is described in Morse and Feshbach ([21], pp. 1210-1211). First we compare the solutions of the two numerical models to establish the validity of using the cylindrical model as a substitute for the Cartesian model. Soil-gas entry predictions of the cylindrical numerical-model were consistently ~8% higher than predictions of the Cartesian model. This discrepancy is probably explained by the cylindrical idealization of the geometry of the Ben Lomond structure.

The entry prediction of the bipolar analytical-model was modified to mimic the geometry of entry into a gap in a floor slab by ignoring entry from elevations above the cylindrical-gap level, *i.e.*, the region blocked by the presence of the structure. The prediction of the bipolar model exceeds that of the cylindrical model by no more than 25%, and the discrepancy is considerably smaller if we acknowledge that flow coming from the quadrant in the direction of the center of the structure would be considerably diminished by horizontal expanse of impermeable slab. The soil-gas entry prediction of the bipolar model therefore exceeds that of the Cartesian model by no more than 33%—providing a crude validation of the numerical solutions.

The model simulates flow in a quarter block of soil (for example, from the center of the structure to the north, and from the center of the structure to the east). Symmetry is assumed in opposing quadrants. For the purpose of the modeling, the soil at the Ben Lomond site was divided into the following regions: upper backfill, between the soil surface and 1.3-m depth; lower backfill, between 1.3 and 1.9 m; natural surface soil from the surface to 0.5 m depth; natural soil lying below 0.5 m depth; and subslab gravel extending 0.10 m below the floor slab and lying within the wall footers. The arithmetic mean of the soil permeabilities were determined for each region using the data for October 1, 1991, in Table I.[4] Gravel permeability was determined

---

[4] As indicated in Table I, notes a and b, the determination of the average permeability of the bulk soil excluded measurements, the values of which are marked as being below the detection limit. Subsequent analysis of the seasonal data for these probes showed that these were not measurement errors, but that the soil permeability was indeed lower than the detection limits listed in the table. The estimate of average permeability for the bulk soil that is quoted here is, therefore, somewhat high. In Chapter VI, the estimate of the average permeability of the

using laboratory soil-column measurements and was found to be 2.0 x 10^{-8} m^2 [15].

Figures 3 and 4 compare the measured and modeled pressure coupling. Predictions at subslab probes agree well with the measured values, especially near the gravel layer. At the low-wall level, however, there is a significant discrepancy between the modeled and measured values. Moreover, the relative magnitude of this discrepancy increases as we move toward the soil surface. Although this discrepancy is greatest in the near-surface soil, the experimental uncertainty is also larger there, so our confidence in the estimation of the magnitude of the discrepancy is lower than for the mid-wall and low-level levels.

Particularly notable is the discrepancy between the measured and predicted pressure coupling in the far-field soil at the low-wall and mid-wall levels. There, observed coupling is 3 – 6 times larger than the model predicts, ignoring the anomalous low-wall, medium length probe on the west side of the structure which shows even larger disagreement between measured and modeled coupling. That probe violates the predicted trend of higher pressure coupling existing nearer the structure walls. This violation is also apparent in the measurements in the near-surface probes, but the relative uncertainties in the measured values are considerably larger there.

The higher than expected pressure coupling observed in the far-field raised the possibility of the existence of a high permeability zone occurring in a sleeve around the probe due to disturbance during probe installation. Such a zone would make the pressure at the probe tip reflect the near-wall, highly coupled region. To test this possibility, thin open-end probes were installed vertically from the soil surface at horizontal distances corresponding to the existing medium and long probes. Pressure coupling measured with these probes agreed well with the results of measurements made with the permanently installed probes.

Figure 5 indicates the soil-gas entry rate predicted by the model for the conditions of the September 25, 1991, advection experiment, based on the permeabilities measured at the soil probes and extrapolated to other driving

---

bulk soil was revised to include those probes which were considered to be *at* the detection limit, thereby yielding a new upper estimate of average soil permeability based on the available data.

pressures by assuming the same soil conditions. The model underpredicts the measured best estimate of soil-gas entry rate (from Eq. 4) by a factor of ~7.[5] The model predicts an entry rate of only 3.1 L/min (4.3 x 10^{-5} m^3/s) relative to the radon-balance estimate of 21 L min^{-1} (3.5 x 10^{-4} m^3/s) at an indoor-outdoor pressure difference of 21 Pa.[6] Even the minimum radon-based estimate of soil-gas entry of 18 L/min (2.5 x 10^{-4} m^3/s) is a factor of 6 higher than predicted by the model.

To further investigate the nature of this discrepancy, we ran the model again at the same structure pressure, but using the highest values of soil permeabilities measured in each soil region rather than the average. At 7 L/min (1.2 x 10^{-4} m^3/s), the model prediction is still a factor of 3 below the best radon-balance estimate of soil-gas entry, and a factor of 2.6 below the minimum estimate. The possible existence of non-Darcy flow near the soil-gas entry locations was dismissed as a possible explanation, since the inertial effects of non-Darcy flow increase the effective soil resistance, thereby suppressing, not enhancing, the entry rate.

As an additional check on the performance of our numerical model, we compared the predictions of soil-gas entry and pressure coupling of the simplified cylindrical model derived from it (discussed above) with results of an independently developed, two-dimensional finite-difference model and measurements reported by Andersen [22]. Again, regionally averaged measured permeabilities were used as inputs to the model. Andersen's measurements were made at a small test structure, 0.5-m deep, that, like our structure, is located in natural soil and underlain by gravel. Both Andersen's and our model agreed well with pressure coupling measured 1.2 m from the wall of the small test-structure and 0.26 m below the soil surface. Andersen's prediction, our prediction, and the measured value were: 0.6%, 0.7%, and 0.5%, respectively. When scaled to the small test structure, this is the vicinity in which our model gave the worst agreement with measurements made at the Ben Lomond site. Both of the models, however, underpredict the measured soil-gas entry rate at -10 Pa depressurization by a factor of ~20. As

---

[5] See footnote 1, this chapter.

[6] The modeling of the soil-gas entry rate was revised in Chapter VI based on data available subsequent to publication of this Chapter (see footnote 1, this chapter). The revised prediction of the soil-gas entry rate, based on that analysis is 2.4 L/min.

with our model, even when Andersen used the highest measured permeabilities for the soil, the model still underpredicted the measured entry rate. The fact that pressure measurements agree with the model whereas entry measurements do not is an indication that the sources of the two discrepancies found in the Ben Lomond measurements may not be the same. This is discussed in greater detail below.

DISCUSSION

There are three key findings of this chapter:

(1) The observed soil-gas entry rate exceeds that predicted by the numerical model by a factor of ~7,[7] given the arithmetic mean of soil permeabilities measured in different regions of the soil as inputs to the model.

(2) Similarly, the observed pressure coupling between the structure and the far-field soil exceeds the model predictions. This was most evident in the mid- and low-wall-level soil 2 m from the structure, where measured values exceeded predicted values by factors of approximately 6 and 3, respectively.

(3) The soil-gas entry rate as a function of structure depressurization was insensitive to reasonably large seasonal changes in near-surface soil permeability.

The source of the model-measurement discrepancies of soil-gas entry and pressure coupling may well not be the same, since these parameters can vary independently, as the following example illustrates: Given that the slots provide insignificant resistance to flow (a good assumption in the present case) if soil permeability in all regions is doubled, the predicted soil-gas entry rate will also double, but the pressure coupling will be unchanged. We offer a hypothesis to explain the model-measurement discrepancies in soil-gas entry and pressure coupling below.

Underprediction of soil-gas entry could result from systematic bias in the soil permeability measurements or from the existence of high-permeability flow paths not detected by our network of probes. Preferred flow

---

[7] See footnote 1, this chapter.

paths from different sources could produce different aspects of the observed discrepancies. The difference in the physical properties of the soil and structure walls and floor might result in a thin high-permeability sleeve around the structure, enhancing flow along that path. A network of paths might be present in the bulk soil as a result of burrowing by soil fauna or the growth of tree roots. Indeed, animal burrows were observed down to a depth of 3 m in a trench dug ~20 m southeast of the structure, and 70 roots were observed in an area of ~4 m^2 [22]. Lastly, high-permeability flow path or channel between the gravel and the probe tip could explain the anomalously high pressure coupling observed in the medium-length probe on the west side of the structure.

The remainder of this thesis describes intensive testing of the second hypothesis that a network of preferred flow paths through the soil results in underestimation of effective permeability of the soil at the structure scale when determined from multiple smaller-scale permeability measurements. If spatially infrequent, preferred flow paths are the explanation for the underprediction of soil-gas entry, then use of the type of soil-probe permeability measurements utilized here to assess the radon entry potential into homes, as previously suggested [23], could yield significantly misleading results since it is impractical to probe complex field sites even as thoroughly as this controlled site. If spatially infrequent flow paths in the bulk soil cause the observed discrepancy in soil-gas flow rate, then the effect should be largest in houses with below-slab gravel since the gravel acts as a plenum communicating structure depressurization to a significantly larger region of soil than would cracks or gaps alone, increasing the probability of intercepting spatially infrequent, high-flow channels. Steady-state experiments planned at the second structure at the same site, which has no gravel under the slab, should help resolve this question. On the other hand, if hierarchically nested, or finely graded scales of increasing permeability are the cause, a plenum would not have as significant an effect.

Two mechanisms that could explain the underprediction of the horizontal extension of the pressure field are anisotropy or heterogeneity of soil permeability. Anisotropy would require higher horizontal than vertical permeabilities. Heterogeneity could spread the pressure field by soil layering [13] or if soil permeability increased significantly with increasing distance from the structure.

Observable regional differences in soil permeability were included in the model but did *not* produce the observed pressure field. It is possible that our network of soil probes does not capture the existence of a thin but important layer with different soil permeability. This appears unlikely, however, because, although there was indication of physical and chemical changes in soil with depth during soil excavation [17], permeability measurements made on soil cores sampled from different horizons did not indicate the presence of such a layer [24]. Soil anisotropy is measured in Chapters III and VI, and its effect on the modeled pressure field is described in Chapter VI.

The insensitivity of soil-gas entry to significant seasonal changes in near-surface soil permeability can be explained by the fact that the air permeability of much of the soil-gas transport path is unchanging during the year. Furthermore, because the soil-gas velocity field converges toward the gravel, the net permeability of the soil is most strongly influenced by conditions near the gravel, where average permeability remains relatively constant for several reasons. The region is somewhat protected by the structure; water leached to the deep soil is channeled and dispersed, increasing the spatial variability of permeability and reducing the average moisture content; in addition, loss of water to the surface from evaporation and transpiration reduces transport of water to the deep soil. The gravel itself plays an insignificant role in determining the net permeability of the soil pathway because its permeability is so much higher than that of the natural soil and should remain fairly constant since its water retention potential is minimal.

CONCLUSIONS

Experiments were conducted at an extensively instrumented basement structure located in natural soil and designed for the study of soil-gas and radon transport. These experiments were used to investigate the effect of seasonal changes in soil conditions on pressure-driven soil-gas entry rates and to test a persistent observation from field studies that models consistently underpredict the measured entry rate.

This study found *no* measurable seasonal change in pressure-driven soil-gas entry or in pressure coupling between the structure and the soil as a result of seasonal changes in soil moisture and soil permeability, despite large seasonal changes in near-surface soil conditions due to significant temporal variability in precipitation. This appears to be a result of the fact that soil conditions near the entry slots in the floor slab are relatively constant. This suggests that, at least in climates lacking extreme and sustained seasonal changes in soil conditions, the major factor affecting advective entry of contaminants from the soil into basements should be changes in driving pressures due to variation in indoor-to-outdoor temperature differences, in operation of ventilation systems and wind speed, and possibly in patterns of barometric pressure fluctuation. Structures for which entry typically occurs close to the surface, such as slab-on-grade or crawl-space houses, have greater potential to be affected by seasonal changes in soil conditions. Houses in extreme climates, particularly those where the soil freezes seasonally, might see significant seasonal changes in soil-gas entry.

Experiments on soil-gas entry as a function of structure depressurization and on pressure coupling between the structure and the soil were compared with the results of a three-dimensional model of soil-gas transport. Our results corroborate the findings of field studies conducted at existing houses in which significant model-measurement discrepancies were observed. These discrepancies had previously been attributed to poor understanding of inherently complex field sites. The models significantly underpredict soil-gas entry rate as a function of structure depressurization and, to a lesser extent, also underpredict pressure coupling. At the Ben Lomond test structure, the soil-gas entry rate was underpredicted by a factor of ~7.

The fact that this model underprediction persists despite significant reduction of the uncertainties to model inputs provided by the controlled and extensively monitored experimental structure suggests the possibility that conditions at this site, and possibly at real houses, are inconsistent with the model assumptions or that the typical method of assessing regional soil permeability (an input to the model) can be misleading. This work indicates possible sources of these discrepancies that will be tested at the site in the future.

Resolving these discrepancies at the Ben Lomond site will improve our understanding of the entry of contaminant-bearing soil gas into real houses. In particular, this understanding should assist us in achieving our policy goals for radon control in the following ways:

(1) Use of geological studies is an often cited tactic for finding regions with large potential for high indoor radon concentrations. If it is determined that improper soil characterization is causing the model-measurement discrepancy in soil-gas entry into houses, then different measurement techniques might be required for site assessment, or new studies might be required to correlate regions of high radon potential with existing geological information.

(2) Models are currently being used as tools for assessing radon mitigation technologies for different environmental conditions and housing types. If these models can be properly validated, we can have greater confidence in the model predictions. If we find that some unforeseen structure of soil characteristic(s) is causing the large model-measurement discrepancy, this (these) factor(s) should be incorporated in the models during theoretical testing of mitigation technologies.

(3) Models and better conceptual understanding of the radon entry problem can also be used to develop rational and cost-effective building guidelines for new homes that would minimize indoor exposures to radon progeny and other contaminants.

REFERENCES

1. Bruno, R.C., Sources of indoor radon in houses: A review, *Journal of the Air Pollution Control Association*, 1983, 33: 105-109.

2. Åkerblom, G., Anderson, P. and Clavensjo, B., Soil gas radon—A source of indoor radon daughters, *Radiation Protection Dosimetry*, 1984, 7: 49-54.

3. Nero, A.V. and Nazaroff, W.W., Characterizing the source of radon indoors, *Radiation Protection and Dosimetry*, 1984, 7: 23-39.

4. Nazaroff, W.W. and Doyle, S.M., Radon entry into houses having a crawl space, *Health Physics*, 1985, 48: 265-281.

5. Nazaroff, W.W., Lewis, S.R., Doyle, S.M., Moed, B.A. and Nero, A.V., Experiments on pollutant transport from soil into residential basements by pressure-driven airflow, *Environmental Science and Technology*, 1987, 21: 459-466.

6. Turk, B.H., Prill, R.J., Grimsrud, D.T., Moed, B.A. and Sextro, R.G., *Radon and Remedial Action in Spokane Valley Homes, Volume I: Experimental Design and Data Analysis.* LBL-23430, Lawrence Berkeley Laboratory, Berkeley, CA: 1987.

7. Hodgson, A.T., Garbesi, K., Sextro, R.G. and Daisey, J.M., Soil-gas contamination and entry of volatile organic compounds into a house near a landfill., *Journal of the Air and Waste Management Association;* 1992, 42: 277-283.

8. Nazaroff, W.W., Moed, B.A. and Sextro, R.G., Soil as a source of indoor radon: Generation, migration, and entry. In: *Radon and Its Decay Products in Indoor Air*, Nazaroff, W. W. and Nero, A. V. J., Ed. John Wiley and Sons: New York, 1988, 57-112.

9. Narasimhan, T.N., Tsang, Y.W. and Holman, H.Y., On the potential importance of transient air flow in advective radon entry into buildings, *Geophysical Research Letters*, 1990, 17: 821-824.

10. Tsang, Y.W. and Narasimhan, T.N., Effects of periodic atmospheric pressure variation on radon entry into buildings, *Journal of Geophysical Research*, 1992, 97: 9161-9170.

11. Hintenlang, D.E. and Al-Ahmady, K.K., Pressure differentials for radon entry coupled to periodic atmospheric pressure variations, *Indoor Air*, 1992, 2: 208-215.

12. Revzan, K.L., Fisk, W.J. and Gadgil, A.J., Modeling radon entry into houses with basements: Model description and verification, *Indoor Air*, 1991, 1: 173-189.

13. Garbesi, K. and Sextro, R.G., Modeling and field evidence of pressure-driven entry of soil gas into a house through permeable below-grade walls, *Environmental Science and Technology*, 1989, 23: 1481-1487.

14. Fisk, W.J., Flexser, S., Gadgil, A.J., Holman, H.Y., Modera, M.P., Narasimhan, T.N., Nuzum, T., Revzan, K.L., Sextro, R.G., Smith, A.R., Tsang, Y.W. and Wollenberg, H.A., *Monitoring and Modeling for Radon Entry into Basements: A Status Report for the Small Structures Project*. LBL-27692, Lawrence Berkeley Laboratory: Berkeley, CA: 1989.

15. Fisk, W.J., Modera, M.P., Sextro, R.G., Garbesi, K., Wollenberg, H.A., Narasimhan, T.N., Nuzum, T. and Tsang, Y.W., *Radon Entry into Basements: Approach, Experimental Structures, and Instrumentation of the Small Structures Project*. LBL-31864, Lawrence Berkeley Laboratory: Berkeley, CA: 1992.

16. Hillel, *Fundamentals of Soil Physics*, Academic Press: New York, 1980.

17. Flexser, S., Wollenberg, H.A. and Smith, A.R., *Distribution of Radon Sources and Effects on Radon Emanation in Granitic Soil at Ben Lomond, California.* LBL-31915, Lawrence Berkeley Laboratory, Berkeley, CA: 1992.

18. Sherman, M., *Air infiltration in buildings.* American Institute of Physics: 1985.

19. Busigin, A., van der Vooren, A.W. and Phillips, C.R., Interpretation of the response of continuous radon monitors to transient radon concentrations, *Health Physics*, 1979, 37: 659-667.

20. Loureiro, C.O., Abriola, L.M., Martin, J.E. and Sextro, R.G., Environmental Science and Technology, 1990, 24: 1338-1348.

21. Morse, P.M. and Feshbach, H., *Methods of Theoretical Physics,* McGraw-Hill: New York, 1953.

22. Andersen, C.E., *Entry of Soil-Gas and Radon into Houses.* Riso-R-623(EN), Riso National Laboratory, Roskilde, Denmark: 1992.

23. Nazaroff, W.W. and Sextro, R.G., Technique for measuring the indoor ^{222}Rn potential of soil, *Environmental Science and Technology,* 1989, 23: 451-458.

24. Flexser, S., Lawrence Berkeley Laboratory, Berkeley, CA, personal communication, February 18, 1992.

Table I. A comparison of measurements of permeability of soil to air made at 30 probes on the two dates with the highest and lowest average measured permeabilities. Multiply table values by 10^{-13} to obtain permeabilities in m^2. Uncertainties are dominated by environmental noise in the measured values of pressure and flow.

Measurement Date->	**October 1, 1991**	**January 7, 1992**
High-wall probes	Backfill Region	
E	29 ± 2.0	10. ± 0.7
W	30 ± 2.0	4.4± 1.4
S	37 ± 2.5	8.7± 0.6
N	26 ± 1.8	9.4± 0.7
Avg.	31	8.1
	Natural Soil	
E (medium)	22 ± 2.0	2.2± 0.5
W (medium)	18 ± 1.2	1.5± 0.2
S(long)	240 ±23.	69. ± 4.9
N(long)	28 ± 1.9	1.7± 0.3
Avg.	77	19
Mid-wall probes	Backfill Region	
E	20 ± 2.3	21. ± 2.9
W	17 ± 1.2	6.8± 0.5
S	30 ± 2.0	11. ± 0.8
N	20 ± 1.3	14. ± 1.0
Avg.	22	13
	Natural Soil	
E (medium)	75 ± 5.4	41. ± 2.7
W (medium)	91 ± 6.2	48. ± 3.8
S(long)	83 ± 5.7	40. ± 2.7
N(long)	100 ± 7.2	61. ± 4.5
Avg.	87	45
Low-wall probes	Backfill Region	
E	39 ± 5.4	42. ± 3.9
W	73 ±17.	89. ±12.
S	52 ± 8.9	49. ± 6.5
N	45 ± 5.2	49. ± 6.1
Avg.	52	57
	Natural Soil	
E (medium)	190. ±80.	160. ±47.
W(medium)	2.0± 0.3	5.9± 0.5
S(long)	35. ± 3.8	18. ± 1.7
N(long)	< 1.8	< 1.6
Avg.(a)	76	61

Table I. continued

Sub-slab probes		
(short)	64. ± 4.6	73. ± 5.0
(short)	44. ± 3.0	43. ± 3.0
(medium)	< 1.8	< 1.6
(medium)	170. ±12	170. ±13.
(medium)	< 1.9	1.6± 0.2
(long)	11. ± 1.1	12. ± 1.3
Avg.(b)	72	75

(a) Only first three values included in average.

(b) First, second, third, and fifth values included in average.

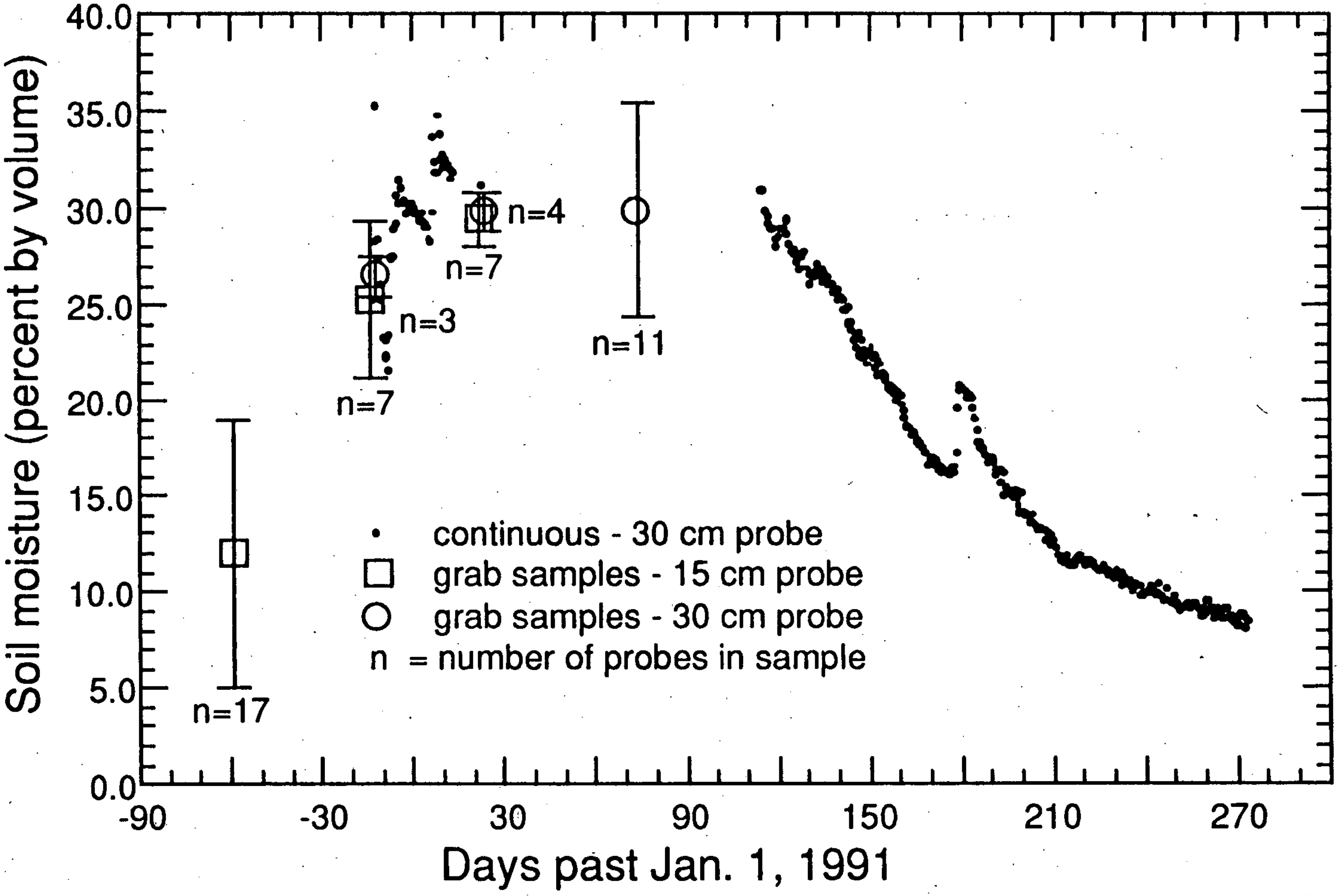

Figure 1. Grab samples and continuous measurements of soil moisture around the Ben Lomond structure. The vertical bars on the grab sample data show spatial variability as indicated by the sample standard deviation of measurements made on a single day at n different locations.

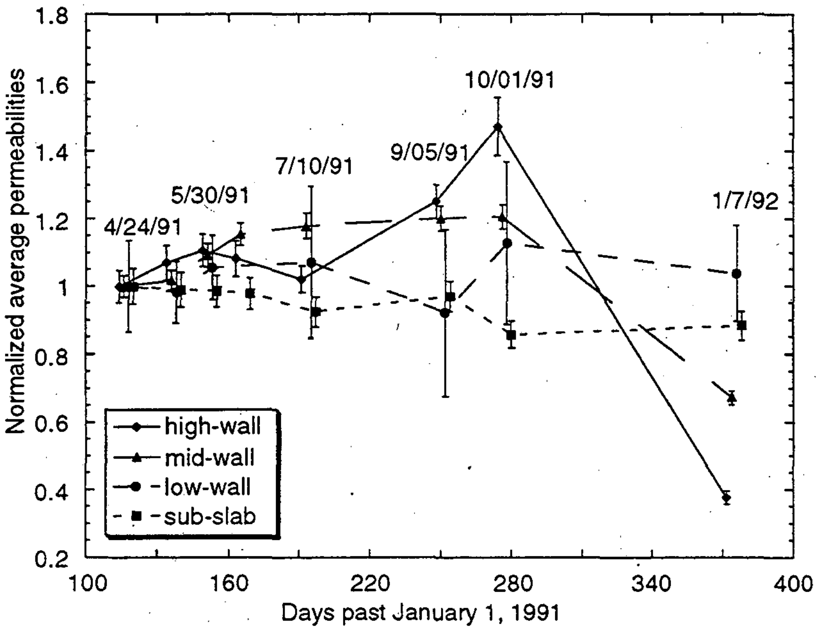

Figure 2. Seasonal trends in average air permeabilities of the soil in the high-wall, mid-wall, low-wall, and subslab regions. The averaged values are normalized with respect to their value on April 24, 1991. Only probes with complete data sets are included (seven, eight, five, and four probes in the high-, mid-, and low-wall, and subslab- levels, respectively). Vertical bars indicate the standard error in the mean values.

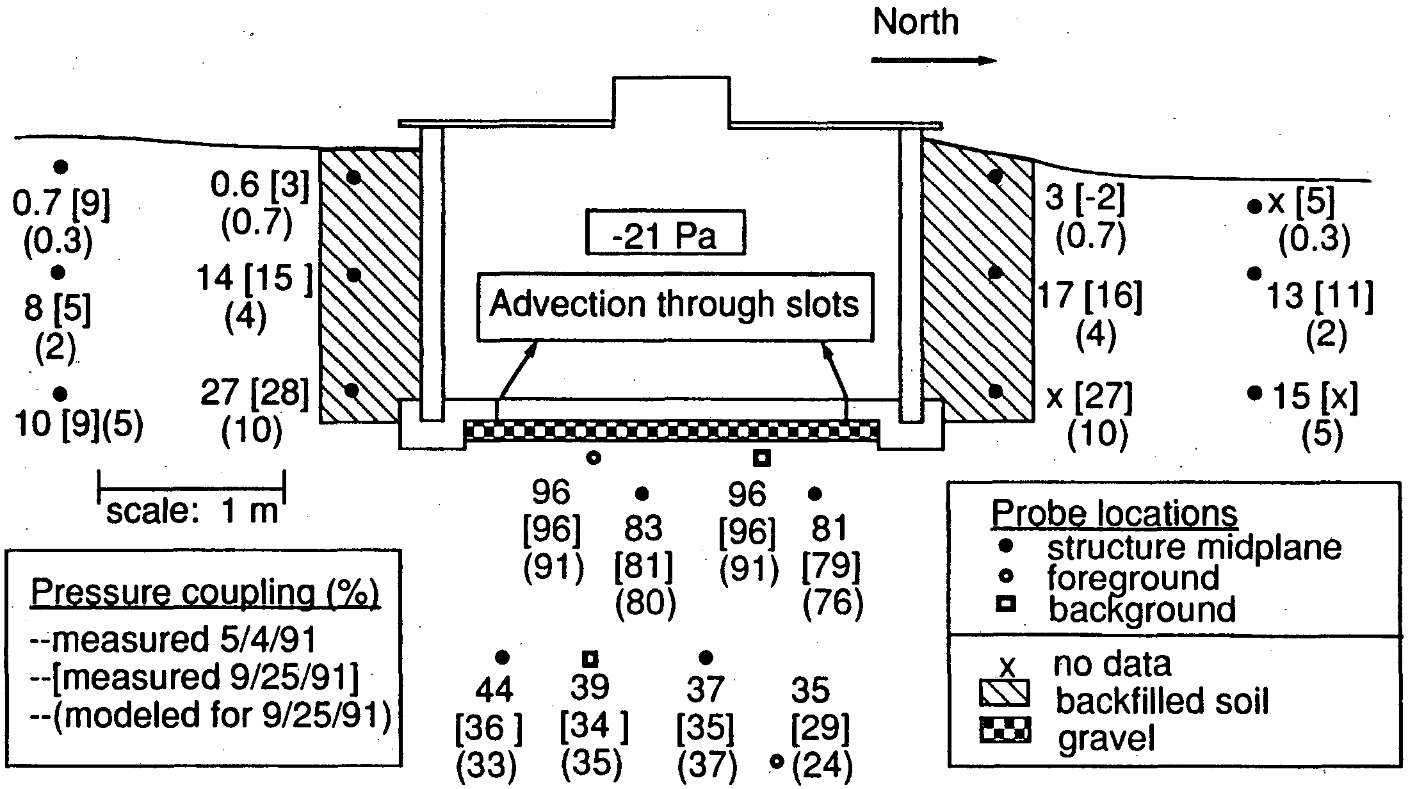

Figure 3. North/south cross section of the Ben Lomond site showing measured and predicted pressure coupling at the probe locations. Measurements were made on May 4, 1991, and September 25, 1991, at 19- and 21-Pa structure depressurization, respectively, and have an uncertainty of ±4%. The numerical model was run given regional average permeabilities measured on October 1, 1991, and assuming 21 Pa structure depressurization.

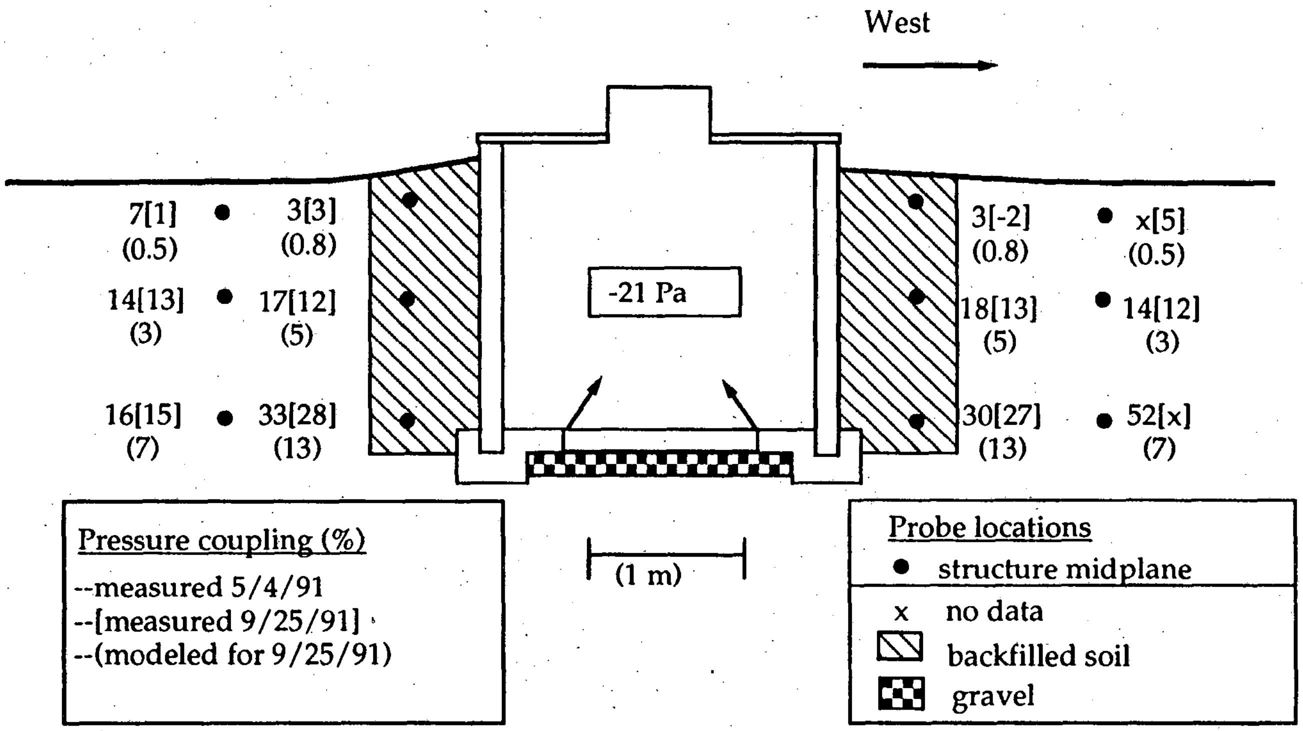

Figure 4. East/west cross section of the Ben Lomond site showing measured and predicted pressure coupling at the probe locations. Measurements and modeling are as in Figure 3.

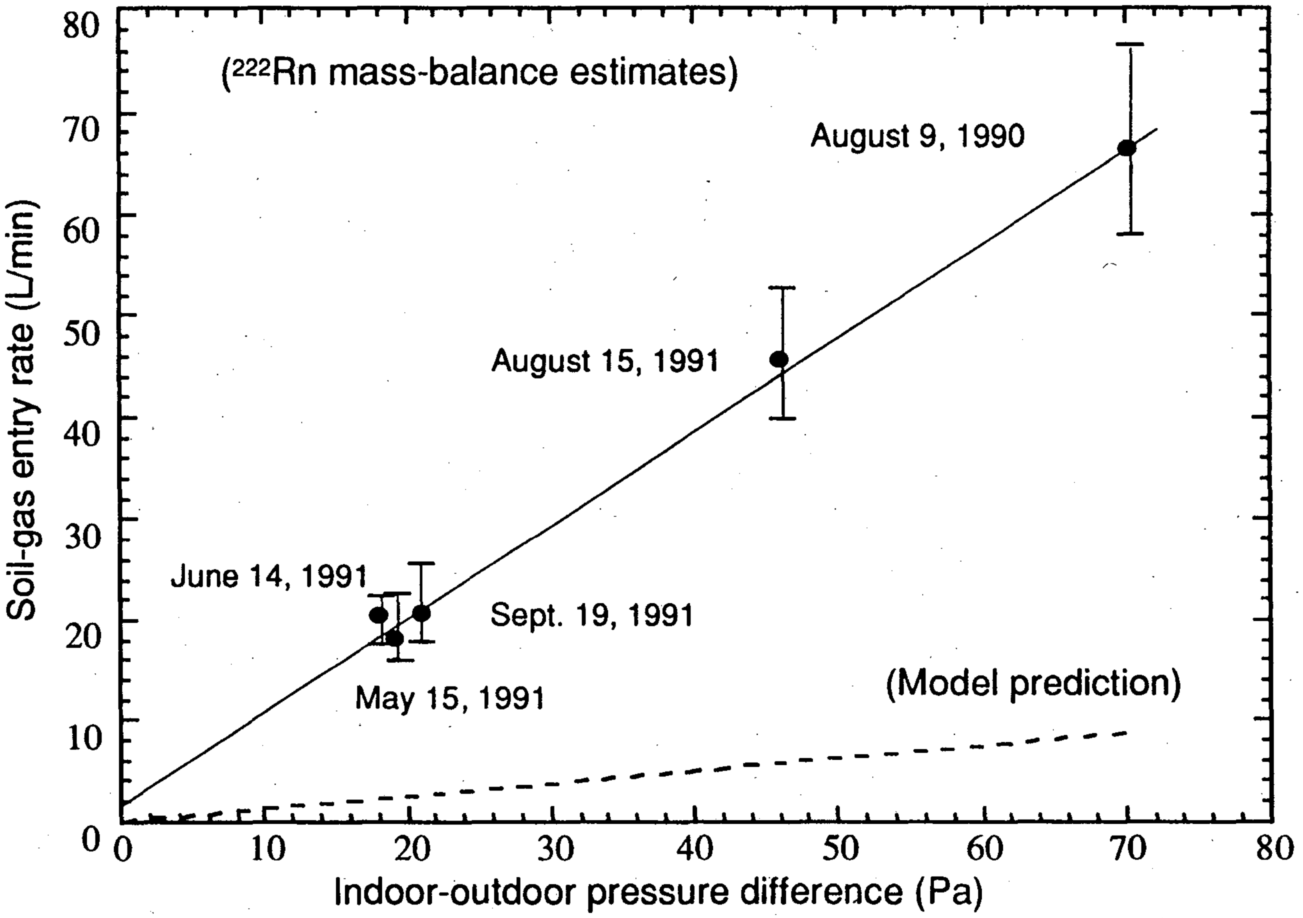

Figure 5. Soil-gas entry rate vs. structure depressurization in the Ben Lomond west structure. The entry rate is determined from radon mass-balance measurements in the structure during advection experiments and by the numerical model using measured soil permeabilities as inputs. The vertical bars indicate the maximum and minumum estimates of entry based on uncertainty in the amount of nonslot, below-grade leakage, and on propagation of error of the measured parmeters.

APPENDIX

Effective Leakage Area of Structure

A low total area of uncontrolled leakage into the structure is desired to minimize uncertainty in the magnitude and location of advective entry into the structure. To quantify leakage into the structure we use the concept of effective leakage area (ELA) described in Sherman [1].

First, the leakage equation is given by

$$(1) \qquad Q = K\Delta P^{n} \ ,$$

where Q is the total exhaust flow from the structure used to induce a dynamic pressure difference between the structure and outdoors of ΔP. Measurements are made at many pressures, both positive and negative. K and n are then determined by regression analysis.

The ELA is defined as

$$(2) \qquad ELA = \frac{K\Delta P_r^{n}}{\sqrt{\frac{2}{\rho}\Delta P_r}} \ ,$$

where ELA is in units of m^2, ΔP_r is the reference dynamic pressure difference of 4 Pa, ρ is the density of air (1.2 kg/m^3), and $K\Delta P^n$ has units of m^3/s.

The ELA of the structure was measured first with the slots open, then sealed. The leakage equations and ELAs are shown in Table A-I for both experiments. The approximate slot ELA is estimated from the difference. Note that this is only approximate because the pressure field in the soil is modified by sealing the slots. That is, the pressure difference across the slab near the sealed slots is larger with the slots sealed than open. Therefore, when the slots are open, the non-slot leakage may well be less than what it is estimated to be by sealing the slots. The estimated uncontrolled leakage (slots sealed) of 0.12 cm^2 is well within the design goal for the structure.

Note that because of the relationship between the exponents in the leakage equations, as the indoor-outdoor pressure difference increases, the contribution to entry from the soil increases relative to the contribution from the atmosphere.

Table A-1. Leakage equations and effective leakage area of the structure.

Experiment configuration	**Leakage equation (Q in L/min ΔP in Pa)**	**ELA ($\times 10^{-4}$ m^2)**
slots open	$Q_o = 0.93\ \Delta P^{1.0}$	0.24
slots closed	$Q_c = 0.56 \Delta P^{0.88}$	0.12
slots only	(not measured directly)	0.12[a]

[a] Estimated using: ELA(slots open) - ELA(closed).

REFERENCES

1. Sherman, M. *Air infiltration in buildings.* American Institute of Physics: 1985.

CHAPTER III

A Dynamic Pressure Technique for Estimating Permeability and Anisotropy of Soil to Air Flow over Variable Length Scales*

SYNOPSIS

A technique was developed that measures the diffusivity of a dynamic pressure signal through soil over variable length scales. Given a known soil porosity, the technique can be used to determine the effective permeability of soil to air. A sinusoidally oscillating pressure signal, imposed at a source probe, is recorded at a detector probe. The time lag between the imposed and detected signals is used to determine the effective permeability along the path between the probes. The technique improves upon previous methods by offering relatively unweighted and longer integration paths. Arbitrary location of the detector probe also allows the detection of anisotropy in permeability. A field test of the technique was carried out at the site of the Small Structures Project radon transport experiment in Ben Lomond, California [1, 2]. Comparisons of the results of the dynamic permeability measurements made at the 2 – 3 m scale with static permeability measurements that integrate over 0.1 – 0.5 m indicate a length dependence of soil permeability at this site. The field experiment also indicated the presence of horizontal-vertical anisotropy, with horizontal permeability exceeding vertical by a factor ~2. The tentative finding of scale-dependent permeability is substantiated by the work in Chapters IV, V, and VI.

---

* This chapter is a substantially revised version of a paper previously published as: Garbesi, K., Sextro, R.G. and Nazaroff, W.W. *A dynamic pressure technique for estimating permeability and anisotropy of soil to air flow over a scale of several meters.* LBL-32723.; Lawrence Berkeley Laboratory: 1992.

INTRODUCTION

High indoor radon concentrations have been demonstrated to result primarily from advective entry of radon-bearing soil gas into houses through gaps in the substructures [3-12]. Because of their large size and geometries, houses are likely to interact with the soil at a scale of several meters or more, drawing in soil-gas-borne contaminants such as radon and volatile organic compounds. It is useful to characterize the permeability of soil to air over path lengths of several meters, since houses, The actual scale(s) at which a given house interacts with the soil will depend on many factors: the depth of the locations at which soil gas enters the house, the size and shape of the gaps, cracks, or holes in the substructure, the presence or absence of gravel layer, and the details of the structure of the soil. It is also useful to have larger-scale permeability assessment techniques than were available in the past to study contaminant transport in other applications such as above contaminated ground water or nonaqueous-phase liquid plumes.

Field studies of the entry of radon and VOC into houses have characterized soil permeability using static techniques that impose a constant flow of air through a soil probe. Permeability is inferred from the known flow rate and from measurements of the pressure difference between the probe and the soil surface [12-15]. Because of practical constraints on probe size, integration of the information about soil permeability is limited to a relatively small distance from the source (~0.1-0.5 m radius) [2].

Typically, to determine regional soil permeabilities for use in soil-gas transport models, many of these small-scale measurements are averaged together. Persistent discrepancies between modeled and measured soil-gas and radon entry rates into houses suggest that small-scale measurements might not reflect soil characteristics at the larger scales at which houses typically interact with soils [15]. It is therefore desirable to have a measurement technique that integrates over appropriate length scales, and that can be used *in situ* with minimal disturbance to the soil.

Anisotropy of the permeability of soil to air due to small-scale structure—or effective anisotropy due to the presence of larger-scale, homogeneous isotropic layers with distinct permeabilities—is another possible confounding factor in predicting gas-phase contaminant transport through soils. Nazaroff *et al.* [3] and Garbesi and Sextro [13] describe two sites in which there are large discrepancies between measured and modeled pressure coupling between a house and the surrounding soil. In those cases, soil layering or horizontal high-permeability seams, were invoked as possible explanations for the observed discrepancy. Measurements of regional anisotropy of permeability could verify such hypotheses.

Laboratory methods exist for determining anisotropy from field samples [7]. However, these methods have serious limitations in the applications mentioned because of the inherent problem of maintaining sample integrity during the sampling and measurement process, and the need for a large number of samples to determine soil characteristics over the desired scale. Tanner [16] developed a soil probe specifically for the measurement of soil anisotropy. As in the case of other static measurements described above, the probe imposes a localized steady pressure that intrinsically weights information about soil conditions to the near-probe soil. In addition, with a single probe it is not possible to determine the orientation of the anisotropy since information about soil gas motion is integrated at one location.

To overcome these limitations, we have developed a dynamic technique for measuring soil permeabilities over variable length scales given known soil porosity. The technique imposes a sinusoidal pressure oscillation at a source probe that is detected at a second probe. The time lag between the source and detector signals is used to determine the effective permeability of the path between the probes. By varying the location of the detector probe, one can detect anisotropy in soil permeability, or effective anisotropy due to soil layering, along any arbitrary path. Anisotropy is, however, only *approximately* quantified since the reference theoretical system is isotropic.

The goal of this chapter is to describe the development of a technique that can be used to predict Darcy flow through soils, for flows that might occur over various length scales. We want a single measure of soil air-permeability of a given flow path. Effective permeability is therefore defined as the equivalent permeability a homogeneous medium must have to allow the same flow as the inhomogeneous medium at the same driving pressure—where the effective permeability is defined for a given path or soil volume.

This chapter describes the dual-probe dynamic pressure technique for making permeability measurements and develops a mathematical model for analyzing field data. The technique is tested at the site of the Small Structures Project in Ben Lomond, California [1, 2].

THEORY

Model Development

As with any technique for measuring permeability, we require a mathematical model to interpret the measurement data. For the reasons given in the last paragraph of the preceding section, we adopt the usual assumption of a homogeneous medium. In addition, since we have no advance knowledge of the soil when making a measurement, we assume an isotropic medium. Since these are the assumptions used to interpret essentially all field measurements of soil permeability to air, they facilitate comparison with measurements made using other techniques.

The three-dimensional model developed here follows the approach of Fukuda [17] who solved the problem of the one-dimensional propagation of a dynamic pressure signal through soil. The governing equation is derived from the observation that a change of pressure in a volume element of soil is related to a change in the mass of air in that volume, as determined by the ideal gas law. For a representative volume element with dimensions $\Delta x \Delta y \Delta z$ and air-filled porosity ε, the change in the mass of air in the volume that occurs over a time Δt must equal the mass entering the volume minus the mass leaving the volume in the same time increment. Given effective Darcy velocities of the soil gas in the x, y, and z directions,[1] v_x, v_y, and v_z, respectively, this relationship is described by

$$\begin{aligned} &\Delta P^{*}(x,y,z)[\Delta x\Delta y\Delta z]\frac{\varepsilon M}{RT} = \\ (1)\quad &v_x(x,y,z)[\Delta y\Delta z\Delta t]\rho \quad + \quad v_y(x,y,z)[\Delta x\Delta z\Delta t]\rho \quad + \quad v_z(x,y,z)[\Delta x\Delta y\Delta t]\rho \\ &- v_x(x+\Delta x,y,z)[\Delta y\Delta z\Delta t]\rho - v_y(x,y+\Delta y,z)[\Delta x\Delta z\Delta t]\rho - v_z(x,y,z+\Delta z)[\Delta x\Delta y\Delta t]\rho \quad , \end{aligned}$$

where ΔP^{*} is the change in absolute pressure induced by the change in mass, M is the molar weight of air, R is the universal gas constant, T is the temperature, and

---

[1] The Darcy velocity is defined as the volume of fluid per unit time that moves across an imaginary surface in the soil per *total* area (that is, including the area of the soil grains and the interstices).

ρ is the density of the air. The assumptions are made that changes in pressure are small enough that ρ can be considered approximately constant and that changes in temperature throughout the medium may be neglected.

Dividing (1) by ΔxΔyΔzΔt, and taking the limit as Δx, Δy, Δz, and Δt approach zero, we get:

$$(2)\qquad \frac{\partial P^*}{\partial t} = -\frac{RT}{\varepsilon M}\left(\frac{\partial(\rho v_x)}{\partial x} + \frac{\partial(\rho v_y)}{\partial y} + \frac{\partial(\rho v_z)}{\partial z}\right) .$$

The soil-gas velocities under the experimental conditions will be low enough that Darcy's law can be used to describe the resulting flows. For a homogeneous and isotropic model, the x, y, and z components of velocity are then given by

$$(3)\qquad v_x = -\frac{k}{\mu}\frac{\partial P}{\partial x},\quad v_y = -\frac{k}{\mu}\frac{\partial P}{\partial y},\quad v_z = -\frac{k}{\mu}\frac{\partial P}{\partial z} ,$$

where P is called the disturbance pressure (the absolute pressure minus the hydrostatic pressure)[2], k is the permeability of the soil to air, and μ is the dynamic viscosity of soil-gas (taken as the dynamic viscosity of air). We assume isothermal conditions so that μ is constant.

We make the assumption that we can neglect changes in atmospheric pressure under the conditions of the experiment (a condition which is validated by the experimental results). Therefore, in Eq. 2, $\frac{\partial P^*}{\partial t} = \frac{\partial P}{\partial t}$. Using this fact, substituting Eq. 3 into Eq. 2, expanding the derivatives, and collecting like terms, we get

$$(4)\qquad \frac{\partial P}{\partial t} = \frac{k}{\varepsilon\mu}\frac{RT}{M}\left(\rho\nabla^2 P + \frac{\partial\rho}{\partial x}\frac{\partial P}{\partial x} + \frac{\partial\rho}{\partial y}\frac{\partial P}{\partial y} + \frac{\partial\rho}{\partial z}\frac{\partial P}{\partial z}\right) .$$

Using the ideal gas law to substitute P for ρ,

---

[2] For the soil system under consideration, the hydrostatic pressure

$$P_h = P_a - \rho g z$$

where z the Cartesian coordinate taken as zero at the soil surface and is positive in the downward direction.

(5) $$\rho = \frac{M}{RT} P ,$$

and, inserting Eq. 5 into Eq. 4, we obtain the nonlinear partial differential equation:

(6) $$\frac{\partial P}{\partial t} = \frac{k}{\varepsilon\mu}\left(\frac{\rho RT}{M} \nabla^2 P + \left(\frac{\partial P}{\partial x}\right)^2 + \left(\frac{\partial P}{\partial y}\right)^2 + \left(\frac{\partial P}{\partial z}\right)^2 \right) .$$

Since the amplitude of the driving signal in the dynamic pressure measurements is, at its largest, $\leq 10^3$ Pa, to within 1% accuracy we can make the approximation that

(7) $$P_a = \frac{\rho RT}{M} ,$$

where P_a is the mean atmospheric pressure.

This same argument suggests that, if the disturbance pressures are maintained at less one percent of atmospheric pressure, we can simplify Eq. 6 by neglecting the non-linear terms with an estimated error of ~1% or less. This is supported by the following scale analysis:

If

(8) $$\nabla^2 P >> \frac{1}{P_a}\left(\left(\frac{\partial P}{\partial x}\right)^2 + \left(\frac{\partial P}{\partial y}\right)^2 + \left(\frac{\partial P}{\partial z}\right)^2 \right),$$

the scale arguments indicate that

(9) $$1 >> \frac{|P|}{|P_a|} > 0.01 .$$

Of course, this is *not* a proof since the scale analysis ignores the specific nature of the first and second order derivatives, which we cannot know with certainty without solving the full non-linear equation. This exercise does, however, give us some confidence in the assumption. Final verification of the assumption will rely on laboratory and field tests of the experimental technique described Chapters IV, V, and VI.

We are therefore left with the task of finding a solution for the three dimensional diffusion equation:

$$\frac{\partial P}{\partial t} = D_p \nabla^2 P \,, \tag{10}$$

where the effective diffusion constant is

$$D_p = \frac{kP_a}{\varepsilon\mu} \,. \tag{11}$$

In modeling the experimental system we consider a spherical pressure source with its center at the origin. The sinusoidal source signal is at radial distance r = b. This is the effective spherical radius of the probe (discussed in more detail below).

We begin the analysis by considering the case of a source buried in an *infinite* homogeneous medium. Since the system under consideration is spherically symmetric, we can consider the disturbance pressure P to be a function of r and t alone. The initial and boundary conditions for Eq. 10 are:

(12.a) $P(r,0) = 0$ for $r \geq b$
(12.b) $P(b,t) = P_O \sin(\omega t)$ for $t > 0$
(12.c) $P(r \to \infty, t) = 0$ for $t > 0$.

Because of the spherical symmetry of the problem we might be tempted to solve Eq. 10 using spherical coordinates:

$$\frac{\partial P}{\partial t} = D_p \frac{1}{r^2} \frac{\partial}{\partial r}\left(r^2 \frac{\partial P}{\partial r} \right) \,. \tag{13}$$

However, the transformation from ([18], Chapter 9)

$$W(r,t) = r\,P(r,t) \tag{14}$$

yields a simpler one-dimensional partial differential equation:

$$\frac{\partial W}{\partial t} = D_p \frac{\partial^2 W}{\partial r^2} \tag{15}$$

that is solved readily analytically. The transformed initial and boundary conditions are

(16.a) $W(r,0) = 0$ for $r \geq b$
(16.b) $W(b,t) = b\,P_O \sin(\omega t)$ for $t > 0$
(16.c) $W(\infty,t) = 0$. for $t > 0$.

Following the example of Fukuda [17], we assume a complex solution of the form

$$\overline{W}(r,t) = \phi(r)e^{i\omega t} \quad , \tag{17}$$

where the bar on W indicates that we are considering a complex function, the real part of which will be the solution to Eq. 15, having the real boundary conditions given in Eqs. 16.a and b.

This approach will allow us to find the steady part of the solution (that is after the transient in-growth from the initial condition of W(r,0) = 0). This solution will satisfy the boundary conditions (Eqs. 16.b and 16.c) but not the initial condition (Eq. 16.a). This is sufficient since we are interested in finding the steady phase shift between the source and detector signals. Indeed, the Fourier analysis of the data, discussed below, only identifies the steady phase shift. The full transient solution is discussed later.

Substituting Eq. 17 into Eq. 15, we get an ordinary differential equation for ϕ:

$$\frac{d^2\phi}{dr^2} - \frac{i\omega}{D_p}\phi = 0 \tag{18}$$

that has the general solution

$$\phi(r) = \alpha_1 e^{\frac{\lambda(r-b)}{\sqrt{2}}(1+i)} + \alpha_2 e^{-\frac{\lambda(r-b)}{\sqrt{2}}(1+i)} \quad , \tag{19}$$

where $\lambda = \sqrt{\frac{\omega}{D_p}}$ and $i = \sqrt{-1}$.

The general solution for W(r,t) is, therefore,

$$(20) \qquad \overline{W}(r,t) = \alpha_1 e^{i\omega t} e^{\frac{\lambda(r-b)}{\sqrt{2}}(1+i)} + \alpha_2 e^{i\omega t} e^{-\frac{\lambda(r-b)}{\sqrt{2}}(1+i)} .$$

Since W is bounded at $r \to \infty$, we know that $\alpha_1 = 0$. Eq. 16.b tells us that $\alpha_2 = -bP_o i$.[3] Our solution is the real part of $\overline{W}(r,t)$

$$(21) \qquad \mathrm{Re}[\overline{W}(r,t)] = bP_o e^{-\frac{\lambda(r-b)}{\sqrt{2}}} \sin\left(\omega t - \frac{\lambda(r-b)}{\sqrt{2}}\right) .$$

Since Eq. 21 satisfies the governing equation (Eq. 15) and the boundary conditions, we know that we have obtained the correct solution.

Applying Eq. 14 to Eq. 21, we obtain the steady solution for 3-dimensional problem in the infinite medium (Eq. 10)

$$(22) \qquad P(r,t) = bP_o \frac{e^{-\frac{\lambda(r-b)}{\sqrt{2}}}}{r} \sin\left(\omega t - \frac{\lambda(r-b)}{\sqrt{2}}\right) .$$

There is one remaining complication, we must still satisfy the boundary condition that P = 0 at the soil surface. This is achieved using the standard *method of images* often used to handle boundary conditions in electrostatics problems [19]. In brief, if the real source is buried at a depth L below the surface, an imaginary 'image' source is placed at a height L above the surface, opposite the real source. The image source has a signal of equal amplitude and opposite sign to the real source, thereby canceling the effect of the real source at every point on the surface and creating the zero pressure boundary condition.

Figure 1 shows the geometry for the real and image sources and two possible probe locations. The distances between the real and image sources and

---

[3] What we are doing here is finding the complex form of W(b,t), designated $\overline{W}(b,t)$, such that its real part is equal to $bP_o e^{i\omega t}$, which is true if $\overline{W}(b,t) = -ibP_o e^{i\omega t}$. This is then set equal to the right hand side of Eq. 20 with r = b and $\alpha_1 = 0$.

the detector probe are r and r', respectively. The response location is given by the sum of the effects of the real and im equivalent infinite media). The effect of the image source at the is:

$$P_I(r',t) = -bP_o \frac{e^{-\frac{\lambda(r'-b)}{\sqrt{2}}}}{r'} \sin\left(\omega t - \frac{\lambda(r'-b)}{\sqrt{2}}\right). \tag{23}$$

The full solution at the detector location for a given val given by the sum of Eqs. 19 and 20:

$$P_{det}(t) = P(r,t) + P_I(r',t) \ . \tag{24}$$

For convenience in analyzing the measurement data we would expression for Eq. 20 of the form:

$$P_{det}(t) = \gamma b P_o \sin(\omega t - \beta) \ . \tag{25}$$

This objective can be achieved by making the following substitu

$$A_1 = \frac{e^{-\frac{\lambda(r-b)}{\sqrt{2}}}}{r} \tag{26.a}$$

$$A_2 = \frac{e^{-\frac{\lambda(r'-b)}{\sqrt{2}}}}{r'} \tag{26.b}$$

$$\delta_1 = \frac{\lambda(r-b)}{\sqrt{2}} \tag{26.c}$$

$$\delta_2 = \frac{\lambda(r'-b)}{\sqrt{2}} \ . \tag{26.d}$$

Eq. 24 can then be written:

$$P_{det}(t) = bP_o\left\{A_1 \sin(\omega t - \delta_1) - A_2 \sin(\omega t - \delta_2)\right\} \tag{27}$$

Using the trigonometric identity

(28) $$\sin(x\text{-}y) = \sin(x)\cos(y)\text{-}\cos(x)\sin(y)$$

Eq. 27 is rewritten

(29)
$$P_{det}(t) = bP_o\left\{\sin(\omega t)\left[A_1\cos(\delta_1) - A_2\cos(\delta_2)\right] - \cos(\omega t)\left[A_1\sin(\delta_1) - A_2\sin(\delta_2)\right]\right\}.$$

We now define the variables α and γ, such that they satisfy the following equations:

(30.a) $$\gamma\cos(\beta) = \left[A_1\cos(\delta_1) - A_2\cos(\delta_2)\right]$$
(30.b) $$\gamma\sin(\beta) = \left[A_1\sin(\delta_1) - A_2\sin(\delta_2)\right]\ .$$

Eq. 29 is then simplified to

(31) $$P_{det}(t) = \gamma bP_o\sin(\omega t - \beta)$$

as desired.

The phase shift at the detector location, β, is calculated using Eqs. 30.a and 27.b.

(32) $$\beta = \tan^{-1}\left(\frac{A_1\sin(\delta_1) - A_2\sin(\delta_2)}{A_1\cos(\delta_1) - A_2\cos(\delta_2)}\right)$$

Given particular D_p and ω, the time lag, T, for the signal to travel from the source to the detector location is simply $\frac{\beta}{\omega}$, or

(33) $$\boxed{T = \frac{1}{\omega}\tan^{-1}\left(\frac{\frac{e^{-\frac{\lambda(r-b)}{\sqrt{2}}}}{r}\sin\left(\frac{\lambda(r-b)}{\sqrt{2}}\right) - \frac{e^{-\frac{\lambda(r'-b)}{\sqrt{2}}}}{r'}\sin\left(\frac{\lambda(r'-b)}{\sqrt{2}}\right)}{\frac{e^{-\frac{\lambda(r-b)}{\sqrt{2}}}}{r}\cos\left(\frac{\lambda(r-b)}{\sqrt{2}}\right) - \frac{e^{-\frac{\lambda(r'-b)}{\sqrt{2}}}}{r'}\cos\left(\frac{\lambda(r'-b)}{\sqrt{2}}\right)}\right)}$$

From Eq. 31, we also see that the signal amplitude at the detector location is

$$(34) \qquad bP_o\gamma = bP_o \frac{A_1\cos(\delta_1) - A_2\cos(\delta_2)}{\cos(\beta)} \ .$$

Note that care must be exercised in interpreting the solution in this form since half cycles of phase lags are indicated by changing the sign of the amplitude term, and time lags separated by integer numbers of full cycles are indistinguishable. Therefore, in practice, we begin by computing T for very high permeabilities for which we know that the phase lags are less than one cycle and then decrease the permeability incrementally. Since we know that time lag must increase monotonically with decreasing permeability, the solutions can be correctly interpreted with little difficulty.

An alternative approach for determining the correct integer (or half integer multiple) of the driving period is to generate the full solution of the dynamic pressure problem that includes the term for transient in-growth of the pressure signal. Comparing this with the source signal gives an unambiguous result, but the analysis is considerably more time consuming.

The complete solution to Eq. 10, including the transient in-growth, is obtained using Green's functions to solve Eq. 15. The procedure is detailed in the appendix to this chapter. As before, the full solution is given by the sum of the contributions of the real and imaginary sources:

$$(35) \qquad P(r,t) = \frac{1}{r}\int_0^t bP_a \sin(\omega\tau)\frac{(r-b)}{(t-\tau)}\frac{e^{-\frac{(r-b)^2}{4D_p(t-\tau)}}}{\sqrt{4\pi D_p(t-\tau)}}d\tau .$$

$$(36) \qquad P_I(r',t) = -\frac{1}{r'}\int_0^t bP_a \sin(\omega\tau)\frac{(r'-b)}{(t-\tau)}\frac{e^{-\frac{(r'-b)^2}{4D_p(t-\tau)}}}{\sqrt{4\pi D_p(t-\tau)}}d\tau \ .$$

To check our model, the Green's function solution was compared to the analytical solution, and their steady parts were found to agree exactly. The Green's function solution was used to determine the time required to reach a steady signal, $\sim\sqrt{r^2 / D_p}$ (the time for the system to respond to a step function change in pressure at the source location). For our experimental system this is ~10 s. This presents no problem for our measurements since we gather data over many signal periods, ~30 minutes, and the data analysis technique is insensitive to the transient part.

The advantage of using the analytical solution over the Green's function approach is that a functional form can be obtained for the time lag. In the case of the Green's function solution, Eqs. 35 and 36 must first be solved numerically, the steady part of the solution must then be graphically fitted to a sinusoidal curve and compared with the source signal to find the phase lag. This procedure must be repeated point-wise to obtain a curve of permeability vs. time lag for each detector location under consideration—an extremely time intensive process.

Model Application

Figure 2 shows a sample set of theoretical curves of lag time vs. permeability for a source signal with a 60 s period imposed at 2-m depth. Each figure shows traces for a number of possible detector locations, identified by their radial distance from the source (r) and angle (θ), as in Figure 1. The following parameters are used in the calculations to correspond with conditions in the field test:

(37.a)	$P_a = 900$ Pa	Amplitude of the driving signal.
(37.b)	$2\pi/\omega = 60$ s	Period of the driving signal.
(37.c)	$P_o = 92{,}000$ Pa	Mean atmospheric pressure at experiment site.
(37.d)	$\mu = 1.8\mathrm{x}10^{-5}$ Pa s	Dynamic viscosity of air.
(37.e)	$b = 0.1$ m	Effective spherical radius of source.
(37.f)	$\varepsilon = 0.45\pm.02$	Air-filled porosity of soil.

The air-filled porosity is calculated from the absolute porosity reported in [20], and from soil moisture content measured using a time domain reflectometer device (Trase, System 1, Soilmoisture Equipment Corp., Santa Barbara, CA). The driving frequency can be optimized for specific soil conditions. Higher frequency driving signals allow measurements to be made in a shorter amount of time but produce lower amplitude signals at the detector location.

Note that the observed time lag at the detector location will depend on the driving signal frequency, as indicated by Eqs. 33 and the fact that $\lambda(\omega)$. To check our experimental design and model, we ran several experiments at fixed detector locations but different driving periods (30 s and 60 s). In each case the time lags changed as predicted by the theory, and, for each path, identical permeabilities were determined by the measurements made using the two different periods.

FIELD TEST

Experimental Design

We carried out field tests of the dual-probe dynamic pressure technique in Ben Lomond, California, at the site of the soil-gas transport experiments discussed in Chapter 2. Spot measurements of soil permeability were made at the site using both blunt-end soil probes (technique described in [21]) and probes through which sampling occurs near the end of a sealed steel pipe via a welded-in cylindrical well screen technique described in [2] and results in Chapter 2.

The source probe for this experiment was a previously installed well-screen probe, horizontally oriented and positioned 2 m below the soil surface and 5 m south of the structure. This probe was used because the well screen provides a large enough area open to the soil to propagate the pressure signal through several meters of soil without excessive signal loss due to attenuation, while maintaining soil-gas velocity well within the Darcy limit at a distance 0.01 m from the source. The effective spherical radius of the cylindrical source was determined by comparing a numerical simulation of a static pressure field around a cylindrical source with the analytical prediction of the field surrounding a spherical source. An effective spherical radius of 0.10 m was estimated for the 15-cm-long well screen. The maximum error associated with the spherical-source approximation can be determined from consideration of the real and approximated sources. The maximum distance between the surfaces of the real 0.01-m radius cylindrical source and the assumed 0.1-m spherical source is 0.04 m. For a pressure signal propagating at constant velocity along a 2-m path, this represents error in the lag time of 0.04/2, or 2%. From Figure 2, for a detector probe 2 m from the source, at an orientation of 0°, this would produce an uncertainty in permeability of only about 1%.

Seven detector probes were installed vertically from the soil surface using a procedure described previously [12]. (These are identified by the labels NE-S, E-D, SE-S, S-D, SW-S, W-D, and NW-S, on Figure 3). Each probe consisted of an open-ended length of 10-mm ID galvanized steel pipe (nominally 1/8-inch) threaded at the top for connection to 4-mm ID polyethylene tubing. The tubing carried the pressure signal to a low-range, variable reluctance pressure transducer (resolution ~ 0.2 Pa). To avoid undue disturbance of the pressure field at the probe tip due to compaction of soil during probe installation, the soil at the bottom of each blunt-end probe was loosened using a wood auger welded to the end of a long rod.

Figure 3 shows the spatial distribution of the source and detector probes. Each of the seven newly installed detector probes terminated at a radial distance of 2 m from the source. Three of the probes sampled from the same depth as the source probe ($r = 2$ m, $\theta = 0^{o}$, Figure 1), the other three sampled the near-surface soil ($r = 2$ m, $\theta = 45^{o}$, Figure 1). In addition, two previously installed and horizontally positioned well-screen-type probes (N-D and N-M, on Figure 3) were also used for signal detection, one with r=2.69 m and $\theta = 0^{o}$, the other with $r = 3.12$ m and $\theta = 30^{o}$.[4]

The source signal was created using two mass flow controllers coupled as shown in Figure 4. To create a sinusoidally oscillating pressure signal centered about the mean atmospheric pressure, one mass flow controller was driven to produce a sinusoidal flow with a positive DC offset ($Q = B + A \sin(\omega t)$, $B \geq A$), while the other maintained a constant negative offset of the same amplitude ($Q = -B$). The flows were adjusted at the site to produce a source pressure amplitude, A, of about 900 Pa.

Before the start of each experiment the sinusoidally oscillating source flow was vented to the atmosphere. The source probe was also open to the atmosphere to ensure neutral pressure. While recording the pressure signal at the source and detector probes, at $t = 0$, the source signal was switched to the source probe. Data were collected for about 20 minutes. We found that it was sufficient to gather about 20 driving-frequency cycles to get a good signal to noise ratio. For the soil we investigated, driving periods between 30 and 60 s were optimal. For low permeability soils, however, one might want to use a lower driving frequency to increase the amplitude of the detected signal, and to integrate longer to reduce the effect of noise. Laboratory tests ensured that

---

[4] These probes and the source probe were installed as part of the measurement system for determining radon and soil-gas transport into the Ben Lomond experimental basement (west structure).

phase shift and amplitude attenuation of the signal across the length of tubing and probe was negligible. These same tests demonstrated that there were no problems due to potentially different response times of the source and detector pressure transducers.

Data Analysis

The source and detector signals were decomposed into their frequency components by Fast Fourier Transform (FFT) using commercially available software (MathCad, MathSoft Inc., Cambridge, MA) running on an IBM PC clone with 2 Mb RAM. A peak at the driving frequency was clearly visible in all of our detector signals. The phase information from the FFT was then used to determine the lag time between the source and detector signals. In our case, visual inspection of the raw data was sufficient to ascertain that the first peak arrived at the detector within the first source signal period rather than during some later period, in which case the actual lag time would be some integral multiple of the period plus the lag determined by the transform.

A combination of two factors, numerical dispersion and environmental noise, makes it advantageous to use lag time rather than amplitude attenuation of the source signal as the indicator of permeability. Numerical execution of the FFT on even a pure, single-frequency, sinusoidal data train of finite length shows that there can be considerable dispersion of the signal into adjacent frequency bands. When environmental noise is added to the detected signal, it becomes impossible to determine how much of the power in adjacent bands actually belongs to the driving signal and how much results from real noise. Therefore, the detected pressure amplitude at the driving frequency has larger uncertainty.

The lag time, on the other hand, is determined by comparison of the source and detector signals at the driving frequency alone, and the resolution of the signal is determined only by the number of data points collected and the sampling frequency. Furthermore, lag times give better resolution at large distances from the source because the propagation velocity falls off less rapidly with distance from the source than does the signal amplitude.

RESULTS

The results of the probe-to-probe dynamic permeability measurements are displayed in square brackets in Figure 3 for each source-to-detector path. The permeabilities measured at each of the probes using the static technique are shown in parentheses. Table I lists the permeabilities and indicates the ratio of the dynamic result for each path to the average of the static measurements at its end points. The uncertainty in the results of the dynamic pressure measurements are determined from the estimated uncertainty in the measurement of air-filled porosity and the uncertainty in the measured lag time.

Two features stand out: (1) The dynamic measurements consistently give a higher estimate of permeability than the static measurements, by a factor of six, on average. This suggests that permeability is scale-dependent, with effective permeability increasing as the sampling scale increases. The results of the measurements on the N-D and N-M probes support this finding—these are the most distant probes and they have the highest observed permeabilities. (2) The dynamic measurements also yield consistently higher permeabilities for the horizontal direction than for the nonhorizontal directions indicating the presence of anisotropy. As expected, the dynamic results are considerably less variable than the static results because sampling occurs over a longer integration path, minimizing the detection of small-scale heterogeneity.

A first order approximation of vertical-horizontal anisotropy can be made using the hydrogeological concept of a hydraulic-conductivity ellipse ([22], p. 174) and given values for horizontal permeability measurements (k_h) and those made at a 45° orientation (k_{45}). The vertical permeability, k_v, is then estimated from:

$$\frac{x^2}{k_h} + \frac{z^2}{k_v} = 1 \quad (38)$$

The measurement made at $\theta = 45°$ gives us the location of a point on the ellipse at:

$$x = z = \sqrt{k_{45}}\cos(45^\circ) \quad (39)$$

From the data in Table I (for $r = 2.0$ and $\theta = 0$), k_h is 23×10^{-12} m^2. The average permeability along $\theta = 45°$ (k_{45}) is 17×10^{-12} m^2. Using these values, and substituting Eq. 39 into Eq. 38, k_v is estimated to be 13.5×10^{-12} m^2, ~0.6 times the horizontal value.

DISCUSSION

Dynamic measurements of soil permeability to air have been made previously [9, 14, 15]. These measurements used fluctuations in barometric pressure as the source signal and were confined to assessments of vertical permeabilities. Dependence upon the vicissitudes of the barometric pressure signal limits the range of soil conditions and physical scales over which measurements can be made using this one-dimensional technique, and complicates data analysis, creating large uncertainties in estimates of permeability [15].

In contrast, the use of a controlled sinusoidal source signal in the current technique enables precise, phase-sensitive detection with low uncertainty. Signal amplitude and period can be adjusted for detection over longer paths or in lower permeability soil. In cases of high environmental noise, signals can be integrated over arbitrarily long times, limited only by the size of RAM in the computer doing the FFT. This is not a serious limitation with the current availability of inexpensive computing power.

A drawback of the dynamic pressure technique relative to the static techniques is that it requires knowledge of the effective flow porosity under the experimental conditions, since what is being measured directly is the pressure diffusivity, $D_p = kP_a/\varepsilon\mu$, rather than k. Effective flow porosity is the air-filled porosity through which flow actually occurs. In other words, if all flow is occurring through fast paths that occupy only 2% of the soil volume and have an intrinsic porosity of 50%, then the effective flow porosity would be only 1%, rather than the usual values of bulk porosity of ~30 – 40%. (*I.e.*, effective flow porosity = volume of pore space in fast paths / volume of soil.)

The problem that arises is that effective flow porosity might itself depend upon both scale and source signal frequency. The extent to which porosity in the low permeability part of the soil is excluded from contributing to the effective porosity is determined approximately by the spacing between and interconnectedness of the fast paths dominating flow and by the frequency of the source signal. If the pressure signal has time to diffuse through the low-k part, then its porosity is included. That is, if the low permeability part has dimension $< \sim \sqrt{D_p \Delta t}$ (the diffusion length of the signal) then it is included. D_p is taken here as the pressure diffusivity of the low-k part of the soil given the porosity of that part of the soil and Δt is taken as the half-period of the source signal.

Fortunately there are ways to test if experiments are being carried out in a regime in which effective flow porosity is scale dependent. In addition, if that is found to be a problem, the source signal frequency can be reduced, increasing time for the dynamic signal to permeate the low permeability soil. The only negative impact of this is increasing the time over which experiments must be run. These issues are discussed further in Chapter V.

One of the desirable features of this measurement technique is that the results do <u>not</u> contain the $1/r$ weighting factor inherent in small-source static techniques. The difference derives from our use of wave-front propagation time as the parameter to determine permeability. In an infinite homogeneous and isotropic medium, the propagation velocity is constant, independent of distance from the source. To the extent that this is true for our semi-infinite medium, we obtain unweighted results from our dual-probe technique, with each point along the path contributing equally to the characterization.

To explore the effect of the semi-infinite medium on the weighting factor, we plot the time lag of the source-to-detector signal (Eq. 33) vs. radial distance from the source as the signal propagates in the vertical and horizontal directions. Figures 5a and 5b show the results for two different soils with homogeneous permeabilities of 8.5×10^{-13} m^2 and 8.5×10^{-12} m^2, respectively. When the points on the graph lie along straight lines the propagation velocity of the pressure wave is constant along the path, an indication that each point along the soil path contributes equally to the total lag time (*i.e.,* the weighting factor is constant along the path). For the vertical path of Figure 5b, the weighting factor decreases with proximity to the soil surface. This result occurs because the wave front velocity increases as it approaches the surface, decreasing the relative contribution of this part of the path to the total measured lag time.

The ideal for determining effective permeabilities over long paths is to have the weighting factor remain constant. In order to compare the effective weighting functions of the static measurement techniques with the vertical and horizontal measurements of the dynamic technique, we have plotted in Figure 6 the normalized weighting factors for the three measurements for the configuration indicated in Figure 5 (bottom). The traces are normalized such that the weighting equals one at the surface of the pressure source (r=0.1 m). The weighting factors for the dynamic measurements are simply the slopes of the traces in Figure 5 (bottom). The weighting factor for the static case is proportional to 1/r. Even for the vertical path, the weighting factor for the dynamic measurement does not fall off nearly as sharply moving away from the probe as it does for the static measurement.

The apparent existence of scale dependence of soil permeability evident from the field tests of the dynamic technique is important. If this effect is verified by future tests in other soils, it means that the typical method of characterizing soil by multiple small-scale measurements can produce misleading results. A study by Schery and Siegel of natural soil in Socorro, New Mexico [23], supports our finding of increasing permeability with scale. In one-dimensional tests of vertical permeability they found a factor of 20 increase in permeability as the integration path increased from a few centimeters to about one meter. The authors showed evidence that increasing permeability with increasing scale resulted from the higher probability of intercepting spatially infrequent, high-flow paths at larger scales.

The ability to make not only larger scale measurements, but also measurements at different scales with one technique, is clearly an advantage of this new method in studying the transport characteristics of soils if scale dependence is typical—an issue that can be resolved by investigations in different soils using the dynamic technique. This feature, along with the ability to detect anisotropy, makes the technique attractive despite its drawback of being considerably more equipment intensive than the static methods.

Examination of the theory for estimating permeabilities from the static method elucidates an additional advantage in the present technique. Permeability is estimated from static measurements using an equation of the form:

$$k = \frac{Q\mu}{S\Delta P} \tag{40}$$

where Q is the steady flow imposed into or out of the probe, ΔP is the disturbance pressure difference between the surface and the sampling region of the probe (i.e., the total pressure difference minus the hydrostatic component), and S is a 'shape factor' that depends on the geometry of the probe. In the case of a buried cylinder, there is more than a factor of two range in published estimates of the shape factor (compare [24] and [25]). In addition, one source

[25] shows a factor of 2 change in shape factor with probe depth, going from 0.15 m to 1.81 m, while another is [24] is relatively insensitive to depth, giving only a 10% change in shape factor over the same depths. Our numerical estimates of the shape factor, used for the analysis of the static measurements given here, give a midrange value that is relatively insensitive to depth [2] Data analysis for the probe-to-probe dynamic pressure technique does not require the use of a shape factor and therefore reduces the associated uncertainty.

An issue was raised in the theory section about the extent of the problem that is created by interpreting experimental data for heterogeneous or anisotropic soils using a homogeneous, isotropic model. All measurements of soil permeability rely on models for interpretation of experimental data. As with any other technique, the extent to which actual soils violate the model assumptions determines the accuracy of the technique. In this regard the current experimental technique does, however, improve on most previous techniques in two ways. First, the dynamic technique provides valuable information about relative permeabilities in specific directions since the end points of the path are well defined. This is not true of any single-probe technique in which the dominant information will come from the path of least resistance; but there is no way of determining where that path lies. Second, the existence of systematic heterogeneity or anisotropy is immediately evident from an array of measurements. If more detailed information on the soil is required, one can improve on the solution by iterating a numerical model incorporating the guessed anisotropy or heterogeneity against the experimental results. The iterative procedure is likely to be extremely time intensive, however, and requires the availability of a model that can simulate anisotropy and layering and the time dependent boundary conditions described in the theory section.

CONCLUSIONS

The dual-probe dynamic pressure technique has definite advantages over previous static techniques for measuring soil permeability to air. First, effective permeabilities can be measured over variable length scales up to and including that over which houses tend to interact with the soil. Second, the presence of anisotropy of permeability is easily detected, although an exact measure is not obtained without detailed analysis using a more sophisticated numerical model.

A drawback of the dynamic technique is that it is not a direct measurement of permeability, k, but of the pressure diffusivity, $kP_a/\varepsilon\mu$. Therefore, the effective porosity, ε, must be known. In addition, the dynamic technique is more instrument intensive than the simpler static techniques.

Field tests comparing the results of static and dynamic measurements appear to indicate scale-dependence of soil permeability to air. The dynamic results yield consistently higher permeabilities, with considerably less spatial heterogeneity, than the static measurements—on average by a factor of about six. The finding of scale-dependent permeability is further supported by the fact that the highest permeabilities of the dynamic measurements occurred in the two measurements with the longest paths. The finding of scale-dependent permeability, which is validated by further experiments in Chapters V and VI, has important implications for site assessment and modeling of the transport of radon and other gas-phase contaminants through soil. The most obvious implication is that the typical method of assessing the transport potential, based on multiple small scale measurements, can produce seriously misleading results in systems that operate naturally at larger scales.

The probe-to-probe technique also offers several advantages over the previously used dynamic pressure technique that relies on barometric pressure fluctuations for the source signal [17, 23]: Our measurement is not confined to the vertical direction, but can be made along any arbitrary path from the source, allowing the detection of anisotropy of soil permeability. The use of the controlled source signal enables integration of the detected signal over arbitrary long times greatly increasing the signal to noise ratio. The single-frequency source signal also allows frequency-sensitive detection, which limits the uncertainty in the propagation time (the indicator of permeability) to the frequency band width of the Fast Fourier Transform. The band width of the frequency channels are in turn determined by the data sampling frequency and experiment duration—both controllable parameters. In addition, manipulation of the source signal permits measurements over longer path lengths and under a wider range of soil conditions than the previous dynamic technique.

REFERENCES

1. Fisk, W.J., Flexser, S., Gadgil, A.J., Holman, H.Y., Modera, M.P., Narasimhan, T.N., Nuzum, T., Revzan, K.L., Sextro, R.G., Smith, A.R., Tsang, Y.W. and Wollenberg, H.A., *Monitoring and Modeling for Radon Entry into Basements: A Status Report for the Small Structures Project.* LBL-27692, Lawrence Berkeley Laboratory: Berkeley, CA: 1989.

2. Fisk, W.J., Modera, M.P., Sextro, R.G., Garbesi, K., Wollenberg, H.A., Narasimhan, T.N., Nuzum, T. and Tsang, Y.W., *Radon Entry into Basements: Approach, Experimental Structures, and Instrumentation of the Small Structures Project.* LBL-31864, Lawrence Berkeley Laboratory: Berkeley, CA: 1992.

3. Nazaroff, W.W., Lewis, S.R., Doyle, S.M., Moed, B.A. and Nero, A.V., Experiments on pollutant transport from soil into residential basements by pressure-driven airflow, *Environmental Science and Technology,* 1987, 21: 459-466.

4. Nazaroff, W.W., Entry by pressure-driven flow or molecular diffusion? A reassessment of ^{222}Rn concentrations measured in an energy efficient house, *Health Physics,* 1988, 55: 1005-1009.

5. Nazaroff, W.W., Boegel, M.L. and Nero, A.V., Measuring radon source magnitude in residential buildings. In: *Proceedings of the International Meeting on Radon-Radon Progeny Measurements..* EPA 520/5-83/021, US Environmental Protection Agency, Washington, DC, 1981.

6. Nero, A.V. and Nazaroff, W.W., Characterizing the source of radon indoors, *Radiation Protection and Dosimetry,* 1984, 7: 23-39.

7. Nazaroff, W.W., Feustel, H., Nero, A.V., Revzan, K.L., Grimsrud, D.T., Essling, M.A. and Toohey, R.E., Radon transport into a detached one-story house with a basement, *Atmospheric Environment,* 1985, 19: 31-43.

8. Bruno, R.C., Sources of indoor radon in houses: A review, *Journal of the Air Pollution Control Association*, 1983, 33: 105-109.

9. Åkerblom, G., Anderson, P. and Clavensjo, B., Soil gas radon—A source of indoor radon daughters, *Radiation Protection Dosimetry*, 1984, 7: 49-54.

10. Scott, A.G., *Computer modeling of radon movement.* In: EML Indoor Radon Workshop, 1982. Report EML-416, Environmental Measurements Laboratory, New York: 1983.

11. Sextro, R.G., Moed, B.A., Nazaroff, W.W., Revzan, K.L. and Nero, A.V., Investigations of soil as a source of indoor radon. In: *Radon and Its Decay Products: Occurrences, Properties, and Health Effects,* Hopke, P. K., Ed. American Chemical Society: Washington, DC, 1987, 10-29.

12. Turk, B.H., Prill, R.J., Grimsrud, D.R., Moed, B.A. and Sextro, R.G., Characterizing the occurrence, sources and variability of radon in Pacific Northwest homes, *Journal of the Air and Waste Management Association,* 1990, 40: 498-506.

13. Garbesi, K. and Sextro, R.G., Modeling and field evidence of pressure-driven entry of soil gas into a house through permeable below-grade walls, *Environmental Science and Technology*, 1989, 23: 1481-1487.

14. Hodgson, A.T., Garbesi, K., Sextro, R.G. and Daisey, J.M., Soil-gas contamination and entry of volatile organic compounds into a house near a landfill., *Journal of the Air and Waste Management Association,* 1992, 42: 277-283.

15. Garbesi, K., Sextro, R.G., Fisk, W.J., Modera, M.P. and Revzan, K.L., Soil-gas entry into an experimental basement: Model-measurement comparisons and seasonal effects, *Environmental Science and Technology,* 1993, 27: 466-473.

16. Tanner, A.B., Methods of Characterization of Ground for Assessment of Indoor Radon Potential at a Site. In: *Field Studies of Radon in Rocks, Soils,*

and Water. Gundersen, L. C., and R.B.Wanty. U.S. Geological Survey Bulletin, 1991.

17. Fukuda, H., Air and vapor movement in soil due to wind gustiness, *Soil Science,* 1955, 4: 249-256.

18. Carslaw, H.S. and Jaeger, J.C., *Conduction of Heat in Solids,* 2nd Ed., Clarendon Press: Oxford, 1959.

19. Reitz, J.R., Milford, F.J. and Christy, R.W., *Foundations of Electromagnetic Theory,* Addison-Wesley: Reading, Massachusetts, 1979.

20. Brimhall, G.H. and Lewis, C.J., *Differential Element Transport in the Soil Profile at the Ben Lomond Small Structure Radon Site: A Geochemical Mass Balance Study.* Department of Geology and Geophysics, University of California, Berkeley: 1992.

21. Garbesi, K., *Experiments and Modeling of the Soil-Gas Transport of Volatile Organic Compounds into a Residential Basement.* LBL-25519 Rev., Lawrence Berkeley Laboratory: 1988.

22. Freeze, R.A. and Cherry, J.A., *Groundwater,* Prentice-Hall, Inc.: Englewood Cliffs, New Jersey, 1979.

23. Schery, S.D. and Siegel, D., The role of channels in the transport of radon from the soil, *Journal of Geophysical Research,* 1986, 91: 12366-12374.

24. Hahne, E. and Grigull, U., Formfaktor und formwiderstand der stationaren mehrdimensionalen warmeleitung, *Journal of Heat and Mass Transfer,* 1975, 18: 751-767.

25. Holman, J.P., *Heat Transfer,* McGraw Hill: New York, 1976.

Table I. Permeabilities (k) determined at individual probes using static techniques and between the reference and detector probes using the dual-probe dynamic technique.

Probe ID[a]	r and θ as in Figure 1	Static Detector Probe k $(10^{-12}\ m^2)$[b]	Static Source Probe k $(10^{-12}\ m^2)$	Avg. of static k at end points[c] $(10^{-12}\ m^2)$	Dynamic k of path[d] $(10^{-12}\ m^2)$	Ratio of dynamic to avg. static	Dynamic Regional Avg. k $(10^{-12}\ m^2)$
SE-S	2.0 m, 45°	1.6 ±0.1	5.9 ± 0.4	3.8	17±1.3	4.5	
SW-S	2.0 m, 45°	4.9 ±0.4	5.9 ± 0.4	5.4	15±1.3	2.8	
NW-S	2.0 m, 45°	1.6 ±0.1	5.9 ± 0.4	3.8	18±1.4	4.7	17
N-M[d]	3.1 m, 30°	9.8 ±0.7	5.9 ± 0.4	7.9	35±2.0	4.4	35
E-D	2.0 m, 0°	0.53 ± 0.04	5.9 ± 0.4	3.3	25±1.6	7.6	
S-D	2.0 m, 0°	0.29 ± 0.02	5.9 ± 0.4	3.1	23±1.5	7.4	
W-D	2.0 m, 0°	0.82 ± 0.06	5.9 ± 0.4	3.4	22±1.5	6.5	23
N-D[d]	2.6 m 0°	3.6 ±0.2	5.9 ± 0.4	4.8	29±1.8	6.0	29

[a] The part of the probe ID coming before the dash is the compass direction from the source probe location, SE=southeast, etc., the part coming after the dash is the depth, S=shallow (0.6 m), M=mid-level (1 m), D=deep (2 m). The source probe is at the D level.

[b] Uncertainties, calculated assuming shape factor is certain, are based on environmental noise in measurements, which exceeds uncertainty due to propagation of instrumental errors.

[c] Average of the static measurements of permeabilities at the source and detector probes.

[d] Estimated permeability of the path between the source and detector probes determined from the dynamic pressure technique. Uncertainties derived from uncertainty in measurement of air-filled porosity of soil and uncertainty in time lag.

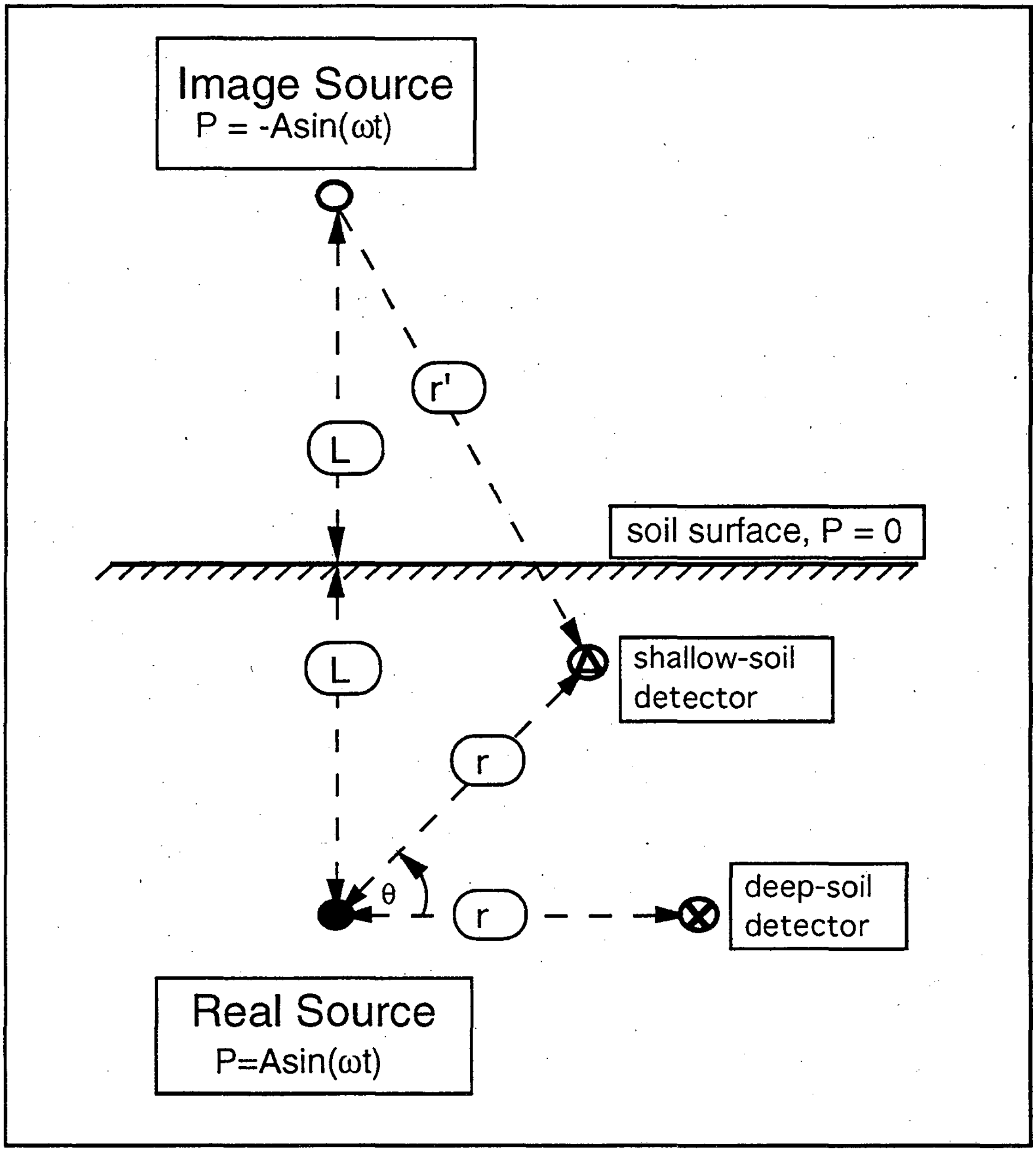

Figure 1. Geometry for the real and image sources for the model of the dual-probe dynamic pressure measurements of soil permeability to air. The figure shows two possible detector probe locations. L is the depth to the real source probe, r is the distance from the real source to a given detector probe, and r' is the distance from the image source to a given detector probe. In this figure the two detector probes are the same distance from the real source probe. This configuration may be used to investigate the anisotropy of soil permeability to air.

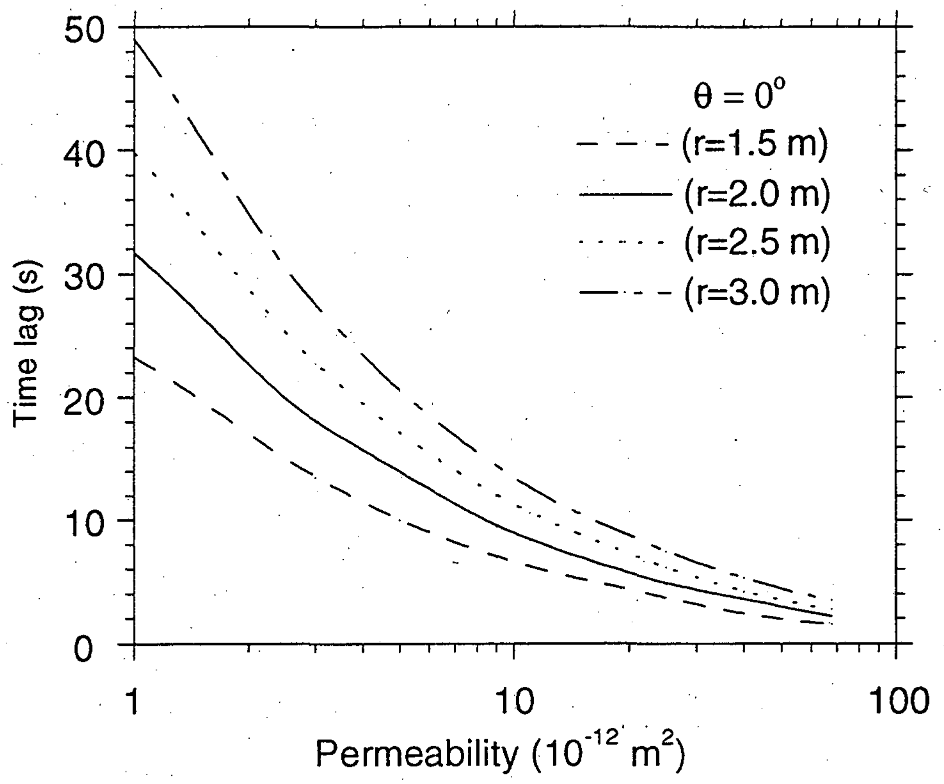

Figure 2. Sample theoretical curves of time lag vs. permeability for a source at depth (L) = 2 m. All other settings as in Eqs. 37.a - 37.f. Traces are for different possible detector locations, given by radial distance (r) and angle (θ), as in Figure 1. Curves are based on Eq. 33.

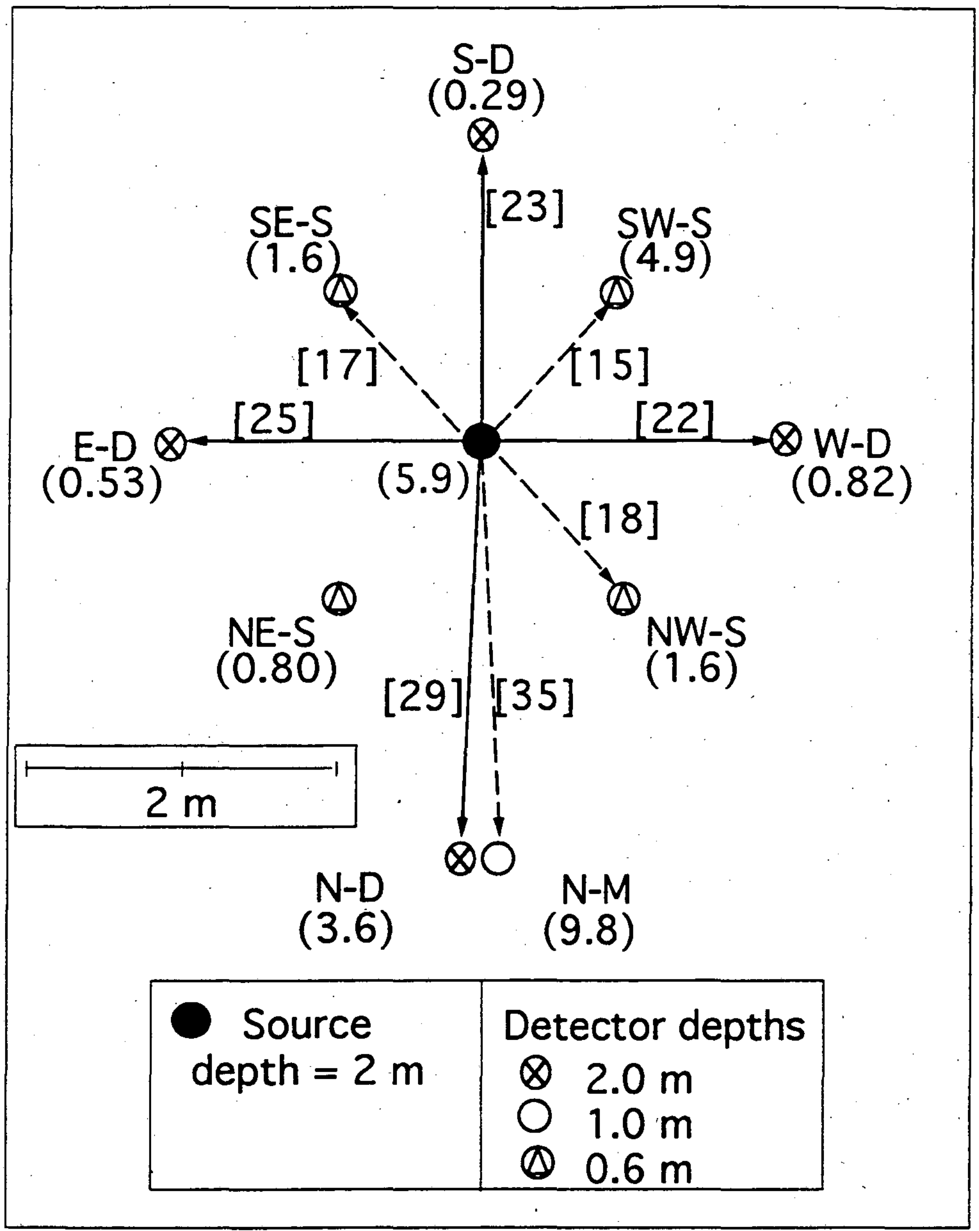

Figure 3. Locations and results of static and dynamic permeability measurements. Permeabilities (x 10^{-12} m^2) were measured at each of the detector probe using the static technique (indicated in parentheses). Permeabilities measured by the dynamic technique for the source-to-detector pathways are in square brackets. Probe IDs are as in Table I.

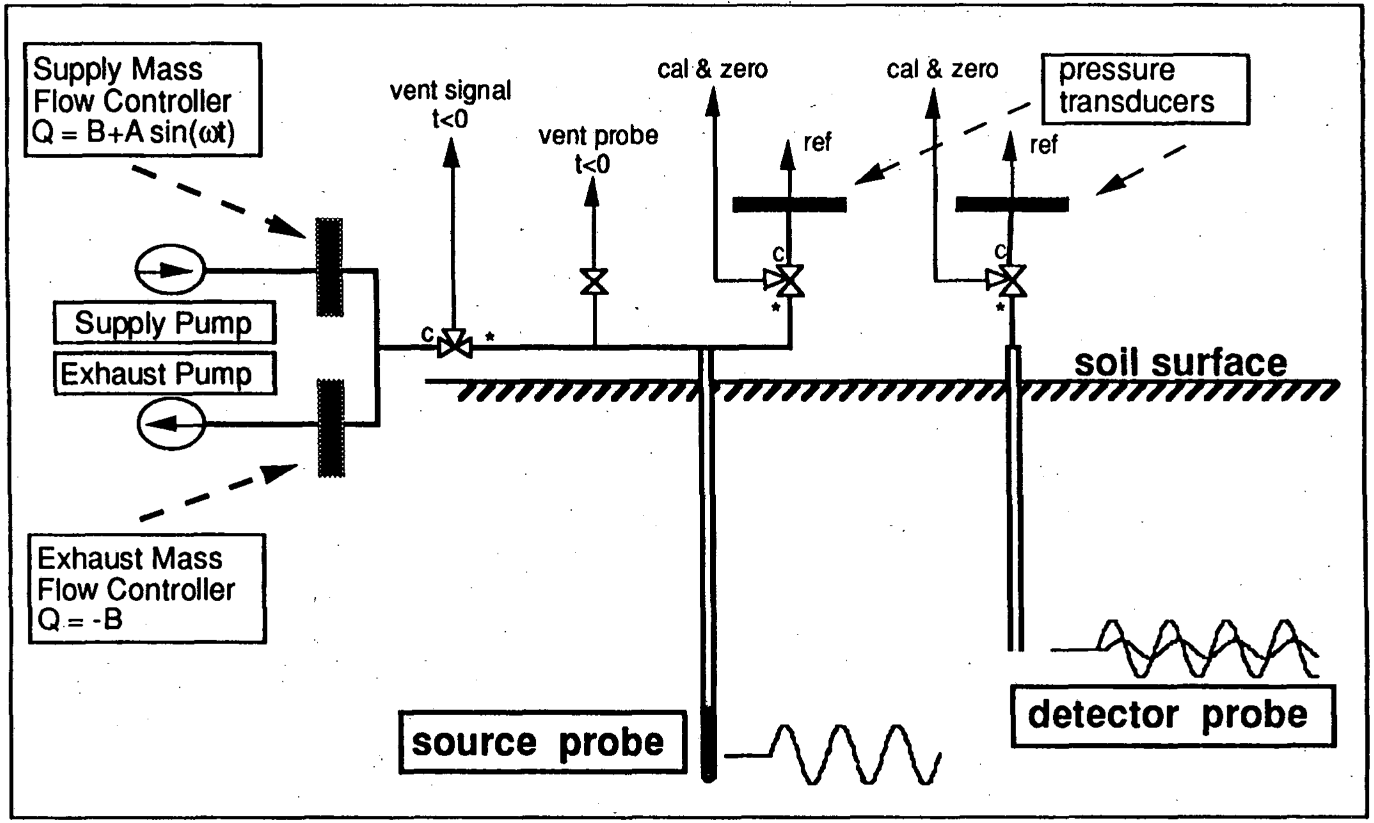

Figure 4. Schematic of apparatus for dual-probe dynamic pressure measurement of soil permeabilities. On the three-way solenoid valves, the ports are marked 'c' for common and '*' for the port that is opened at t = 0 for directing the signal to the source and detector probes. The venting solenoids are included to ensure that the source probe pressure is neutral prior to t = 0. The ports marked 'cal & zero' are for checking the calibration and zero settings on the pressure transducers.

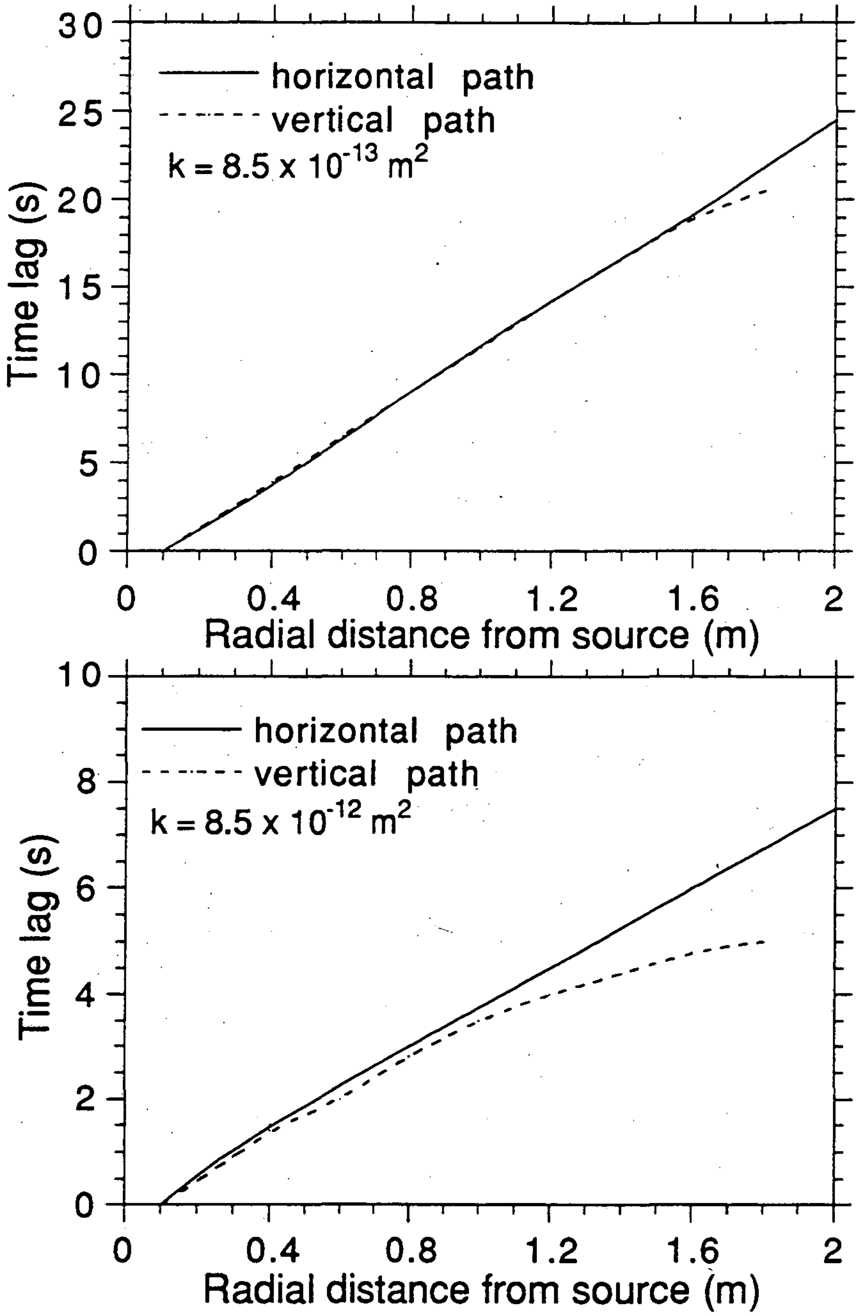

Figure 5a. (Top plot) Predicted lag time of signal vs. distance from source signal along a horizontal ray ($\theta = 0^o$, Figure 1) and a vertical ray ($\theta = 90^o$). The model was run given a soil permeability of 8.5×10^{-13} m^2 and a source depth of L = 2 m. Other paramaters as given in Eqs 37 a - f. Curves are based on Eq. 33.

Figure 5b. (Bottom plot) Same as Figure 5a, except for a soil with permeability 8.5×10^{-12} m^2.

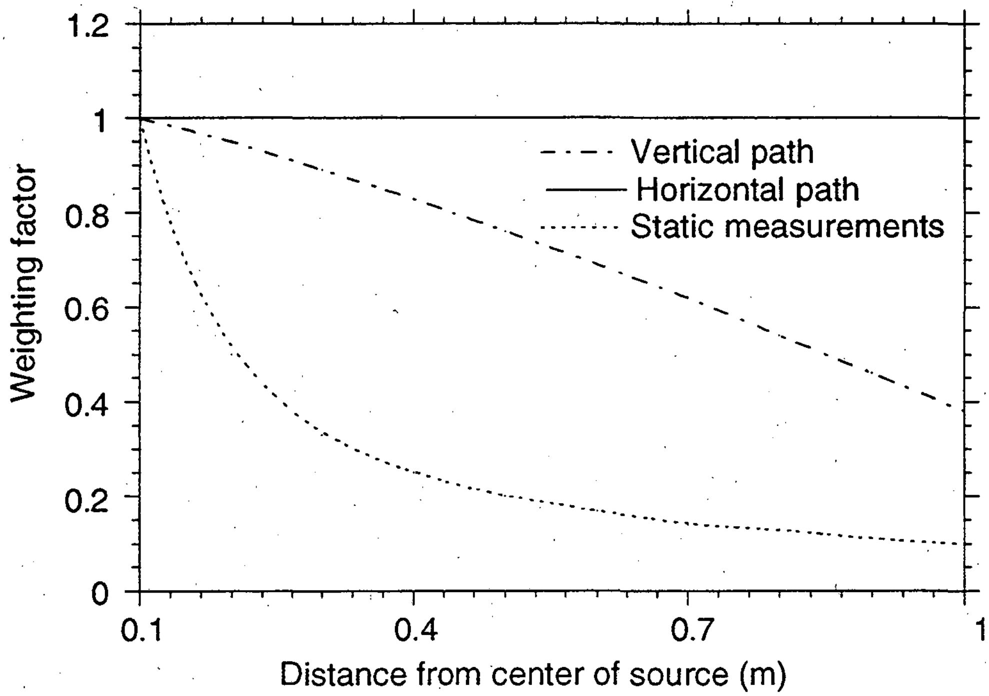

Figure 6. Weighting factors of soil permeability as a function of distance from the source probe. Curves are for the horizontal and vertical path measurements indicated in Figure 5b and for static pressure measurements. The source probe is assumed to be at depth (L) = 2 m.

APPENDIX

Derivation of the Green's Function Solution for the One-Dimensional Diffusion Equation with a Time-Dependent Boundary Condition

In this appendix a solution is derived for the one-dimensional diffusion equation with a time-dependent boundary condition by first considering the solution to the same problem with a step-function boundary condition at the origin. The problem is defined for an arbitrary function U(x,t), given that:

$$(1.a)\quad \frac{\partial U}{\partial t} = D\frac{\partial^2 U}{\partial x^2} \qquad x>0,\ t>0$$

and having the initial and boundary conditions:

$$(1.b)\quad U(x,0) = 0 \qquad \text{for all } x$$

$$(1.c)\quad U(0,t) = 1 \qquad \text{for } t>0\ .$$

Using Laplace transforms in the time domain, such that

$$L[U(x,t)] = G(x,s)\ ,$$

we take the transform of both sides of Eq. 1.a to obtain

$$(2.a)\quad sG = D\frac{\partial^2 G}{\partial x^2}\ .$$

This is an ordinary differential equation with the general solution:

$$(2.b)\quad G(x,s) = c_1 e^{\sqrt{\frac{s}{D}}x} + c_2 e^{-\sqrt{\frac{s}{D}}x}\ .$$

Since $U(x\rightarrow\infty) \rightarrow 0$, then $G(x\rightarrow\infty)$ must be finite, which implies that $c_1 = 0$.

To evaluate c_2, we apply the Laplace transform to the initial condition and boundary condition (Eqs. 1.b and 1.c), giving

(2.c) $L[U(x,0)] = L[0] = 0 = G(x,0)$

(2.d) $L[U(0,t)] = L[1] = \frac{1}{s} = G(0,s)$.

Substituting Eq. 2.d into 2.b with $c_1 = 0$, yields $c_2 = 1/s$. Therefore,

(2.e) $$G(x,s) = \frac{1}{s} e^{-\sqrt{\frac{s}{D}}x}$$

Taking the inverse transform yields

(2.f) $$U(x,t) = L^{-1}\left[\frac{e^{-\sqrt{\frac{s}{D}}x}}{s}\right] = \operatorname{erfc}\left(\frac{x}{\sqrt{4Dt}}\right) = 1 - \operatorname{erf}\left(\frac{x}{\sqrt{4Dt}}\right)$$

$$= \operatorname{erf}(\infty) - \operatorname{erf}\left(\frac{x}{\sqrt{4Dt}}\right)$$

$$= \frac{2}{\sqrt{\pi}}\int_0^{\infty} e^{-\xi^2} d\xi - \frac{2}{\sqrt{\pi}}\int_0^{\frac{x}{\sqrt{4Dt}}} e^{-\xi^2} d\xi$$

$$= \frac{2}{\sqrt{\pi}}\int_{\frac{x}{\sqrt{4Dt}}}^{\infty} e^{-\xi^2} d\xi \ .$$

For simplicity, we will rename the solution:

(2.g) $$\Phi(x,t) = \frac{2}{\sqrt{\pi}}\int_{\frac{x}{\sqrt{4Dt}}}^{\infty} e^{-\xi^2} d\xi \ .$$

Now we consider a step function boundary condition of arbitrary magnitude that is imposed at $t = \tau_0$. The full problem is now described by:

(3.a) $$\frac{\partial U}{\partial t} = D\frac{\partial^2 U}{\partial x^2} \qquad x>0,\ t>0$$

(3.b) $U(x,0) = 0$

(3.c) $$U(0,t) = \begin{cases} 0 \text{ for } 0 \le t < \tau_o \\ A(\tau_o) \text{ for } t > \tau_o \end{cases},$$

where τ_0 is a constant, and therefore $A(\tau_0)$ is also a constant. This boundary condition may be drawn as in Figure 1.

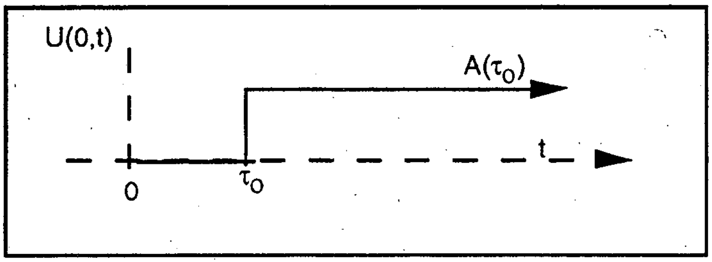

Figure 1. Step function boundary condition.

This is identical to the problem just solved, except that the time of onset of the boundary condition has been translated by τ_0, and the magnitude of the signal at the boundary is scaled from one to $A(\tau_0)$. The solution therefore becomes:

(3.d) $$U(x,t) = A(t_o)\Phi(x, t - t_o)\ .$$

Now consider another boundary condition:

(4.a) $$U(0,t) = \begin{cases} 0 \text{ for } 0 \le t < \tau_o \\ A(\tau_o) \text{ for } \tau_o \le t < \tau_o + \Delta\tau_o \\ 0 \text{ for } t \ge \tau_o + \Delta\tau_o \end{cases}$$

represented graphically as:

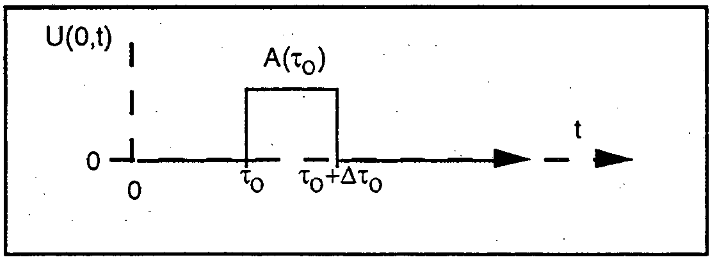

Figure 2. Boundary conditions determined by sum of two step functions.

Using the principal of superposition, we know that the effect of the boundary condition of Figure 2 can be captured by summing the solution to two problems with the boundary conditions shown in Figure 3.

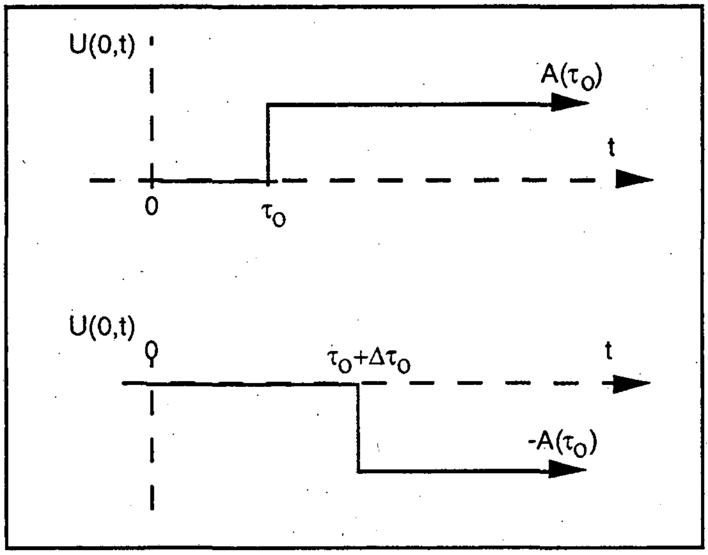

Figure 3. Boundary condition of Fig. 2 decomposed into two parts.

Using Eq. 3.d, the solution is:

(4.b) $U(x,t)=A(\tau_0)\Phi(x,t-\tau_0)-A(\tau_0)\Phi(x,t-(\tau_0+\Delta\tau_0))$ for $t > \tau_0+\Delta\tau_0$.

Finally, we consider the superposition of many such signals to create an arbitrary functional form for the boundary condition.

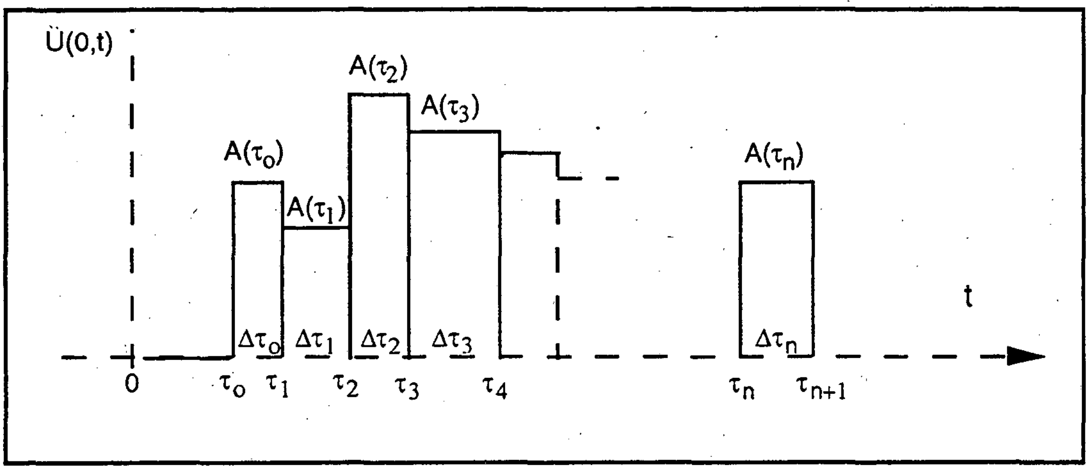

Figure 4. Creation of an arbitrary boundary condition by the superposition of many step functions.

The solution is obtained by summing the contributions of each A(τ_j) for j = 0,...n. From Eq. 4.b, it follows that the solution to this new problem is:

$$\begin{aligned} \text{(5.a)} \qquad U(x,t) = {} & A(\tau_o)\{\Phi(x,t-\tau_o)-\Phi(x,t-(\tau_o+\Delta\tau_o)\}+ \\ & A(\tau_1)\{\Phi(x,t-\tau_1)-\Phi(x,t-(\tau_1+\Delta\tau_1))\}+\ldots \\ & A(\tau_n)\{\Phi(x,t-\tau_n)-\Phi(x,t-(\tau_n+\Delta\tau_n))\} \end{aligned}$$

$$\begin{aligned} = {} & A(\tau_o)\left\{\frac{\Phi(x,t-\tau_o)-\Phi(x,t-(\tau_o+\Delta\tau_o))}{\Delta\tau_o}\right\}\Delta\tau_o + \\ & A(\tau_1)\left\{\frac{\Phi(x,t-\tau_1)-\Phi(x,t-(\tau_1+\Delta\tau_1))}{\Delta\tau_1}\right\}\Delta\tau_1+\ldots \\ & A(\tau_n)\left\{\frac{\Phi(x,t-\tau_n)-\Phi(x,t-(\tau_n+\Delta\tau_n))}{\Delta\tau_n}\right\}\Delta\tau_n \end{aligned}$$

Or, in other notation:

$$\text{(5.b)} \qquad U(x,t) = \sum_{j=0}^{n} A(\tau_j)\left\{\frac{\Phi(x,t-\tau_j)-\Phi(x,t-(\tau_j+\Delta\tau_j))}{\Delta\tau_j}\right\}\Delta\tau_j \ .$$

Using the fundamental theorem of calculus, in the limit that the time intervals $\Delta\tau_j$ approach zero, we obtain a continuous function:

$$(5.c) \qquad U(x,t) = \int_0^t A(\tau)\frac{\partial\Phi(x,t-\tau)}{\partial\tau}d\tau \ .$$

The derivative can be calculated using Leibnitz' Rule:

$$(5.d) \qquad \frac{\partial\Phi}{\partial t} = \frac{2}{\sqrt{\pi}}\frac{\partial}{\partial t}\left(\int_{\frac{x}{\sqrt{4Dt}}}^{\infty} e^{-\xi^2}d\xi\right) = \frac{xe^{-\frac{x^2}{4Dt}}}{t\sqrt{4\pi Dt}} \ .$$

Substituting Eq. 5.d into 5.c, the full solution is:

$$(5.e) \qquad U(x,t) = \int_0^t A(\tau)\frac{x}{t-\tau}\frac{e^{\frac{-x^2}{4D(t-\tau)}}}{\sqrt{4\pi D(t-\tau)}}d\tau$$

$$(5.f) \qquad U(x,t) = \int_0^t A(\tau)\frac{x}{t-\tau}K(x,t-\tau)d\tau \ .$$

Where K(x,t) is the solution to the one-dimensional diffusion equation given an step-function source of magnitude one. The product of the last two terms in the integrand can be thought of as a Green's function for the one-dimensional diffusion equation with a time dependent boundary condition

The same procedure as outlined above may be used to determine the solution for a problem, the boundary condition of which is defined at $x = a$ rather than at $x = 0$. In that case, the basic problem may be defined, analogous to Eqs. 1.a – c, as:

$$(6.a) \qquad \frac{\partial U}{\partial t} = D\frac{\partial^2 U}{\partial x^2} \qquad x>a,\ t>0$$

$$(6.b) \qquad U(x,0) = 0$$

$$(6.c) \qquad U(a,t) = 1$$

which has the solution:

(6.d) $U(x,t) = \Phi(x\text{-}a,t)$,

We proceed as outlined above with the solution for the step function boundary condition (Eq. 3.d) replaced by:

(7) $U(x,t) = A(\tau_0)\,\Phi(x\text{-}a,t\text{-}\tau_0)$.

And the final Green's function solution is simply translated by x = a, yielding:

(8) $$\boxed{U(x,t) = \int_0^t A(\tau)\frac{(x-a)}{(t-\tau)}\frac{e^{\frac{-(x-a)^2}{4D(t-\tau)}}}{\sqrt{4\pi D(t-\tau)}}d\tau} \qquad x>a \ .$$

CHAPTER IV

Soil Column Verification of the Dual-Probe Dynamic Pressure Technique for Measuring Soil Permeability to Air

SYNOPSIS

This chapter describes laboratory verification of the dynamic pressure technique for measuring the permeability of soil to air. A 2.5-m long, 0.15-m ID, soil column is used to run one-dimensional tests of the dynamic technique. The results are compared to the traditional method of measuring permeability in a soil column, using a steady flow of air to produce a constant pressure difference across the soil. The experiments are used (1) to ensure that estimates of permeability obtained from static and dynamic measurements agree, (2) in particular, to test the validity of the mathematical model used to interpret the dynamic pressure measurements of permeability, (3) to test the response of the system and the model to changes in the source signal frequency, and (4) to ensure that scale-dependent permeability observed in the field is not an artifact of the dynamic measurement technique.

A moderate (20%) discrepancy was found between the steady and dynamic estimates of permeability, the source of which is not clear. This magnitude of disagreement does not pose problems for the proposed use of the technique to investigate potential scale dependence of soil permeability to air in the field for two reasons. First, the discrepancy we seek to resolve in the field is considerably larger (a factor of 7 or 8). Second, and more important, the 20% discrepancy observed in the column is *independent* of scale.

The soil column experiments produced two important negative results. First, the dynamic pressure estimates of soil permeability were insensitive to a factor of 4 change in source signal driving frequency. Second, no significant scale dependence of soil permeability was observed in the column using either measurement technique—an expected result for a soil column packed with uniform dry sand.

INTRODUCTION

Chapter III described the development of a technique for measuring soil permeability to air *in situ* and over a range of length scales between about 0.5 and 5 m in near-surface soil. The dual-probe dynamic pressure (DPD) technique uses the lag time for a sinusoidally oscillating pressure signal to travel from a source probe to a detector probe as a basis for determining soil permeability to air along the path between the probes. In Chapter III, a comparison of DPD field data with single-probe steady-state permeability measurements suggested that soil permeability to air depended on measurement length scale. This chapter describes well-controlled laboratory experiments designed to validate the DPD technique.

This work has a number of specific goals: (1) to test that the dynamic pressure measurements of permeability agree with standard Darcy measurements run at steady state, (2) to validate the mathematical model that is used to interpret the dynamic pressure measurements, in particular, the assumption of linearity of the governing equation, (3) to verify that the response of the system to changes in the dynamic-signal driving frequency is accurately predicted by the model, and (4) to verify that field observations of scale dependence of soil permeability are not merely an artifact of the dynamic measurement technique.

This chapter describes soil column experiments used to investigate the issues outlined above. A mathematical model is first developed for the one-dimensional geometry of the soil column. The apparatus allows a direct comparison between estimates of soil permeability based on measurements using the dynamic technique versus those based on the usual steady-flow technique. In addition, by measuring permeability across different portions of the 2.5-m-long column, we can test for the existence of anomalous scale effects that might be created by the measurement technique itself.

THEORY

Model Development

This section develops a theoretical model for interpretation of the dynamic pressure measurements of permeability in the soil column. In this case, flow is restricted to one dimension, the z-direction. Following the 3-dimensional derivation in Chapter III, the governing equation for a pressure signal propagating through the soil column under conditions of Darcy flow is given by:

$$(1) \qquad \frac{\partial P}{\partial t} = \frac{k}{\varepsilon\mu}\left(P_a \frac{\partial^2 P}{\partial z^2} + \left(\frac{\partial P}{\partial z}\right)^2\right) .$$

As before, P is the disturbance pressure, k is the permeability of soil to air, ε is the air-filled porosity of the soil, μ is the dynamic viscosity of air at ambient conditions (1.81×10^{-5} Pa s), and P_a is the mean atmospheric pressure.

Again, we make the assumption that the non-linear term is insignificant. That is,

$$(2) \qquad \frac{\partial^2 P}{\partial z^2} >> \frac{1}{P_a}\left(\frac{\partial P}{\partial z}\right)^2 .$$

The validity of this assumption will be tested by the outcome of the experiments conducted using the soil column.

We are left with the task of solving the diffusion equation

$$(3) \qquad \frac{\partial P}{\partial t} = D_P \frac{\partial^2 P}{\partial z^2} ,$$

where the diffusion coefficient for propagation of the pressure signal, D_p, is again given by $kP_a/\varepsilon\mu$. The z axis is taken as positive upward.

To properly simulate the soil column experiments, different boundary conditions must be imposed from those of the three-dimensional problem described in Chapter III. As indicated in the schematic diagram of Figure 1, the sinusoidally oscillating source signal is imposed at the soil's bottom surface (at the source port (P0) z = 0). The volume occupied by the soil has length L = 2.27 m, and the detector signal is probed at various distances, z, from the origin at probes P1 - P4. The top of the column is open to the atmosphere during these experiments.

The boundary conditions for the pressure signal are therefore given by

(4.a) $P(z = 0,t) = P_o \cos(\omega t)$ for $t > 0$

(4.b) $P(z = L,t) = 0$ for $t > 0$,

where P_o is the constant amplitude of the source signal and ω is the constant source signal frequency.[1]

As in Chapter III, we will solve the problem for the non-transient part of the pressure signal, looking for a solution of the form

$$P(z,t) = \phi(z)e^{i\omega t} \quad . \tag{5}$$

Substituting Eq. 5 into Eq. 3, we get a second order ordinary differential equation in ϕ alone. The solution for ϕ is as follows (cf. Chapter III, Eq. 19):

$$\phi(z) = \alpha_1 e^{\frac{\lambda z}{\sqrt{2}}(1+i)} + \alpha_2 e^{-\frac{\lambda z}{\sqrt{2}}(1+i)} \tag{6}$$

where

$$\lambda = \sqrt{\frac{\omega}{D_p}} \quad . \tag{7}$$

The general solution for P(z,t) is, therefore,

$$P(z,t) = \alpha_1 e^{i\omega t} e^{\frac{\lambda z}{\sqrt{2}}(1+i)} + \alpha_2 e^{i\omega t} e^{-\frac{\lambda z}{\sqrt{2}}(1+i)} \quad . \tag{8}$$

We now need to apply the boundary conditions to evaluate of the complex coefficients α_1 and α_2. Using the complex form of Eq. 4.a, $P(0,t) = P_o e^{i\omega t}$, yields

$$\alpha_2 = P_o - \alpha_1 \quad . \tag{9}$$

Using the second boundary condition, Eq. 4.b, and the following substitutions,

---

[1] The choice of the boundary condition as cos(ωt) (rather than sin(ωt), as used in Chapter III for the 3-dimensional system) is arbitrary. In Chapter III, sin(ωt) was used for consistency with the solution of Fukuda [1]. In this case, I choose cos(ωt) because it simplifies the solution to this problem. These choices have no effect on the ultimate solution, since we are seeking phase shifts between signals at two locations in space rather than the absolute form of the signal.

$$L' = \frac{\lambda L}{\sqrt{2}}\,, \tag{10}$$

we get

$$\alpha_2 = -\alpha_1 \frac{e^{L'(1+i)}}{e^{-L'(1+i)}}\ . \tag{11}$$

Equating the right hand sides of Eqs. 9 and 11, we obtain

$$\alpha_1 = \frac{-P_o e^{-L'(1+i)}}{e^{L'(1+i)} - e^{-L'(1+i)}} \tag{12}$$

and

$$\alpha_2 = \frac{P_o e^{L'(1+i)}}{e^{L'(1+i)} - e^{-L'(1+i)}}\ . \tag{13}$$

Substituting Eqs. 12 and 13 into Eq. 8, we find the complex form of the particular solution:

$$P(z,t) = \frac{-P_o e^{(-L'+z')} e^{i(\omega t - L' + z')}}{e^{L'} e^{iL'} - e^{-L'} e^{-iL'}} + \frac{P_o e^{(L'-z')} e^{i(\omega t + L' - z')}}{e^{L'} e^{iL'} - e^{-L'} e^{-iL'}} \tag{14}$$

where $z' = \left(\lambda z / \sqrt{2}\right)$. Multiplying through by the complex conjugate of the denominator, and taking the real part of the solution, we get

$$\boxed{P(z,t) = \frac{P_o}{e^{2L'} + e^{-2L'} - 2\cos(2L')} \begin{Bmatrix} e^{z-2L'} \cos(\omega t + z') - e^{z'} \cos(\omega t + z' - 2L') \\ + e^{-z'+2L'} \cos(\omega t - z') - e^{-z'} \cos(\omega t - z' + 2L') \end{Bmatrix}}\ . \tag{15}$$

To obtain a functional form for the time lag between the source and detector signals, we would like an expression for the pressure signal in the form

$$P(z,t) = \gamma \cos(\omega t + \delta)\,. \tag{16}$$

We use the following substitutions:

$$A = \frac{P_o}{e^{2L'} + e^{-2L'} - 2\cos(2L')} \tag{17}$$

and

$$\begin{aligned} B &= e^{z-2L'} \\ C &= e^{z'} \\ D &= e^{-z'+2L'} \\ E &= e^{-z'} \end{aligned} \tag{18a – d}$$

substituting into Eq. 15 yields

$$P(z,t) = A\begin{Bmatrix} B\cos(\omega t + z') - C\cos(\omega t + z' - 2L') + \\ D\cos(\omega t - z') - E\cos(\omega t - z' + 2L') \end{Bmatrix} . \tag{19}$$

We simplify the problem of reducing P(z,t) to the form of Eq. 16 by making it a two step process. First we reduce the first and second terms, and then the third and fourth terms, in the sum of Eq. 19, to the equivalent forms of Eq. 16, then we combine the results. That is, we make the following substitutions:

$$\gamma_1 \cos(\omega t - \delta_1) = B\cos(\omega t + z') - C\cos(\omega t + z' - 2L') \tag{20}$$

$$\gamma_2 \cos(\omega t - \delta_2) = D\cos(\omega t - z') - E\cos(\omega t - z' + 2L') . \tag{21}$$

Therefore, Eq. 19 can be rewritten

$$P(z,t) = A\gamma_3 \cos(\omega t - \delta_3) = A[\gamma_1 \cos(\omega t - \delta_1) + \gamma_2 \cos(\omega t - \delta_2)] . \tag{22}$$

The procedure for solving for the γ and δ parameters is similar to that outlined in the Chapter III is shown only for Eq. 20. First the cosines of the sums are expanded using the trigonometric identity

$$\cos(x + y) = \cos(x)\cos(y) - \sin(x)\sin(y) . \tag{23}$$

The right hand side of Eq. 20 becomes

$$\begin{aligned}\gamma_1 \cos(\omega t-\delta_1) = {} & B\cos(\omega t)\cos(z') - B\sin(\omega t)\sin(z') \\ & - C\cos(\omega t)\cos(z'-2L') + C\sin(\omega t)\sin(z'-2L') \ .\end{aligned} \tag{24}$$

Or, regrouping,

$$\begin{aligned}\gamma_1 \cos(\omega t-\delta_1) = {} & \cos(\omega t)[B\cos(z') - C\cos(z'-2L')] \\ & + \sin(\omega t)[C\sin(z'-2L') - B\sin(z')] \ .\end{aligned} \tag{25}$$

But, the left hand side of Eq. 26 also can be rewritten

$$\gamma_1 \cos(\omega t-\delta_1) = \cos(\omega t)\gamma_1\cos(\delta_1) + \sin(\omega t)\gamma_1\sin(\delta_1). \tag{26}$$

Therefore, comparing the right hand sides of Eqs. 25 and 26

$$\gamma_1\cos(\delta_1) = [B\cos(z') - C\cos(z'-2L')] \tag{27}$$
$$\gamma_1\sin(\delta_1) = [C\sin(z'-2L') - B\sin(z')] \tag{28}$$

and solving for γ_1 and δ_1 we obtain

$$\delta_1 = \tan^{-1}\left(\frac{-B\sin(z') + C\sin(z'-2L')}{+B\cos(z') - C\cos(z'-2L')}\right) \tag{29.a}$$

$$\gamma_1 = \frac{-B\sin(z') + C\sin(z'-2L')}{\sin(\delta_1)} \ . \tag{29.b}$$

Following a similar procedure, Eqs. 21 and 22 are solved for γ_2, γ_3, δ_2, and δ_3.

$$\delta_2 = \tan^{-1}\left(\frac{D\sin(z') - E\sin(z'-2L')}{D\cos(z') - E\cos(z'-2L')}\right) \tag{30.a}$$

$$\gamma_2 = \frac{D\sin(z') - E\sin(z'-2L')}{\sin(\delta_2)} \ . \tag{30.b}$$

$$\delta_3 = \tan^{-1}\left(\frac{\gamma_1\sin(\delta_1) + \gamma_2\sin(\delta_2)}{\gamma_1\cos(\delta_1) + \gamma_2\cos(\delta_2)}\right) \tag{31.a}$$

(31.b) $$\gamma_3 = \frac{\gamma_1 \sin(\delta_1) + \gamma_2 \sin(\delta_2)}{\sin(\delta_3)}$$

The new form of the solution,

(32) $$P(z,t) = A\gamma_3 \cos(\omega t - \delta_3) \ ,$$

tells us that the phase lag of the signal at the detector location is given by δ_3 and the amplitude by $A\gamma_3$. The time lag, T, between the source and detector signals is simply:

(33) $$T = \frac{\delta_3}{\omega} \ .$$

As with the three-dimensional dynamic pressure experiments, the time lag, and not the amplitude is used as the indicator of permeability since the time lag can be acquired with greater precision from the Fast Fourier Transform (FFT) of the data than can the amplitude. Even if a perfect sinusoidal signal of finite length is used as input to the FFT, the numerical solution will transfer some of the power from the driving frequency signal into adjacent bands, making it difficult to reconstruct the actual amplitude without having to obtain and analyze data for an excessive period of time.

As noted for the solution to the three-dimensional problem described in Chapter III, care must be exercised in interpreting the solution in this form since half cycles of phase lags are indicated by changing the sign of the amplitude term rather than by adding an additional π radians to δ_3, and phase lags separated by integer numbers of full cycles are indistinguishable. To ensure correct interpretation of the data, we begin the analysis procedure by generating T for very high permeabilities for which we know that the phase lags are less than one half cycle and then decrease the permeability incrementally. Since we know that the time lag must increase monotonically with decreasing permeability, the correct solutions can be interpreted with little difficulty.

EXPERIMENTAL METHODS

This section describes the apparatus and experimental methods for the steady-state and dynamic measurements of permeability made using the soil column.

Description of the Soil Column

Figure 1 is a schematic of the soil column apparatus. The column is 2.5-m long, has an ID of 0.15 m, and is constructed of polyvinyl chloride pipe. At the bottom of the pipe, stainless steel mesh (100-mesh) is supported on a perforated stainless steel disk to contain the soil. These supports are sealed against the bottom of the pipe by means of a PVC cap. The air space inside the cap is used for the introduction of the dynamic and steady source signals. A lid containing a flow collector port is sealed to the top of the column to measure the flow rate of air leaving the column during the static experiments. During dynamic experiments the top of the column is left open.

The soil column contains a number of ports for controlling and monitoring pressures. These ports are all constructed of pipe-to-tube fittings. The pipe end is inserted into previously tapped threads in the column, cap, and lid using Teflon® tape to create a good seal. The cap at the base of the column contains two ports, one for introducing the source signal, the other (P0) for monitoring pressure. Four additional pressure monitoring ports, P1 - P4, are installed at distances of 0.5, 1.0, 1.5, and 1.85 meters from the mesh, respectively. These fittings do not extend beyond the interior wall of the pipe. The inside of each of the four ports is bored to allow the introduction of 0.64 cm OD (1/4") stainless steel tubing installed so that pressure can be monitored along the center line of the column. To facilitate uniform packing, the tubes are only emplaced after the column is packed with soil. During the experiments, the soil column was filled to height of 2.27 m of dry 60-mesh sand (particle grain size ≤ 0.25 mm).

Data acquisition and control (DAC) were handled by commercially available software (Genesis, Iconics, Foxborough, Massachusetts) running on an AST-286 personal computer. Pressures were measured using two electronic digital micromanometers (EDM) (Neotronics, Gainesville, Georgia) with ~1 Pa resolution. The analog output signals were logged with the DAC system at 0.5 s intervals. The EDMs were calibrated prior to each set of experiments using a liquid micromanometer with a 0.25 Pa resolution (Dwyer Instruments, Inc., Michigan City, Indiana). Air flow to the soil column was regulated by computer-controlled mass flow controllers (Sierra Instruments, Inc., Monterey, California).

The air-filled porosity of the sand was determined by water displacement in two replicate measurements. Using the assumption that uniform dry sand packs similarly in a small volume or a large volume, porosity measurements were made on a small sample volume. A 15 ± 1 cm^3 volume of dry sand, V_{sand}, was measured using a graduated cylinder. Another 50-ml graduated cylinder was then filled with 25 ml of water and the inside walls of the cylinder, above the water, were dried using a heat gun to prevent sticking when the previously measured volume of sand was poured into the water of the cylinder. The sand was then stirred with a glass rod and acoustically vibrated to remove all air. The volume of the solid portion of the sand, V_{sol}, was then determined from the difference between the water only and the water plus sand. The air filled porosity, ε, of the original volume of dry sand is determined from $(V_{sand} - V_{sol})/V_{sand}$, and found to be 0.43 ± 0.02.

Steady-state permeability measurements

In theory, it is straightforward to determine soil permeability from steady-state measurements using a soil column since the experimental configuration represents a direct application of Darcy's law. A steady flow of air, Q, is directed into the bottom of the soil column. The resulting pressure difference, ΔP, between two locations in the column, gives the permeability between them using the simple relationship:

$$k = \frac{\mu Q L}{A \Delta P}. \tag{34}$$

The random measurement error is given by

$$\sigma_k = \sqrt{\left(\frac{\mu L}{A\Delta P}\right)^2 \sigma_Q^2 + \left(\frac{\mu Q}{A\Delta P}\right)^2 \sigma_L^2 + \left(\frac{\mu Q L}{A\Delta P^2}\right)^2 \sigma_{\Delta P}^2}\,, \tag{35}$$

given that μ and A are known precisely.

The parameter A is the cross sectional area of the interior of the column and L is the distance between the two pressure sampling locations. During these experiments, the lid was sealed to the top of the soil column and the flow was directed via port 5 to an electronic bubble-flow calibration device (Gilibrator, Gilian Instrument Corp., Caldwell, N.J.) to determine accurately the steady flow rates.

Dynamic Pressure Measurements

As with the dual-probe dynamic pressure measurements used in the field, a sinusoidally oscillating flow is used to generate the source signal. Again, this is achieved by combining the flows from two mass flow controllers. One directs a steady flow away from the column: $Q = -B$. The other directs an oscillating flow toward the column: $Q = B + A\cos(\omega t)$.

In a given experiment the time lag is measured between the source location, P0, and one of the other detector ports, P1 - P4. Experiments were conducted at several different driving frequencies. A test was run to determine whether different response times of the source and detector EDMs might introduce an offset in the observed response times during normal experiments. In that test, the two EDMs were connected together to the same sampling location and the time lag measured as in the other experiments.

As with earlier experiments, the time lags are determined using Fast Fourier Transforms of the source and detector signals. The measured difference between the phases of the two signals at the source driving frequency, $\Delta\delta_m$, is calculated. The measured lag time, T_m, is then obtained from:

$$T_m = \frac{\Delta\delta_m}{\omega} \quad (36)$$

Finally, the air permeability for the path under consideration is determined by comparing the measured time lag with theoretical curves of permeability vs. time lag generated from Eq. 33.

RESULTS

The results of all of the steady-state measurements of soil permeability are shown in Table I. Measurements were made at several flow rates for each probe location. The table shows the length of the soil column between the supply location (P0) and the location of the second EDM detector, the flow rate, and the permeability calculated from each experiment. The last column gives the average permeability calculated for the path length.

The results of the dynamic permeability measurements are given in Table II. Again the detector port location is indicated. At some ports the permeabilities were measured using two different driving frequencies (indicated). The measured time lags, T_m, are shown for each of the experiments including the test for which both EDMs were recording the same signal. When calculating permeabilities, this lag, resulting from a small difference in the response time of the two detectors, is accounted for by subtracting that amount from the measured time lags across the soil pathway. The correction is relatively small, less than 10% at its largest. The uncertainty in the permeability, based on the uncertainty in the measured time lags, is estimated to be less than or equal to 0.3×10^{-11} m^2 for all measurements.

DISCUSSION

As the results in Tables I and II indicate, there is a consistent discrepancy of ~20% between the estimates of permeability based on the two techniques. The source of this discrepancy is not clear. It might result from an error arising from the assumption of linearity (Eq. 2), or it might reflect a systematic error of some other origin, or both. The possibility that neglecting the nonlinear term is the source of the discrepancy should in principle be testable by varying the amplitude of the source signal, since scale analysis of Eq. 2 indicates that the discrepancy should be smaller as P/P_a decreases. We plan to conduct such experiments in the future.

Another possible source of the 20% discrepancy might be deviation from ideal conditions due to preferred flow along the walls of the soil column. In that case, in steady-state experiments, during which flow is kept at some fixed value, slippage along the wall might result in higher flows than the soil itself would let pass, leading to an overestimate of the permeability of soil in the column. This effect should be larger in the steady-state measurements than the dynamic measurements, in which average flows are ~zero and the maximum flow is about the same as the steady flow used in the steady-state experiments. This hypothesis could be tested by rerunning the experiments described here in a soil column of considerably larger cross-sectional area. Such a column is currently being built by our group at Lawrence Berkeley Laboratory and could be used for this purpose.

Two negative results from the soil column experiments are encouraging. First, no significant or systematic scale dependence is evident over the range of scales studied. (Note that although the dynamic measurement of permeability made at P1, over the shortest soil path (0.5 m), is somewhat smaller than the other measurements, this effect is not significant, given the uncertainties.) This is in agreement with steady-state measurements made at different length scales and is expected given the uniform dry sand with which the column is packed. Second, dynamic measurements conducted with a factor of 4 difference in driving frequencies produce consistent estimates of soil permeability.

CONCLUSIONS

A moderate (20%) discrepancy was observed between the steady-state and dynamic measurements of soil permeability in the laboratory soil column experiments. The magnitude of the discrepancy does not pose a significant problem for the proposed field experiments. In the field we are attempting to interpret a discrepancy of about a factor of 7, according to the results of experiments in Chapter III. More important, since the 20% discrepancy observed in the soil column experiments is *independent* of scale, this effect will not produce anomalies in studies of scale dependence of permeability in field soils. The discrepancy might be an indication of the effect of neglecting the non-linear terms in the governing equation for propagation of the disturbance pressure signal. We plan experiments to test this possibility in the future.

The experiments were also used to check for anomalous results in the dynamic measurements when source signal frequencies are altered or when measurements are made over at different length scales. The dynamic estimates of permeability were insensitive to changes in sources signal frequency of a factor of 4. No scale dependence of permeability was observed in the soil column, as expected for a column packed with uniform sand. Given these results, we conclude that the dynamic measurement technique is suitable for investigating scale-dependent permeability in field soils.

REFERENCE

1. Fukuda, H., Air and vapor movement in soil due to wind gustiness, *Soil Science,* 1955, 4: 249-256.

Table I. Soil permeabilities measured across different lengths of soil in the soil column using steady-state measurements.

Detector port	Length of soil	Q (L min^{-1})	ΔP (Pa)	k (m^2)	σ_k (m^2)	$k_{average}$ (m^2)
P4	1.85	2.64	1252	6.63×10^{-11}	0.48×10^{-11}	6.7×10^{-11}
P4	1.85	2.67	1258	6.67×10^{-11}	0.48×10^{-11}	
P4	1.85	3.39	1601	6.65×10^{-11}	0.48×10^{-11}	
P3	1.50	3.50	1253	7.11×10^{-11}	0.52×10^{-11}	7.1×10^{-11}
P3	1.50	3.50	1263	7.06×10^{-11}	0.52×10^{-11}	
P3	1.50	2.17	789	7.01×10^{-11}	0.51×10^{-11}	
P2	1.00	3.69	881	7.11×10^{-11}	0.55×10^{-11}	7.1×10^{-11}
P2	1.00	2.43	586	7.04×10^{-11}	0.54×10^{-11}	
P2	1.00	3.14	756	7.05×10^{-11}	0.54×10^{-11}	
P1	0.50	3.27	391	7.10×10^{-11}	0.66×10^{-11}	7.0×10^{-11}
P1	0.50	3.92	483	6.89×10^{-11}	0.64×10^{-11}	
P1	0.50	2.67	321	7.07×10^{-11}	0.65×10^{-11}	
Average						7.0×10^{-11}

Table II. Soil permeabilities measured across different lengths of soil in the soil column using dynamic pressure measurements.

Detector port	Signal period (s)	T_m (s)	k (m^2)
4	120	1.22	$5.6 \pm 0.3 \times 10^{-11}$
4	30	1.21	$5.6 \pm 0.3 \times 10^{-11}$
3	30	1.05	$6.0 \pm 0.3 \times 10^{-11}$
2	60	0.85	$5.8 \pm 0.3 \times 10^{-11}$
2	30	0.86	$5.7 \pm 0.3 \times 10^{-11}$
1	30	0.53	$5.3 \pm 0.3 \times 10^{-11}$
0[a]	30	0.04	
Average			5.7×10^{-11}

[a] In this test both EDMs were connected together into the P0 port. The time lag results from a difference in the response time of the two instruments.

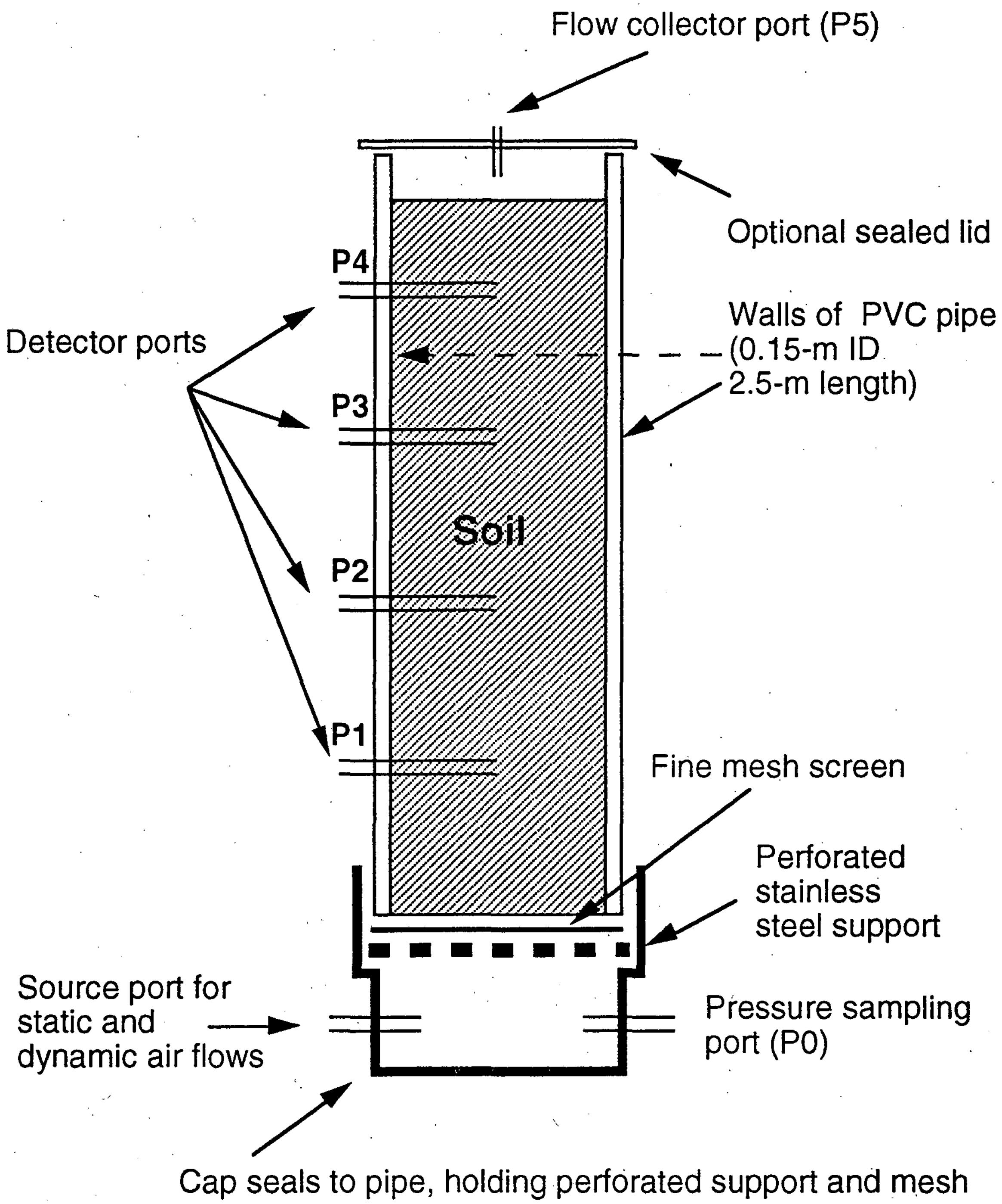

Figure 1. Schematic of soil column.

CHAPTER V

A Field Study of the Scale Dependence of Soil Permeability to Air

SYNOPSIS

Soil permeability to air was measured *in situ* in a natural granitic soil over a range of length scales (0.50 - 3.5 m) using the new dual-probe, dynamic pressure technique. These measurements were compared with regional averages of smaller-scale static measurements of permeability, also made *in situ,* using two types of soil probes with different sampling scales, 0.1 and 0.5 m. The results indicate a strong scale dependence of soil permeability to air—a factor of 35 increase in length scale producing more than a factor of 40 increase in permeability. Although the soil is moderately anisotropic, vertical and horizontal permeabilities displayed a similar scale dependence. These results demonstrate that the typical method of assessing regional soil permeabilities (*i.e.,* averaging over multiple small-scale measurements) can produce seriously misleading results if used for determining contaminant transport potential in systems that operate naturally at larger scales. The finding of scale-dependent air permeability in the Ben Lomond soil is consistent with prior findings of scale-dependent hydraulic conductivities in aquifers[1]. At the Ben Lomond site a likely source of this structure appears to be root networks due to California Live Oaks *(Quercus agrifolia)* surrounding the study site and grasses growing on the site.

INTRODUCTION

In Chapter I, it was pointed out that persistent discrepancies exist between model predictions and field measurements of radon and soil-gas entry into houses [2-5], with measured entry always exceeding that predicted by the models. In Chapter II, this discrepancy, which was previously attributed to misunderstanding of inherently complex field sites, was reproduced at a full-scale experimental basement located in natural granitic soil in Ben Lomond, California. The facility was designed for the detailed study of radon and soil-gas entry into basement structures [6, 7]. The cumulative evidence has suggested a plausible explanation for the model-measurement discrepancy: the systematic underestimation of regional soil permeabilities by traditional assessment techniques. Empirical estimates of regional soil permeabilities are the critical empirical inputs for predicting flow rates using soil-gas transport models, just as hydraulic conductivity governs flow in aquifers.

In Chapter III, I discussed the development and preliminary field tests of a new technique for measuring soil permeability to air *in situ*.. The field tests, carried out in the soil surrounding the Ben Lomond radon-transport test structures, suggested that soil air-permeability at the site might depend on length scale. If this soil (and others to be tested in the future) is in fact scale dependent, then traditional estimates of soil permeability, based on averages of multiple small-scale measurements (0.1 - 0.5 m), will not reflect soil permeability at the scale at which houses might interact with soils (several m or more) because of their large size and geometries.[1] Evidence for the large field of influence of houses is given by field measurements of soil depressurization during artificial basement depressurization. Significant pressure coupling between a house and the surrounding soil has been observed out to distances of 5 m [2] and 7 m [2] from real houses.

Individual small-scale measurements may be made *in situ* or using core samples. *In situ* measurements are made by extracting or supplying a constant

---

[1] The actual scale(s) at which a given house interacts with the soil will depend on many factors: the depth of the locations at which soil gas enters the house, the size and shape of the gaps, cracks, or holes in the substructure, the presence or absence of gravel layer, and the details of the structure of the soil.

flow of air into the subsurface soil via a probe, which typically consists of a cut-off length of galvanized steel pipe that is driven into the soil along the path of an undersized guide hole. Air is injected into the probe from the end protruding from the soil. Soil permeability is determined from the known flow rate and the resulting disturbance pressure difference between the probe tip and the soil surface [6, 7]. This type of measurement is referred to here as a single-probe static (SPS) measurement. The sampling scale of an SPS measurement is determined by the probe geometry and is taken as the radial distance at which the static pressure field is diminished to 5% of its value at the probe tip. Because of practical limitations on probe size, these measurements currently integrate only over length scales of 0.5 m or less.

The goal of this chapter is to test the hypothesis that the Ben Lomond soil has scale-dependent air permeability over the range of scales at which the static permeability measurements obtain information (0.1 - 0.5 m) and that at which the structure operates (~several m or more). This is carried out via a comprehensive set of field measurements made using the dual-probe dynamic measurement technique and using single-probe static measurements made using two different types of soil probes.

EXPERIMENT AND RESULTS

The dual-probe dynamic-pressure (DPD) technique was used to determine the effective permeability of soil to air over a range of path lengths in both the horizontal and vertical direction (see Chapter III for discussion of technique). The technique uses the propagation time for a sinusoidal pressure signal to travel from a source to a detector probe to determine the effective permeability between them. The DPD results are compared with the results of single-probe static (SPS) measurements made at the same site. SPS measurements were made using two different types of probes with different effective sampling radii (r), blunt-end probes (r = 0.1 m), and cylindrical probes (r = 0.5 m) [7].

Figure 1 is a plan view of the experiment site showing the locations and depths of the cylindrical and blunt-end probes and the dynamic measurement paths (marked by arrows). The locations of the two basement structures used for studying radon entry are also shown. Dynamic measurements were made from sources in two locations, south and east of the west structure, using source signals located approximately 5 m from the structure walls. Dynamic measurements from the south-side source were also discussed in Chapter III. Static measurements were made at all probes. Figure 2 shows the experimental configuration for two typical dynamic measurements.

Figure 3 plots the effective permeabilities determined by the DPD technique for different horizontal integration paths, and the range of values (or uncertainty, if n=1) measured at each length scale. The weighted geometric mean permeabilities are also shown for successful SPS measurements at 14 blunt-end probes and 22 cylindrical probes. The geometric mean was used because field studies usually report that permeabilities follow a lognormal probability distribution ([8], p. 80).

Table I shows the weighted arithmetic means and standard deviations (and the weighted geometric means) of the static permeability measurements for the probes shown in Figure 1.[2] The results from horizontal-path dynamic measurements are also indicated, as are the dynamic estimates of vertical permeabilities for 1.5- and 2-m path lengths. (As discussed in Chapter III, the vertical components of permeability are estimated from horizontal and 45-degree-angle DPD measurements having the same path length and a common source probe (see Figure 2) using the concept of a hydraulic conductivity ellipse and assuming that anisotropy is oriented along the horizontal and vertical axes [9].)

As indicated by Figure 3, soil permeability at the site has a strong dependence on sampling scale, with permeability measured at the 3.5-m scale (30 x 10^{-12} m^2) more than 40 times larger than that at the 0.1-m scale (0.7 x 10^{-12} m^2). Note also that despite the fact that the soil is anisotropic, with horizontal permeability ~2x more permeable than vertical, based on the evidence of the vertical permeability estimates at two different length scales, the magnitude of scale dependence appears to be about the same in the two directions (Table I).

---

[2] Note that since we want to compare the results of the dynamic and static measurements in similar regions of soil, the average of the static permeability measurements is taken only for probes in the first 2 m of natural soil. Data from probes in the backfill zones of the structures and from below the structure floors are, therefore, excluded.

DISCUSSION

The scale dependence of permeability at the Ben Lomond site might be explained by the presence of highly permeable, fast-flow paths forming a network through the less permeable soil matrix. Such pathways might be formed by plant roots, animal burrows, and water leaching pathways. The idea is, for example, that roots of different sizes could form nested scales of heterogeneity. Then, as sampling integration length increases, so too would the probability of intercepting larger scales of heterogeneity and therefore decreased flow resistance.

Figure 4 shows a conceptual model of a soil with two scales of permeability and heterogeneity, one defined by structure at the pore scale (*i.e.*, the soil matrix), the other by fast flow paths along larger root networks, animal burrows, or soil weathering pathways. This conceptual model is supported by visual inspection of the soil profile in a 3-m deep trench cut adjacent to the study site [10] and in the excavations for the basement structures. The soil profile reveals a relatively uniformly distributed root network to about 2-m depth. In addition to fine root structures, larger roots (~3 mm diameter) are distributed relatively uniformly at approximately 20 cm intervals. The presence of fast flow channels in the soil is also suggested by the similarity of seasonal SPS-type permeability measurements made at different elevations in the soil [4]. Those data indicate little seasonal change in the moisture content of the bulk soil at 1.5- to 2-m depth despite seasonal saturation and drying of the soil surface, suggesting that groundwater recharge is occurring via transport through fast paths occupying a small total volume of the soil.

In Chapter III the issue was raised that since the dynamic technique is really measuring pressure diffusivity ($D_p = kP_a/\varepsilon\mu$), rather than permeability (k) alone, then it is possible that the effect that we are seeing is really due to scale dependence or frequency dependence (or some combination) of the effective flow porosity (ε) rather than due to scale dependence of permeability. The data set presented in Figure 3 provides two strong arguments that this is *not* the case at the Ben Lomond site. First, the static and dynamic measurements made at the 0.5-m scale agree within measurement uncertainty. Since the static technique only measures k (there are no other undetermined variables), then we know that our choice of ε as the bulk porosity is correct, at least at that scale. In other words, the static measurement provides a sort of calibration of the dynamic technique at that point. The second argument indicates that changing porosity is also not a factor at other points. That argument is that the *slope* of the permeability vs. scale curve indicated by the two sets of static measurements at 0.1 and 0.5 m agrees with the slope of the dynamic measurements at 0.5 m and above. In other words, the static measurements, which are only sensitive to changes in k, show scale dependence that is consistent with the dynamic measurements.

Additional support for the interpretation of scale-dependent permeability comes from the model-measurement comparisons of the soil-gas entry rate vs. depressurization at the Ben Lomond experimental structure (Chapter II). Those measurements also suggest that the soil air-permeability at the scale at which the structure interacts with the soil (> 2 m) is considerably larger than the permeability measured by probes at a scale of 0.5 m. Further support of the dynamic measurements of permeability at the several m scale come from observations of soil-radon concentrations that are presented in Chapter VI.

Scale dependence of permeability is not an unknown phenomenon in fluid flow through porous media, although only one previous study has indicated that this might be the case for soil permeability to air. Schery and Siegel [11] observed a somewhat smaller scale dependence (about half the magnitude of that observed in Ben Lomond) in measurements of vertical permeability of soil to air in natural soil in Socorro, New Mexico. Those tests were conducted at three different length scales of 0.05, 0.56, and 1.0 meters. Measurements at two of those scales were of the static type, and one used propagation of the barometric pressure signal as an indicator. Scale dependence of hydraulic conductivity is a recognized phenomenon at large regional scales. Hydraulic conductivity data compiled by Bradbury and Muldoon [1] of unlithified glacial and fluvial material showed scale dependence of a similar functional form to Fig. 3, however, the largest scale-dependence reported by them was only one tenth the magnitude observed over the same range of scales in Ben Lomond. Scale-dependent permeability is also known in fractured rock systems [12].

This smaller scaling effect in the sandy aquifer than in the Ben Lomond soil might be expected given the nature of the medium and the forces acting upon it. Unsaturated surface soils experience a larger array of physical forces likely to produce high flow networks: shrinkage and expansion from changes in soil moisture, percolation of water, invasion by root structures of different dimensions, and animal burrowing. At the opposite extreme, minimal scaling would be expected in pure uniform dry sand in nature, and none would be expected in a box of equal-sized glass beads.

CONCLUSIONS

The current finding of scale-dependent permeability is consistent with the well known phenomenon scale-dependent permeability in aquifers and fractured rock systems [1, 12]. Few studies exist, however, that demonstrate scale dependence of air-permeability in soils. This study is unique in that scale dependence is demonstrated with high resolution, with a *single* technique, for gas-phase flow in unsaturated soil. Contrary to the conclusions of Bradbury and Muldoon [1], who compiled hydraulic conductivity data on unlithified glacial and fluvial deposits, I suggest that scaling is *not* an anomaly of the sampling technique, but rather that the different techniques *accurately* reflect the potential for flow at the different scales. The data presented here support this because a single technique was used to demonstrate a significant change in permeability with scale and was found to be consistent, given the observed scaling, with measurements made using other techniques that integrate over smaller scales.

The extent to which the finding of scale-dependent permeability resolves the observed model-measurement discrepancy of radon and soil-gas entry into the Ben Lomond structure is discussed in Chapter VI. The finding holds the promise of substantially resolving the model-measurement discrepancy observed in real houses. In addition, the results are also directly applicable to understanding the transport of other gas-phase contaminants that occurs in the first several meters of soil. These applications include transport of: volatile organic contaminants from landfills, solvent vapors from subsurface spills, volatiles from contaminated groundwater. Other applications include study of the exchange biogeochemical trace gases between the soil and atmosphere, water leaching through soil, and pesticide transport to groundwater from surface applications.

The finding of scale-dependence of soil permeability to air has significant implications for both site assessment of pollutant transport potential and for modeling of contaminant transport, suggesting that current methods can yield seriously misleading results (see Chapter VII). These facts and the large magnitude of the scale dependence of permeability observed in the current study argue that it is important to study the prevalence and magnitude of this effect in other soils.

REFERENCES

1. Bradbury, K.R. and Muldoon, M.A., Hydraulic Conductivity Determinations in Unlithified Glacial and Fluvial Materials. In: *Ground Water and Vadose Zone Monitoring,* Nielson, D. M. and Johnson, A. I., Ed. American Society for Testing and Materials: Philadelphia, 1990, 138-151.

2. Nazaroff, W.W., Lewis, S.R., Doyle, S.M., Moed, B.A. and Nero, A.V., Experiments on pollutant transport from soil into residential basements by pressure-driven airflow, *Environmental Science and Technology,* 1987, 21: 459-466.

3. Garbesi, K. and Sextro, R.G., Modeling and field evidence of pressure-driven entry of soil gas into a house through permeable below-grade walls, *Environmental Science and Technology,* 1989, 23: 1481-1487.

4. Revzan, K.L., Fisk, W.J. and Gadgil, A.J., Modeling radon entry into houses with basements: Model description and verification, *Indoor Air,* 1991, 1: 173-189.

5. Garbesi, K., Sextro, R.G., Fisk, W.J., Modera, M.P. and Revzan, K.L., Soil-gas entry into an experimental basement: Model-measurement comparisons and seasonal effects, *Environmental Science and Technology,* 1993, 27: 466-473.

6. Fisk, W.J., Flexser, S., Gadgil, A.J., Holman, H.Y., Modera, M.P., Narasimhan, T.N., Nuzum, T., Revzan, K.L., Sextro, R.G., Smith, A.R., Tsang, Y.W. and Wollenberg, H.A., *Monitoring and Modeling for Radon Entry into Basements: A Status Report for the Small Structures Project.* LBL-27692.; Lawrence Berkeley Laboratory: Berkeley, CA: 1989.

7. Fisk, W.J., Modera, M.P., Sextro, R.G., Garbesi, K., Wollenberg, H.A., Narasimhan, T.N., Nuzum, T. and Tsang, Y.W., *Radon Entry into Basements: Approach, Experimental Structures, and Instrumentation of the*

Small Structures Project. LBL-31864.; Lawrence Berkeley Laboratory: Berkeley, CA: 1992.

8. de Marsily, G., *Quantitative Hydrogeology,* Academic Press, Inc.: New York, 1986.

9. Freeze, R.A. and Cherry, J.A., *Groundwater,* Prentice-Hall, Inc.: Englewood Cliffs, New Jersey, 1979.

10. Brimhall, G.H. and Lewis, C.J., *Differential Element Transport in the Soil Profile at the Ben Lomond Small Structure Radon Site: A Geochemical Mass Balance Study.* Department of Geology and Geophysics, University of California, Berkeley: 1992.

11. Schery, S.D. and Siegel, D., The role of channels in the transport of radon from the soil, *Journal of Geophysical Research,* 1986, 91: 12366-12374.

12. Menduni, G., Scaling permeability in fractured rocks, *EOS, Transactions of the American Geophysical Union,* 1992, 73: 214.

Table I. Permeabilities made over integration distances between 0.1 and 3.5 m using various measurement techniques.

Integration length (m)	Individual measurements k (x 10^{-12} m^2)	Like-scale averages k (x 10^{-12} m^2)	Time of measurements.
0.1[a]		0.4±0.2[0.37][b]	May and September
0.5[a]		3.2±2.4[2.7][c]	September
Horizontal permeabilities[d]			
0.5	5.2±1.0	5.2	September
1.5	21±1.5		September
1.5	19±1.4		September
1.5	14±1.2	18	September
2.0	25±1.6		May
2.0	23±1.5		May
2.0	22±1.5	23	May
2.6	29±1.8	29	May
3.5	26±1.6		September
3.5	29±1.8		September
3.5	36±2.1	30	September

Table continued on next page.

---

[a] For these static measurements, the integration length is the radial distance at which the static pressure field has diminished to 5% of its value at the probe.

[b] Weighted average and standard deviation of 15 static measurements made using blunt-end probes. Weighted geometric mean (GM) indicated in square brackets. Weights for calculating the GM are taken as $\ln(k_i + \sigma_{k_i}) - \ln(k_i)$. Where the k_i and σ_{k_i} are the permeabilities and uncertainties of the individual measurements.

[c] Weighted average and standard deviation of 12 static measurements made using cylindrical probes. Weighted geometric mean indicated in square brackets, with weights calculated as in note 2.

[d] Horizontal permeability measurements from dynamic technique (Chapter III).

Table I. continued

Vertical Permeabilities[e]			
1.5		11	September
2.0		13	May

---

[e] Vertical permeabilities are estimated from horizontal measurements and those made at 45° angle using the concept of a hydraulic conductivity ellipse.

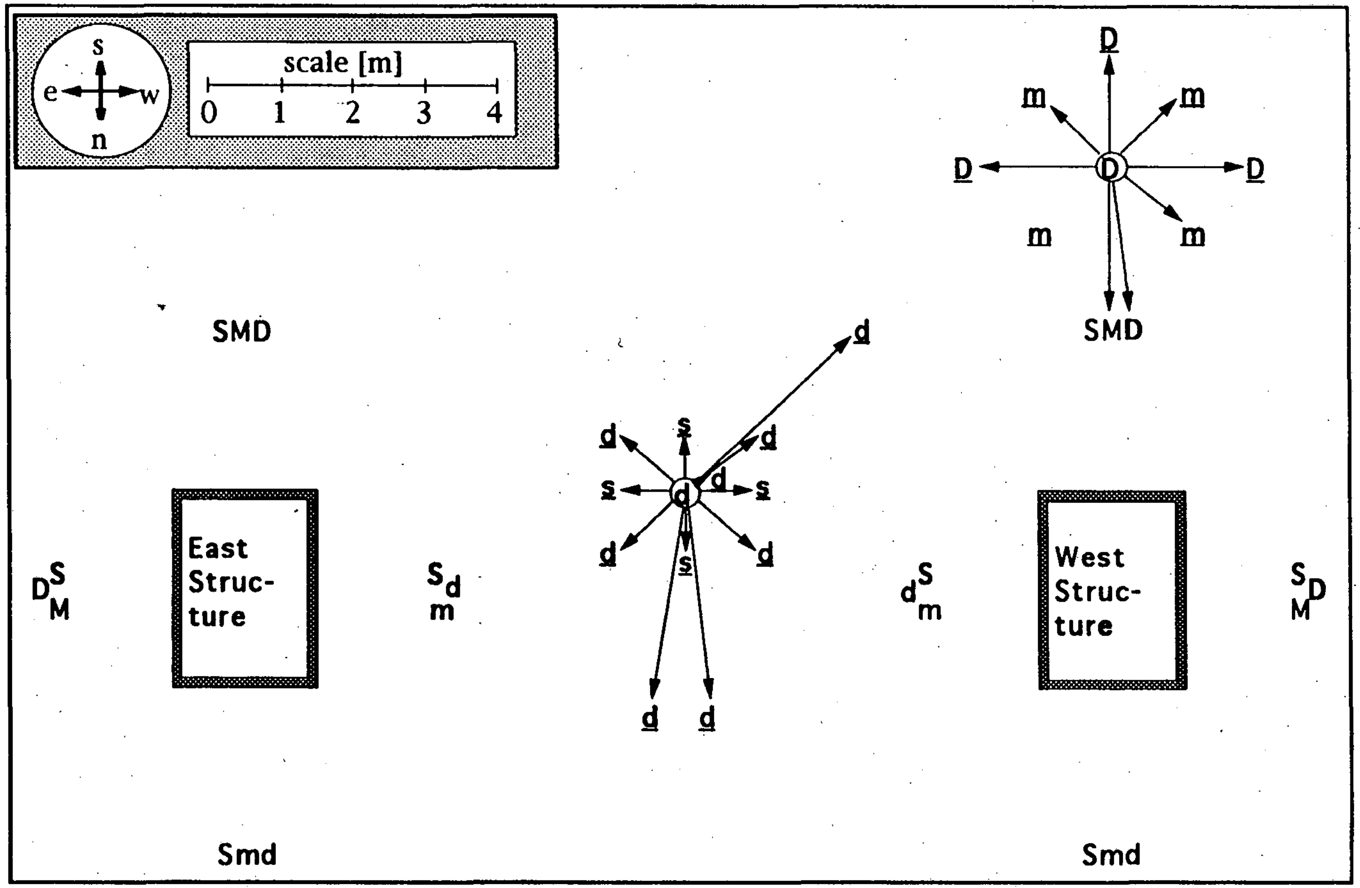

Figure 1. Plan view of Ben Lomond site showing locations of static and dynamic permeability measurements. Alpha characters indicate probe locations (underlined = blunt-end probe; non-underlined = cylindrical probe). Arrows indicate dynamic measurement paths. Probe depths in meters: D(2.0), M(0.8), S(0.18), d(1.5), m(0.59), and s(0.44).

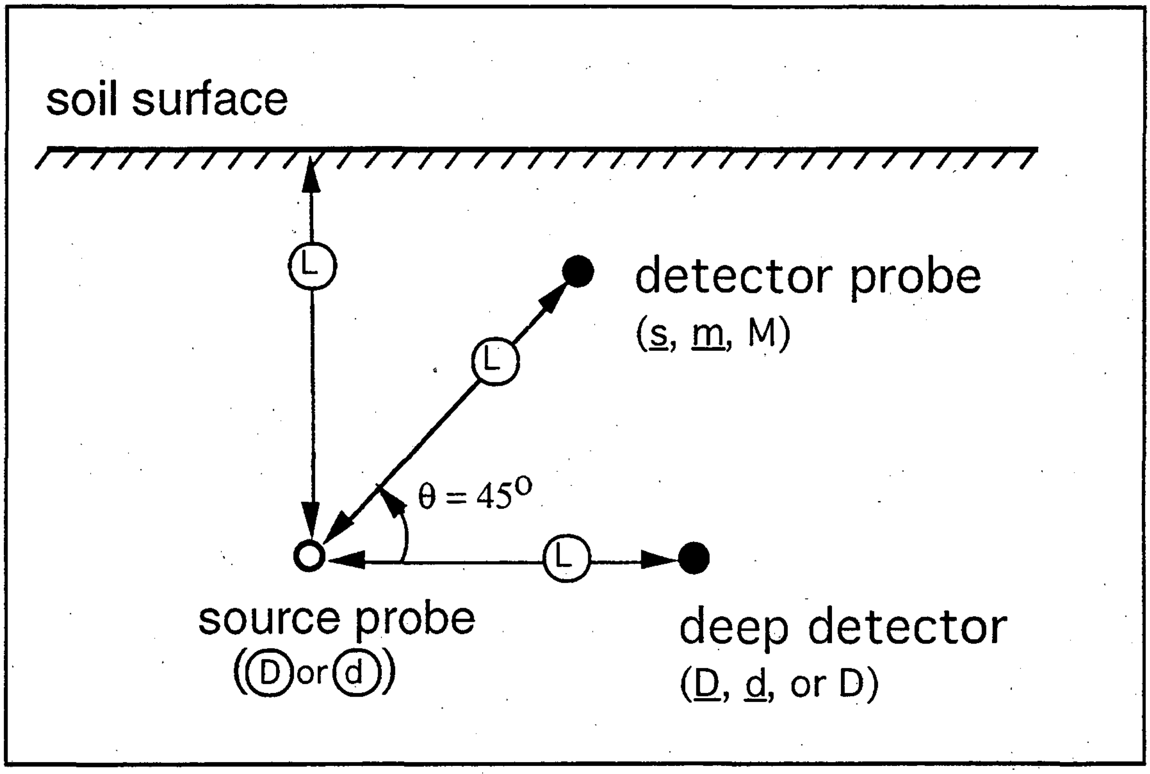

Figure 2. Probe configuration for representative dual-probe dynamic pressure measurements of soil permeability. Probe locations as shown may be used for determining anisotropy of permeability.

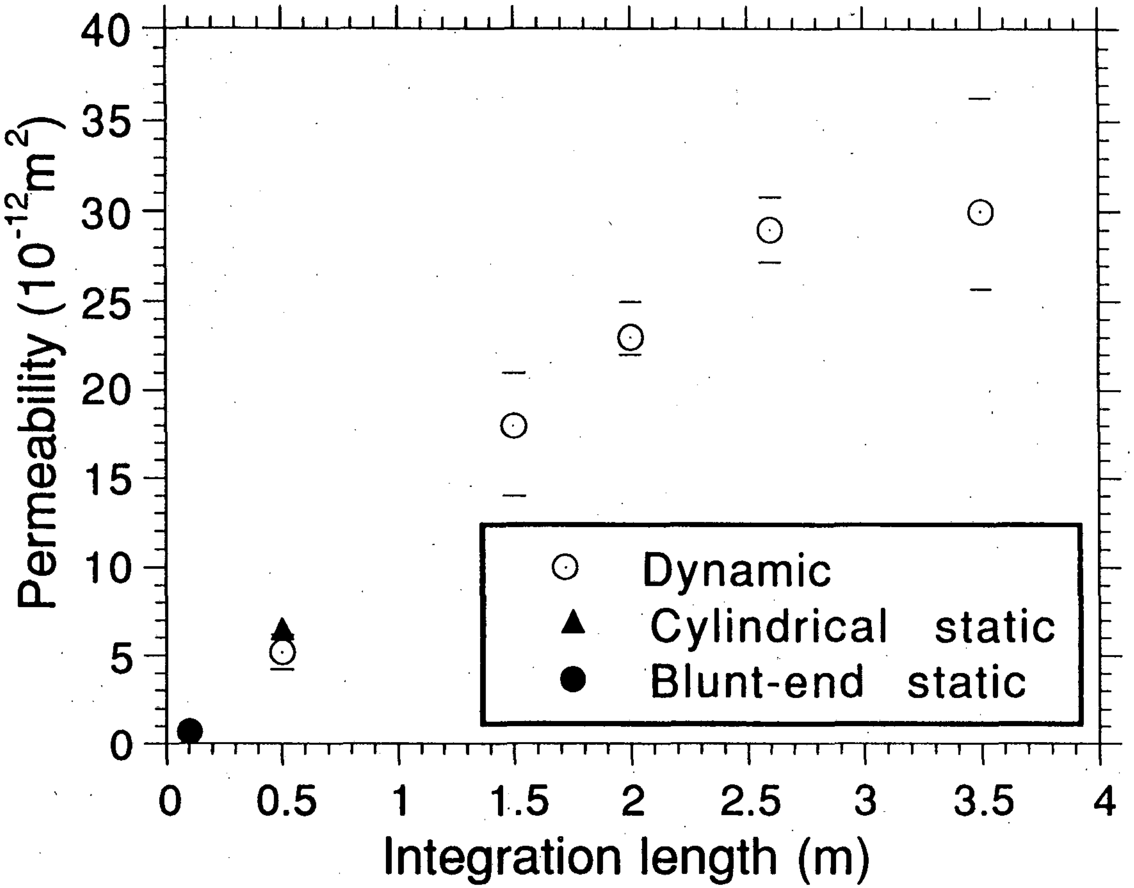

Figure 3. Results of dual-probe dynamic measurements and static measurements made over different integration lengths. The average and full range of values are indicated for the dynamic measurements, unless n=1, in which case, the estimated uncertainty in the individual measurement is indicated. Static measurements are indicated by the weighted geometric mean of 14 blunt-end probe measurements (see Table I) and 22 cylindrical probe measurements. The geometric standard deviation for static measurements is indicated approximately by the size of the symbols.

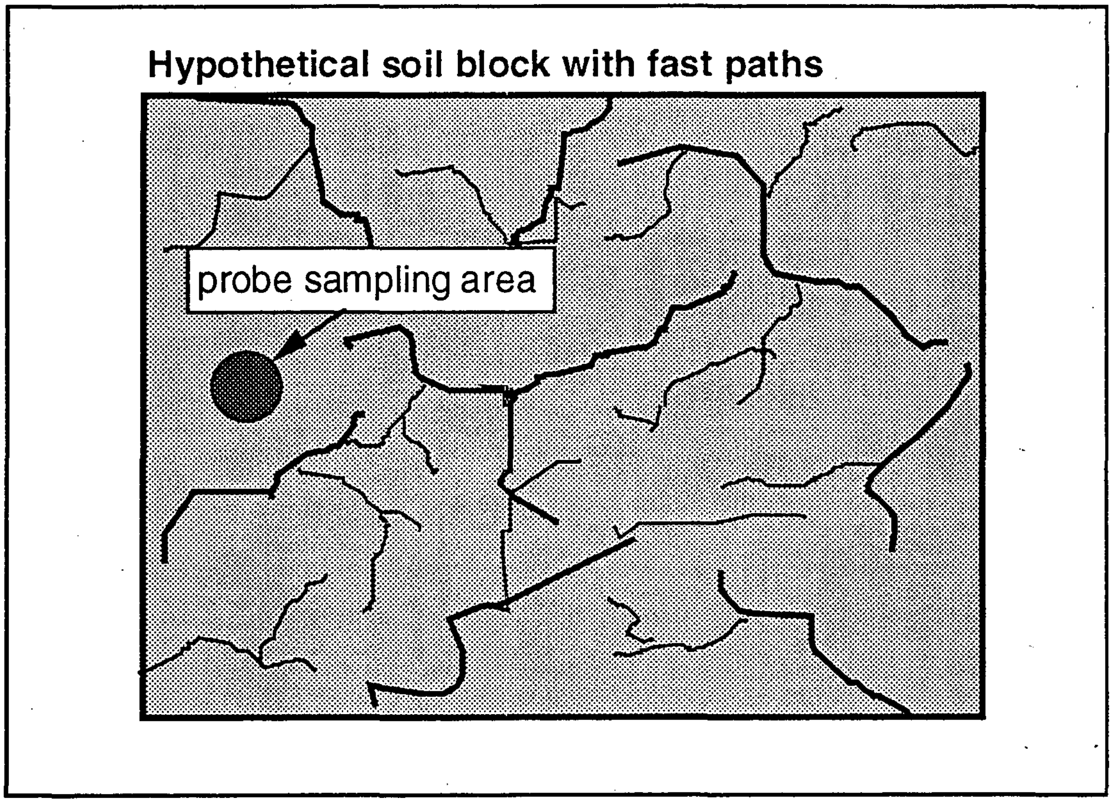

Figure 4. Conceptual model of soil, yielding scale dependent permeability. Network of lines indicates hypothetical fast flow paths that might be caused by the presence of roots, water transport channels, cracks in the soil, or animal burrows.

CHAPTER VI

Resolving the Model-Measurement Discrepancy of Radon and Soil-Gas Entry into the Experimental Structure

SYNOPSIS

This chapter determines the extent to which soil permeability and anisotropy explain the large model-measurement discrepancies in soil-gas entry rate and structure-soil pressure coupling observed at the Ben Lomond experimental basement and reported in Chapter II. In addition, detailed comparisons are made between the modeled and measured radon entry rate and the soil-gas radon concentrations. The three-dimensional radon transport model used in Chapter II was run using both the old and new estimates of soil permeability as inputs, and were compared with the measured soil-gas entry rates. Using the new estimates of soil permeability based on the dual-probe dynamic measurements (taken at the scale at which the structure operates, ~3 m), the model-measurement discrepancy in the soil-gas entry rate is reduced from a factor of ~9 to a factor of 2.5.

The model-measurement comparisons of radon depletion in soil gas substantiate the determination of soil permeability at the several-m scale, as measured by the dynamic measurement technique. Consequently, it appears that our estimates of radon transport through the bulk soil and entry into the structure are probably accurate, as based on the characterization of the soil using the dynamic technique. We hypothesize, therefore, that the remaining discrepancy is due to enhanced soil-gas flow occurring at the soil-structure interface. A fast flow path along the wall would increase coupling at the wall-soil interface, thereby increasing pressure coupling in the adjacent soil. This hypothesis appears to be supported by the remaining discrepancy in the soil pressure field in which much larger pressure coupling is observed adjacent to the wall than is predicted by our model—even when the new description of the soil that includes anisotropy and a low permeability backfill zone is included.

INTRODUCTION

The primary goal of this chapter is to determine the extent to which scale-dependent permeability of soil to air and anisotropy of permeability (Chapter V) explains the model-measurement discrepancies in soil-gas entry rate and soil pressure field observed at the radon transport test facility in Ben Lomond, California (Chapter II). Of particular interest is the extent to which these effects resolve the order-of-magnitude underprediction in the soil gas entry rate. The extent to which the observed anisotropy in permeability explains the larger-than-predicted extension of the pressure field surrounding the structure is also of interest.

As in Chapter II, we use the 3-dimensional finite-difference model of radon transport written by Loureiro *et al.* [1, 2] and modified by Revzan *et al.* [3, 4]. In this case, the model was also modified to include the possibility of anisotropy of soil permeability. Strictly speaking, the finding of scale-dependent permeability implies that models that assume regionally homogeneous soils are inappropriate tools for studying transport in such soils, since homogeneity precludes the possibility of scale-dependent permeability.[1] A homogeneous model will suffice, however, for the purpose of determining the approximate extent to which this effect caused the underprediction of the soil-gas entry rate at the Ben Lomond site. This assertion is justified because the experimental structure, due to its geometry, operates over a relatively limited range of length scales ($\geq \sim 2$ m), a range in which the scale-dependence itself appears to approach a constant value asymptotically (Figure 3, Chapter V).. We know that the structure must operate at scales greater than ~2 m because this is the approximate length of the shortest route from the atmosphere by which air can pass through the soil and

---

[1] This argument assumes that we are using the term *homogeneous* in the usual sense that if the soil were divided into a very fine grid, each grid element would have the same permeability. On the other hand, a statistically *homogeneous* medium might indeed yield scale dependence. Consider for example the nested scales of branched high-flow pathways hypothesized as the cause scale dependence observed in Chapter V. The details of the fine and coarse scaled branching networks might be randomly generated such that each location in the soil has equal probability of having a larger or smaller branch passing through it. On the fine scale, this medium must be considered heterogeneous, but each scale of heterogeneity is itself *statistically* homogeneous.

enter the structure—starting at the soil surface, moving down along the outer wall, going around the footer, and finally entering the gravel layer and then the slots.

A number of points of comparison between the model predictions and measurements are used to evaluate the effect of the new estimations of soil permeability characteristics, and the extent to which they explain earlier model-measurement discrepancies for the Ben Lomond site. These include comparisons between measured and predicted pressure-coupling, soil-gas and radon entry rates, and depletion of radon in the soil gas with structure depressurization.

METHODS

Experimental

As was the case in Chapter II, we use steady-state measurements for comparison with the model simulations. The structure (described in Chapter II) is depressurized by some constant fixed amount relative to atmosphere by regulating exhaust air flow from the structure with a proportional-integral-differential control loop operating in software. Because the half life of ^{222}Rn is 3.82 days, static pressure experiments are run for a week or more so that soil-gas radon concentrations can stabilize.

During these experiments, ^{222}Rn is sampled semi-continuously from the slots through which soil-gas enters the structure and from the air in the structure. Structure air is maintained well mixed by use of an oscillating fan. Slot air is drawn from all six slots simultaneously, delivering a single, mixed sample to the detector. The structure and slots each have a dedicated continuous radon monitor (CRM) to measure concentrations. In addition, radon in soil gas is sampled four times per day from each of 12 soil probes. These samples are multiplexed to one CRM using solenoid valves controlled by the data acquisition software (Genesis, Iconics, Foxborough, Mass.).

The radon data are corrected for the cell background activity due to the slow buildup of ^{210}Pb activity (see Figure 1, Chapter 1, for a schematic of the ^{238}U decay series, which produces ^{222}Rn in soil). This is determined by periodic testing in which the cells are flushed with outdoor air having much lower activity than the cell background. The short-lived daughters are allowed to decay away for more than 3 hrs. The remaining activity, primarily from ^{210}Pb, changes only slowly with time, in accordance with its relatively long half life of 22.3 yr. The backgrounds are then subtracted from the CRM signals.

The CRM data are then analyzed using the method of Busigin *et al.* [5] to account for the contribution of α-decays from the short-lived radon decay products (^{218}Po and ^{214}Po) left in the scintillation cell from previous samples. This correction is required because most radon progeny generated in the cell remain there, adhering to the cell walls. The progeny then contribute α activity according to their concentrations and half lives. The correction is particularly important for the multiplexed probe samples in which the CRM cell sees large and abrupt concentrations changes.

The rate at which radon enters the structure by advection during a given steady depressurization experiment is determined by applying a steady-state mass balance on radon in the structure:

$$(1) \qquad E = R_{in}(Q_{ex} + \lambda V) - S_d$$

where E is the rate of radon entry by advection (Bq/s), R_{in} is the average radon concentration in the structure (Bq/m^3) at time >> 3.82 days after the onset of the experiment, Q_{ex} is the flow rate of exhaust air from the structure (m^3/s), λ is the radioactive decay rate of radon (2.1×10^{-6} s^{-1}), V is the volume of the structure (13.4 m^3), and S_d is the total rate at which radon enters the structure by diffusion. The uncertainty in the estimate of the entry rate is calculated by standard analysis of propagation of error based on the uncertainties in R_{in}, Q_{ex}, V, and S_d. The decay constant is assumed to be known exactly.

There are three possible sources of diffusive entry of radon into the structure: radon from the decay of radium in the concrete of the walls and floors, radon originating in the soil that diffuses through the walls and floor, and radon diffusing through the slots in the floor. The contributions from each of these sources are calculated in the appendix to this chapter. Their sum determines S_d.

Numerical Modeling

The three-dimensional finite-difference model used in Chapter II was also used here to simulate the steady depressurization experiments at the Ben Lomond experimental basement. Briefly, recall that the model simulates radon transport through soil by advection and diffusion. The model assumes that the structure can be simulated by specifying the geometry of only one-quarter of the structure and the soil block (from the mid-lines of the structure outward in the horizontal directions). The full solution for the radon and soil-gas entry rates is obtained by multiplying the fluxes calculated for the block by a factor of four.

The model was modified for the current study to account for horizontal-vertical anisotropy of soil permeability to air. This was achieved in the usual fashion by specifying permeability as a 3 x 3 tensor (see, for example, [6]). We consider only the possibility of anisotropy aligned with the horizontal and vertical axes, so that the off-diagonal elements in the permeability tensor are taken to be zero.

To determine the approximate extent to which the anisotropy and scaling of soil permeability observed in Chapter V explains the model-measurement discrepancy found in Chapter II, we run the model, given the geometry of the structure and gravel, but varying the soil permeability configurations. Other soil parameters are held constant at the values given in Table I and taken from Chapter II and Refs. [7, 8]. Table I also defines the depths of 4 soil layers possessing different characteristics and indicates the location of the backfill zone that was excavated for installation of the structure and was mechanically repacked later. In addition to those variable soil parameters listed in Table I, the radium concentration in the soil was set at 33 ± 6 Bq/kg throughout the soil, as determined from measurements by Flexser *et al.* [7]. Literature values of the effective radon-diffusion coefficient in soil are compiled in [9]. A value of 1.0 $\times 10^{-6}$ m^2/s was used for the modeling.

To determine the effect of the soil permeability field on predictions of the soil-gas and radon entry rates, the radon concentration field, and the pressure-field in the soil, we consider 4 possible permeability configurations, designated Cases 1 - 4. These are summarized in Table II.

Case 1 is similar to the modeling in Chapter II, with the soil divided into homogeneous and isotropic regions as shown in Figure 1. The permeability of each region is estimated from the arithmetic means of the cylindrical-probe permeability measurements made in each region. The soil characterization differs from that in Chapter II in the details of the determination of the permeability for the bulk soil (layers 2 -4). In Chapter II probes for which permeability data were not available were neglected from the average (see Chapter 2, Table II, notes 'a' and 'b' of the table). Subsequent inspection of long-term data (seasonal variations) acquired at those probes indicated that the lack of 'availability' of data was a result of permeabilities at those probes falling below the detection limit, rather than due to a measurement error. Therefore, the estimate of average permeability of the bulk soil in Chapter II was somewhat high. In the current analysis, those probes are assigned a permeability at the detection limit. This reduces the new upper estimate of average soil permeability.

Case 2 is a simplification of Case 1 in which the entire soil (other than the gravel) is assigned a homogeneous isotropic permeability determined by the arithmetic mean of all cylindrical-probe permeability measurements.

Case 3 assumes homogeneous, anisotropic soil with values determined from the dual-probe dynamic permeability measurements in Chapter V. Permeability is selected for a length scale of 3+ m.

Case 4 is identical to Case 3 except that the backfill region is treated separately. In this case it is assumed that, since the soil in that region had been excavated, extensively handled, and repacked by compression, at the time that the structures were built, the soil there might not have developed the structure that causes scale dependence. (Recall that we hypothesize in Chapter V that scale dependence is due to the presence of roots and possible animal burrows, and water leaching channels.) In that case the backfill permeability might be more accurately determined by the smaller-scale cylindrical measurements, and consequently be lower than that of the surrounding soil.

We are forced to take the approach of modeling both Cases 3 and 4 rather than simply measuring scale dependence in the backfill zone because of current limitations of the mathematical model used to analyze the field data. That model accounts for two boundary conditions only: that specifying the dynamic pressure at the probe, and that specifying the constant zero disturbance pressure at the soil surface (see Chapter III). Because of the proximity of the structure wall for measurements made in the backfill zone, an additional boundary condition would be required—a no-flow condition at the wall.[2] We plan to modify the model to account for that condition in the future.

Note that the arithmetic mean permeability is used in Cases 1 and 2 rather than the geometric mean. This is for consistency with the work in Chapter II.

---

[2] An added complication would occur if flow were enhanced at the soil-wall interface due to the presence of a localized high permeability region where the two materials meet. It would probably be impossible to model that case analytically.

The effect of selecting the geometric, rather than the arithmetic mean is discussed in the next section.

The model assumes that the ^{226}Ra source concentration is homogeneously distributed throughout the soil. To determine the soil-gas radon concentration field that results from transport of radon by advection (from pressure-driven flow), the pressure field resulting from structure depressurization, and the resulting soil-gas velocity field is first calculated. In practice, the predicted soil-gas radon concentration field is then normalized with respect to the measured deep-soil radon concentration in order to compare the measured and modeled values. This is discussed further in the next section. Transport by diffusion is also included in the model.

RESULTS

The effect of the soil-permeability characteristics on the soil-gas entry rate is explored by comparing the predictions of the four model cases with the entry rate measured during a steady 21 Pa depressurization experiment. The results are shown in Table III, below. The new assumptions about soil permeability increase the predicted soil-gas entry rate by about a factor of four, considerably reducing, but not eliminating, the discrepancy reported in Chapter II.

If the weighted geometric mean (GM) permeability is used instead of the arithmetic mean in Case 2, the bulk permeability is estimated at 2.7×10^{-12} m^2. Therefore, the soil-gas entry prediction using the GM would be even lower than for the arithmetic mean (AM) ($\sim 2 \times 10^{-5}$ m^3/s), increasing the model-measurement discrepancy in the soil-gas entry rate. Thus, it is not our choice of probability distribution for the permeability field that is causing the model-measurement discrepancy in the soil-gas entry rate. Since, if we had used the GM instead of the AM for the static-measurement estimate of regional soil permeability, the original value of the model-measurement discrepancy would have been even higher. That is, the correction would go in the wrong direction!

Figure 2 shows the modeled and measured radon entry rates for the Ben Lomond west structure. The model predictions are for the old and new homogeneous soil estimates of soil permeability (Cases 2 and 3). Also shown are 'measured' radon-entry rates inferred from radon mass balance using Eq. 1. As expected from the remaining model-measurement discrepancy in the *soil-gas* *entry rates*, the new estimates of soil-permeability characteristics considerably reduce but do not eliminate model underprediction of the *radon entry rate* at the Ben Lomond west structure. At 65 Pa depressurization, the measured entry rate is ~1.5 times higher than the model-predicted rate based on the dual-probe dynamic measurements of soil permeability. A considerable improvement has been realized relative to the factor of 7 overprediction based on the single-probe static estimates of soil-permeability.

Unlike the soil-gas entry vs. depressurization curve (Figure 5, Chapter II), the advective radon-entry vs. depressurization curve (Figure 2) is not linear. Instead, the slope decreases at higher pressures. This result is explained as follows: As structure depressurization increases, the flow of dilution air from the soil surface, through the soil, and into the structure also increases. If flow rates are high enough so that the transit time for a packet of air moving from the surface to a given point in the soil is significantly less than the half life of ^{222}Rn, then the radon concentration in the soil at that point will be lower than during non-advective conditions. We refer to this phenomenon as *soil-gas radon depletion*. It is quantified as the ratio of the concentration at a given point when both advection and diffusion are active to the concentration when advection is absent.

The amount of depletion at a given point in the soil, for a given structure pressure, depends only on the effective soil permeability of the path that the air follows from the surface through the soil. Therefore, the measured soil-gas radon depletion can be used as an *independent* check of soil permeability, either verifying or refuting the permeability estimates of the dual-probe dynamic pressure technique. This phenomenon has been modeled for a simple geometry by Nazaroff [10]. Unfortunately, that model cannot be used to simulate radon entry into the Ben Lomond west structure because of the presence of the sub-slab gravel layer.

The difference in depletion estimates resulting from different assumptions about soil permeability are not immediately obvious from a comparison of soil-gas radon concentrations given only one value of structure depressurization. Figures 3a and 3b show a comparison of measured radon concentrations vs. model predictions for Cases 2 and 3. The measured radon concentrations are normalized with respect to the concentration measured in the 2.4-m long probe that penetrates the structure floor. That point was selected to have a concentration of 0.89 times the concentration at infinite depth in soil at a depressurization of 21 Pa, bracketing the predictions of the model for Cases 2 and 3 of 0.88 and 0.90, respectively. The need to calibrate the model to the data in this fashion is an obvious drawback of this kind of comparison. From the multi-point comparisons it is not clearly obvious that one model or the other best fits the experimental evidence.

On the other hand, if we compare measured and modeled concentrations over a *range* of depressurizations, we find a very clear basis upon which to judge the selection of model inputs. The model is run given the old and new estimates of soil permeability and anisotropy (Cases 2 and 3) over a range of structure depressurizations from 0 - 60 Pa. To determine the effect that a lower permeability back-fill zone might have on soil-gas radon concentrations, we also model soil-gas radon depletion for Case 4. The predicted soil-gas radon concentrations curves are then compared with measurements of soil-gas radon concentrations made over the same range of conditions for a number of locations in the soil.

For the purpose of the soil-gas radon depletion comparison, radon concentrations are normalized with respect to their initial concentrations under neutral pressure conditions. This procedure eliminates any confounding error due to uncertainty in the diffusion coefficient for radon in soil and allows us to assess the effect of advection alone. Figures 4a - d show the model-measurement comparisons for four probe locations in the mid- and low-wall levels of the soil: at a short, medium, or long probe on each side of the structure. These probes were chosen for several reasons: (1) the variety of their locations, (2) the fact that they are in locations where significant depletion might be expected to occur, and (3) because their depth below surface ensures that we are observing an effect due to transport over a reasonably long path length. Incidentally, reason (3) also ensures a signal which is relatively undisturbed by seasonal changes in soil conditions. The concentration data in Figure 4a - d are from 10 experiments run over a 1.3-year period at the steady pressures indicated in Table IV. Figures 4a - d show clearly that the description of soil permeability based on the larger-scale dynamic measurements gives a considerably better fit to the data than that based on the smaller-scale cylindrical probe measurements.[3]

---

[3] Note, in all four cases depletion occurs somewhat faster than predicted by the model at depressurization below ~20Pa, and it occurs somewhat slower than expected at larger depressurization. The source of this disagreement is not clear. Its existence makes it difficult to

Despite the somewhat different shapes of the modeled and measured depletion curves, the data clearly favor the higher permeability description of the soil. Based on Figures 4a and 4b, for probes in the natural soil, there is little distinction between Cases 3 and 4, indicating that the nature of the backfill zone has relatively little effect on probes in the natural soil. On the other hand, for probes in the backfill zone a clear distinction can be made between Cases 3 and 4, as illustrated in Figures 4c and 4d. That is, the soil-gas radon concentrations in the backfill zone itself depend strongly on the permeability of the backfill zone. In Figure 4c, Case 4 clearly gives a better fit to the data, suggesting that the permeability of the mechanically packed soil is indeed lower than that of the natural soil, resulting in reduced advective flow and therefore reduced dilution of radon in soil-gas in that region.

Figure 4d is somewhat ambiguous in that regard, giving a reasonable fit with Case 3 at low pressures and Case 4 at higher pressures. Despite this ambiguity, it is clear that the measured depletion in the backfill zone, even in Figure 4d, is smaller, relative to Case 3 (the high permeability homogeneous model) than is the case for probes in the natural soil. In other words, although the radon depletion data do not provide an unambiguous best fit to the data, we can say that the permeability in the backfill zone appears to be lower than in the natural soil. This finding is consistent with our hypothesis that scale dependence of permeability results from natural processes such as root growth, animal burrowing, and the creation of water leaching channels, which enhance the otherwise lower permeability of the soil matrix.

The final model-measurement comparison that we will consider is that of pressure coupling between the structure and points in the surrounding soil (see Chapter II for definition of pressure coupling). Figure 5 shows a comparison for pressure coupling predicted by Cases 2 and 3 of the model and pressure coupling measured during the 21 Pa depressurization experiments reported in Chapter II (experiment BLW079, Table IV).

---

determine with certainty what the "correct" soil permeability should be to give a best fit to the data (*i.e.,* whether we should be fitting to the low pressure data or the higher pressure data). There does not appear to be a correlation between deviation from the modeled depletion curve and time of year, so it is unlikely that changes in soil conditions are responsible for the shape of the measured depletion curve.

Key observations result from this comparison. First, there is very little difference between the model predictions of Cases 2 and 3. Second, the measured coupling significantly exceeds the model predictions, especially in relative magnitude in the mid- and low-wall level probes. Because of the relatively large uncertainties in measurements in the near-surface probes we do not place much importance on the magnitude of the discrepancy in that region. A comparison of Cases 2 and 3 indicates that although the anisotropy of Case 3 does indeed increase the magnitude of pressure coupling predictions in the far-field (long probes) soil relative to near-field (short probes), the effect is only slight, and does not explain the factor of 2 to 3 larger values observed in the mid- and low-wall level probes.

Case 4 was also run to determine the pressure coupling in the soil because it was thought that a low-permeability backfill zone might contribute to an increase in coupling in the far-field soil. However, even the inclusion of a low-permeability backfill zone does little to increase the far field pressure coupling. In Case 4 the pressure coupling in the long low-wall probe on the north side of the structure is predicted to be 4.8% instead of 4.6% for Case 3, and the pressure coupling in the short low-wall probe is 9.1% instead of 7.7%. These are the largest fractional changes in estimated coupling for the two cases, and are not significant relative to the model-measurement discrepancy.

DISCUSSION

The model-measurement comparisons of radon entry rate and of radon depletion in soil gas give us greater insight into the nature of radon transport through the soil and into the possible causes of the remaining model-measurement discrepancy in the radon entry rate. The model-measurement comparisons of the soil-gas radon depletion curves confirm the findings of Chapter V, that the small-scale measurements of soil-permeability systematically and significantly underestimate the effective permeability of the soil at larger scales. The radon depletion data indicate that effective soil permeability, on the scale sampled by the Ben Lomond experimental basement, is at least as large as that determined by the dual-probe dynamic permeability measurements at the 3+ m scale. These findings justify confidence that our estimates of radon transport through the bulk soil, and resulting entry into the structure are fairly accurate. Yet, the model-measurement comparisons of the radon and soil-gas entry rates indicate that there is more radon entering the structure than can be accounted for by bulk flow through the soil alone.

Taken together, these facts support our hypothesis that the source of the missing soil-gas and radon entering the structure is enhanced flow occurring along the soil-structure interface—a possibility not accommodated in the current configuration of the model. The remaining discrepancy in the soil pressure field also appears to support this hypothesis. The new description of the soil-permeability field was not sufficient to explain the large pressure coupling observed in the soil adjacent to the structure. If, however, a fast path does exist next to the wall, then the pressure gradient in that region would be more nearly linear than expected if the soil-structure interface were a perfect discontinuity. This path would increase coupling along the wall and in the adjacent soil. (See Ref. [4] for a discussion of the effect of a high-flow path at a structure-soil interface.)

CONCLUSIONS

The results presented in this chapter further support the conclusion of Chapter V, that misinterpretation of the effective permeability of the bulk soil due to the presence of scale-dependent soil permeability, accounts for a majority of the model-measurement discrepancy in radon entry rate measured and predicted for the Ben Lomond test structure (Chapter 2). Comparison of measured and modeled soil-gas radon depletion with structure depressurization provides an independent check of the dual-probe dynamic estimates of soil permeability at the 3+ m scale. In particular, the radon depletion confirmation indicates that, despite the fact that the dynamic technique provides only an indirect measurement of permeability through a direct measurement of pressure diffusivity ($D_p = kP_a / \varepsilon\mu$), the interpretation of the results in terms of permeabilities are correct. That is, the results are *not* confounded by potential scale or frequency dependence of the porosity parameter (μ).

Despite great improvement in the model predictions of the radon and soil gas entry rates, a significant discrepancy remains. The new description soil permeability reduced the model-measurement discrepancy in the radon entry rate from a factor of ~7 to a factor of about ~1.5. Because the description of radon transport in the bulk soil appears to be approximately correct, we hypothesize that the remaining discrepancy is due to a fast flow path at the structure-soil interface. This hypothesis is supported by observations of the soil pressure field that indicate significantly (factor or 2 - 3) higher pressure coupling in probes adjacent to the structure walls than is predicted by the model—even using the new description of the soil permeability field that includes anisotropy and a low permeability backfill zone. Experiments are planned for the future that will sample soil gas from the interface to determine if flow is enhanced (and radon concentrations therefore reduced) in this region.

Measurements of radon concentration in soil gas in the region of soil that was excavated and repacked after structure depressurization indicate that this region has lower soil permeability than the surrounding soil. This finding provides further support for our hypothesis that the scale dependence of soil permeability results from natural processes such as the growth of roots, animal burrowing, and the movement of water through soil. In the backfill region, these structures have not had time to become fully developed because of the relatively recent disturbance of the soil.

In summary, this work reinforces our earlier conclusions that assessment of soil transport characteristics, typically based on multiple small-scale measurements, can produce serious underestimates of actual transport in systems that function at larger scales. The magnitude of this error argues that it is important to study this effect in other soils to determine its prevalence and causes.

REFERENCES

1. Loureiro, C.O., Abriola, L.M., Martin, J.E. and Sextro, R.G., Environmental Science and Technology, 1990, 24: 1338-1348.

2. Loureiro, C.O., *Simulation of the Steady-State Transport of Radon from Soil into Houses with Basements under Constant Negative Pressure.* LBL-24378, Lawrence Berkeley Laboratory, Berkeley, CA: 1987.

3. Revzan, K.L., Fisk, W.J. and Gadgil, A.J., Modeling radon entry into houses with basements: Model description and verification, *Indoor Air,* 1991, 1: 173-189.

4. Revzan, K. and Fisk, W., Modeling radon entry into houses with basements: The influence of structural factors, *Indoor Air,* 1992, 2: 40-48.

5. Busigin, A., van der Vooren, A.W. and Phillips, C.R., Interpretation of the response of continuous radon monitors to transient radon concentrations, *Health Physics,* 1979, 37: 659-667.

6. de Marsily, G., *Quantitative Hydrogeology,* Academic Press, Inc.: New York, 1986.

7. Flexser, S., Wollenberg, H.A. and Smith, A.R., *Distribution of Radon Sources and Effects on Radon Emanation in Granitic Soil at Ben Lomond, California.* LBL-31915, Lawrence Berkeley Laboratory, Berkeley, CA: 1992.

8. Brimhall, G.H. and Lewis, C.J., *Differential Element Transport in the Soil Profile at the Ben Lomond Small Structure Radon Site: A Geochemical Mass Balance Study.* Department of Geology and Geophysics, University of California, Berkeley: 1992.

9. Nazaroff, W.W., Moed, B.A. and Sextro, R.G., Soil as a source of indoor radon: Generation, migration, and entry. In: *Radon and Its Decay Products in Indoor Air*, Nazaroff, W. W. and Nero, A. V. J., Ed. John Wiley and Sons: New York, 1988, 57-112.

10. Nazaroff, W.W., Predicting the rate of ^{222}Rn entry from soil into the basement of a dwelling due to pressure-driven air flow, *Radiation Protection Dosimetry*, 1988, 24: 199-202.

Table I. Soil characteristics assigned to different regions in the soil.

soil depths[a] [m]	soil layers[b]	backfill regions[b]	emanation fraction[c]	air-filled porosity[d]	bulk density[e] [10^3 kg/m^3]
0.00 - 0.52	layer 1	upper backfill	0.31 ± 0.02	0.45 ± 0.05	1.4 ± 0.1
0.52 - 1.40	layer 2		0.31 ± 0.02	0.45 ± 0.05	1.4± 0.1
1.40 - 2.25	layer 3	lower backfill[f]	0.45 ± 0.04	0.45 ± 0.05	1.4± 0.1
2.25 - 13.0	layer 4		0.31 ± 0.02	0.25 ± 0.15	1.9± 0.5

[a] The ranges indicate the top and bottom depths of the different regions of soil indicated in the fourth and fifth columns of the table. (Note exception in note f to this table.)

[b] The location of the different soil regions are shown in Figure 1.

[c] Fraction of ^{222}Rn generated in the soil that is left in the pore space after it is created by decay from ^{226}Ra. Data from Flexser et al. [7].

[d] Data on non-solid porosity from [8] combined with soil-moisture data from Chapter 2 to determine air-filled porosity.

[e] Data from [8].

[f] Backfill region actually terminates at about the level of the bottom of the slab (~1.9 m), but it is assigned the soil characteristics of the layer 3 soil.

Table II. Soil permeability configurations for different model runs.

Region of soil		**Permeabilities[d] (10^{-12} m^2)**
Case 1[a]		
upper backfill		2.6
lower backfill		5.2
layer 1 soil	(non-backfill)	7.7
layer 2 - 4 soil	(non-backfill)	6.3
Case 2[b]		
all soil except gravel		5.4
Case 3		
vertical	(all soil)	18.
horizontal	(all soil)	30.
Case 4[c]		
vertical	(all soil)	18.
horizontal	(all soil)	30.
backfill		3.5

[a] Locations of soil regions are shown in Figure 1.

[b] This case uses an average permeability that includes natural soil and the backfill region. The calculated value is the arithmetic mean of all cylindrical-probe permeability measurements made in the soil around the west structure (using the detection limit value for those probes with permeabilities below the detection limit). This value differs from the mean permeability of cylindrical probes measurements listed in Table I, Chapter V. Different probes were used for that case because we wanted to compare dynamic permeability measurements with probes in the immediate vicinity, and only in the natural soil. Therefore, in that case, the backfill and subslab probes were excluded.

[c] Backfill region here includes upper and lower backfill as indicated in Figure 1.

[d] Arithmetic mean of cylindrical probe measurements of soil permeabilities for different regions of the soil.

Table III. Soil-gas entry rates measured and modeled given different assumptions about soil permeability characteristics.

Measurement or Model Run	Soil-gas entry rate [10^{-5} m^3/s]	Ratio of measured to modeled entry rates
measurement (-20 Pa)	35. ± 10	
Case 1	4.0	8.8
Case 2	3.5	10.
Case 3	14.	2.5
Case 4	14.	2.5

Table IV. Static depressurization experiments used to determine the soil-radon concentrations indicated in Figures 4a - d.

Experiment ID	Starting date of experiment	Structure depressurization [Pa]
BLW085	11/22/91	0
BLW044	9/1/90	0
BLW099	4/17/92	9
BLW068	5/15/91	18
BLW072	6/14/91	18
BLW079	9/19/91	21
BLW029	8/1/90	24
BLW033	8/15/90	46
BLW030	8/8/90	65
BLW087	12/11/91	65

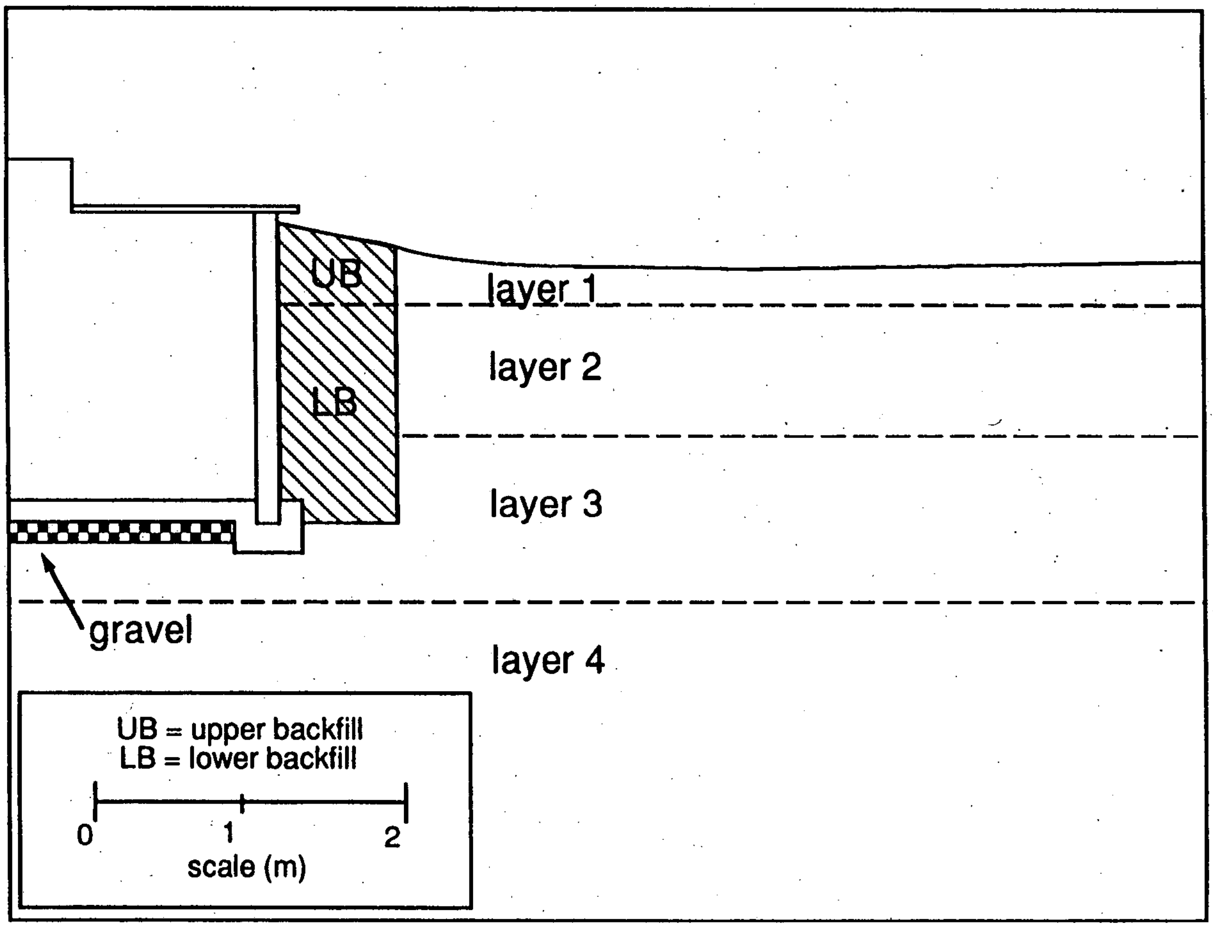

Figure 1. Soil regions used for modeling soil-gas and radon entry into the structure. The figure shows a vertical cross section of the soil from the middle of the struc ture outward into the soil. Symmetry is assumed about the mid-line.

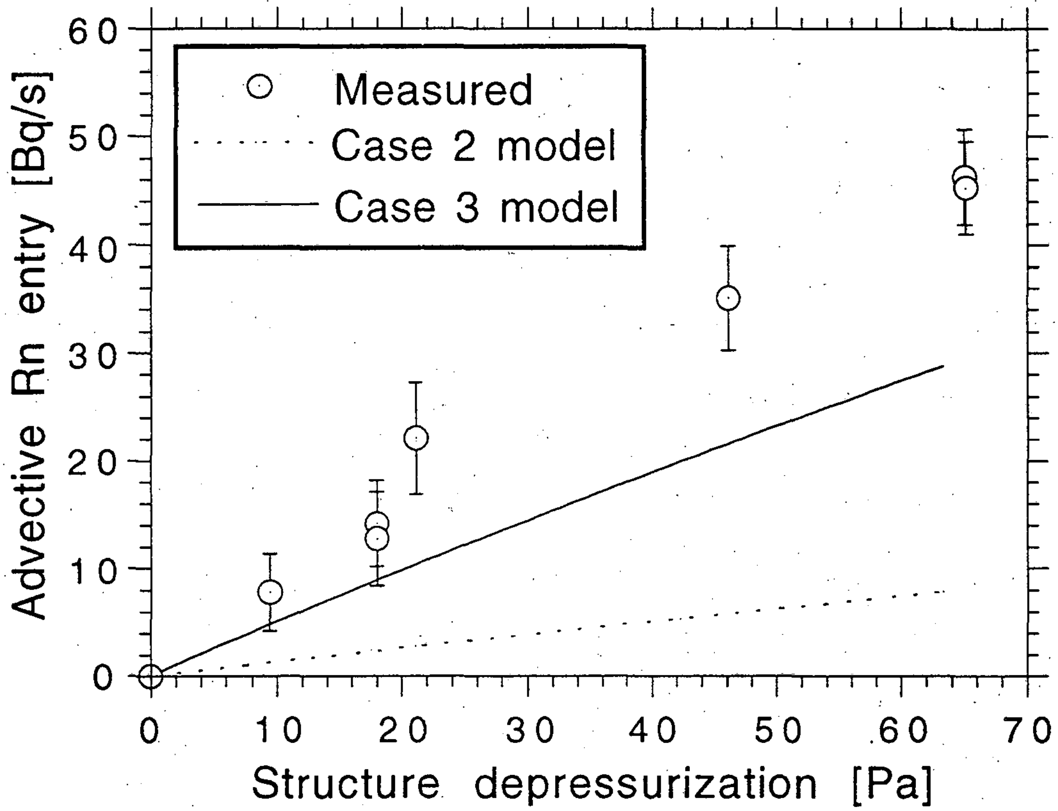

Figure 2. Radon entry rates vs. structure depressurization: model-measurement comparison. The soil permeability configurations used in the model runs are described in Table II. Case 2 uses as input a homogeneous soil permeability determined from the arithmetic mean of the cylindrical-probe static permeability measurements. Case 3 uses a homogeneous and anisotropic permeability field determined from the dual-probe dynamic permeability measurements at a scale of 3+ m.

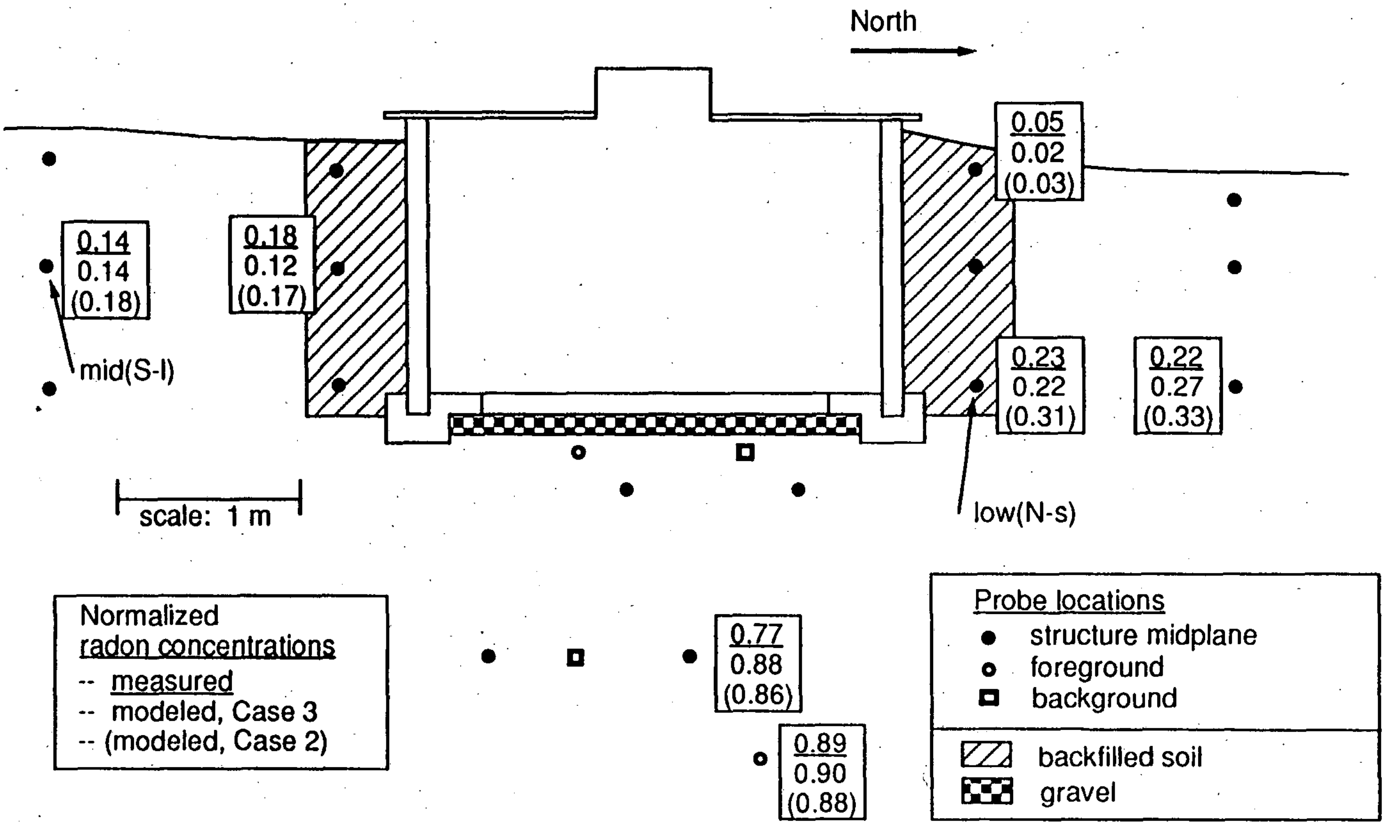

Figure 3a. North/south cross section of the site showing measured and predicted radon concentrations, normalized with respect to the concentration measured in the deepest soil probe. Measured concentrations are the average of values obtained in three experiments run at -18, -21, and -23 Pa. The model was run at 21-Pa depressurization given the two different assessments of soil permeability represented by Cases 3 and 2, Table II. Individual probes are identified that were used for model-measurement comparisons of soil-radon depletion in Figures 4b and 4d.

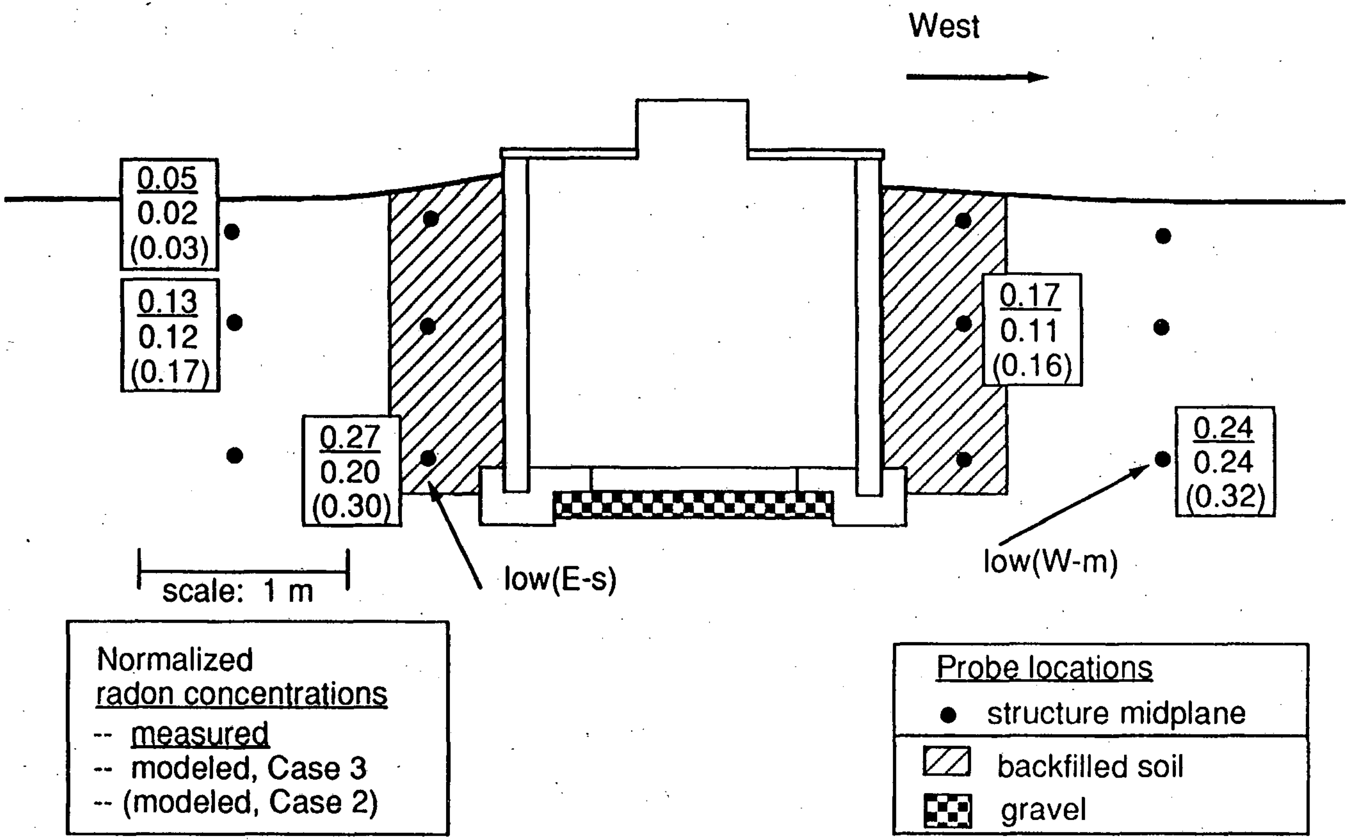

Figure 3b. East/west cross section of the site showing measured and predicted radon concentrations, normalized with respect to the concentration measured in the deepest probe. Individual probes are identified that were used for model-measurement comparisons of soil-radon depletion in Figures 4a and 4c.

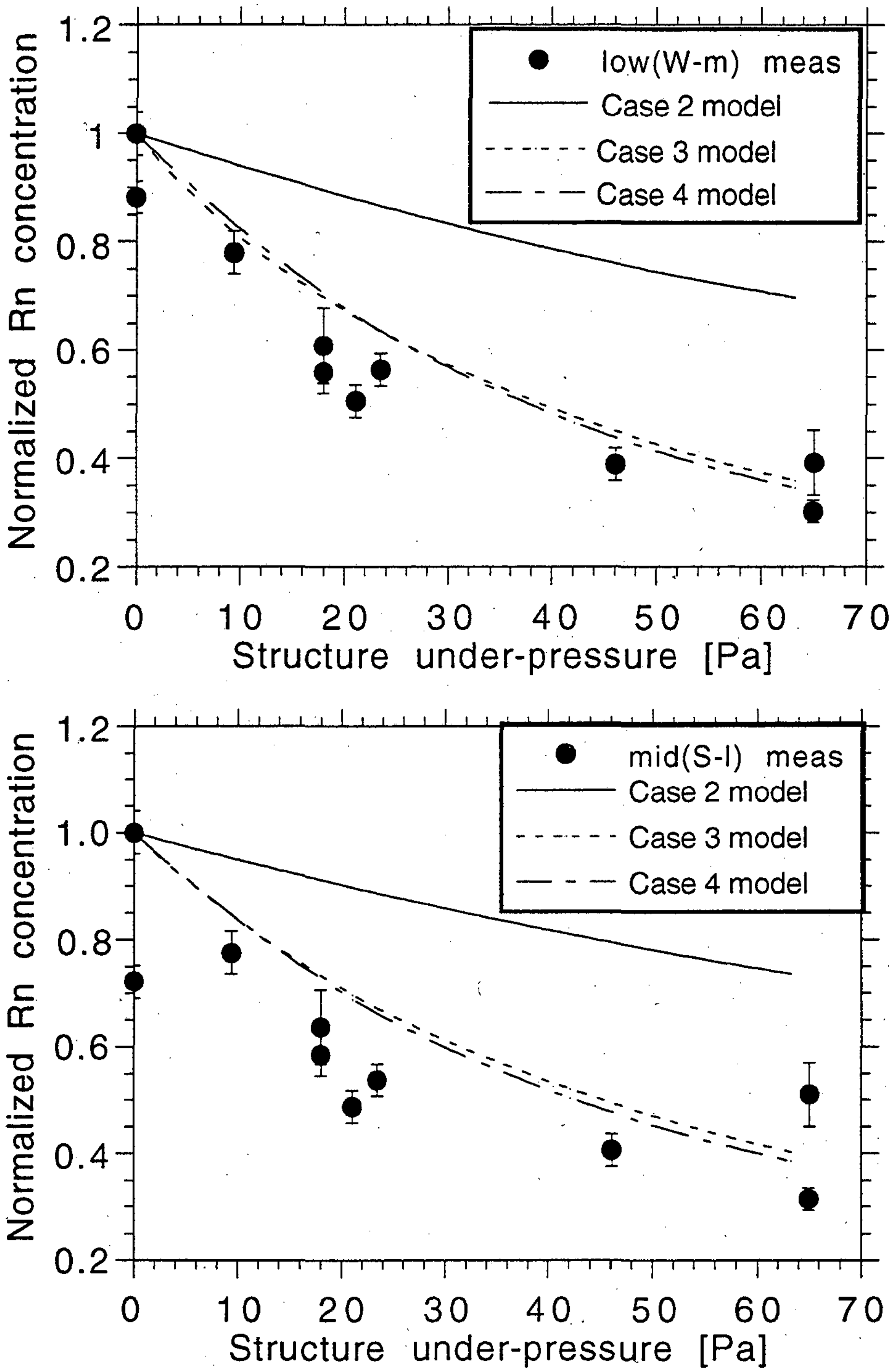

Figures 4a (top) and 4b (bottom). Model-measurement comparison of soil-gas radon depletion with structure depressurization. Model case descriptions are found in Table II. Measurements are for probe locations low(W-m), a medium length probe located at low-wall level on the west side of the structure, and mid(S-l), a long probe located at mid-wall level on the south side.

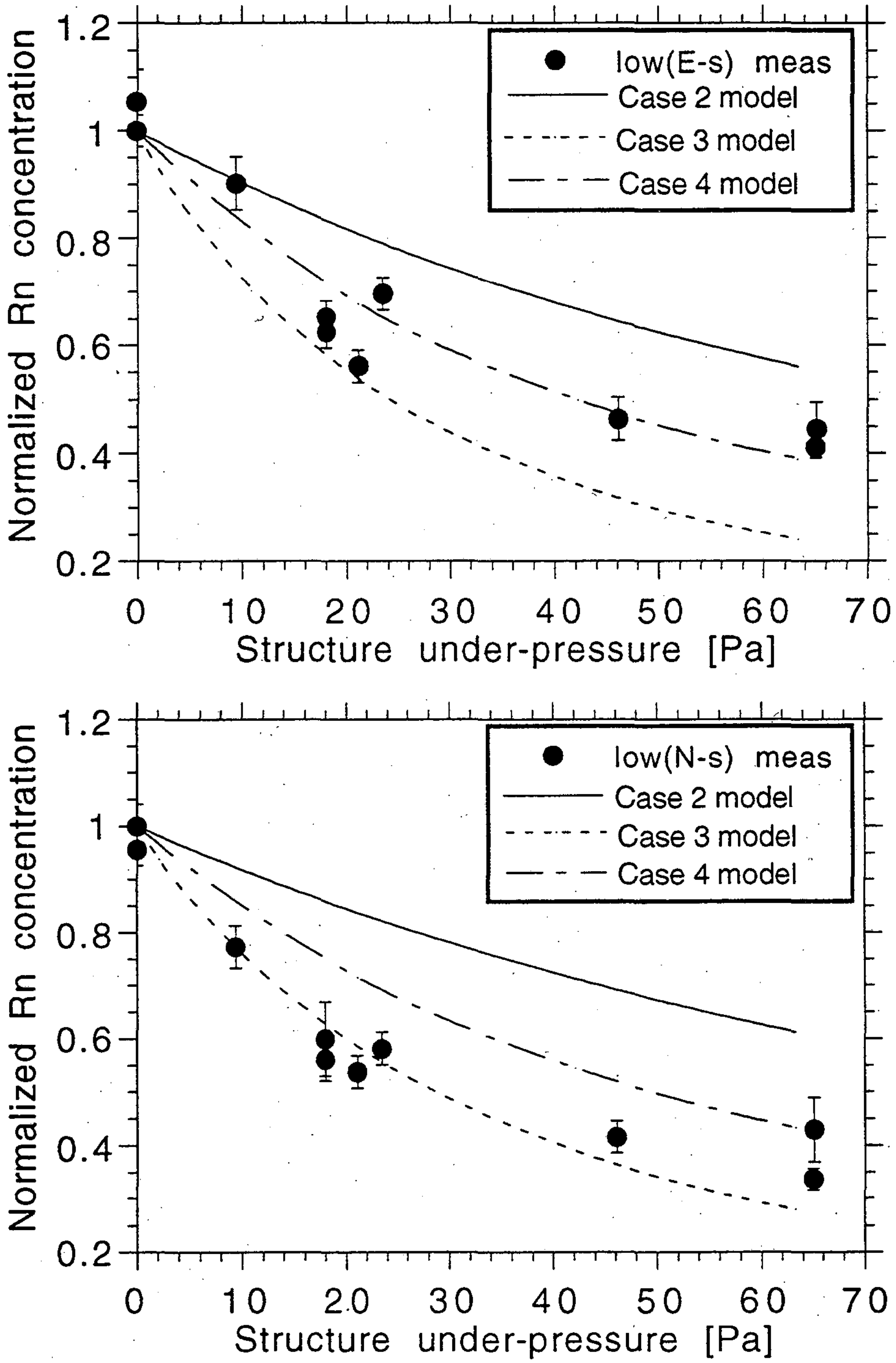

Figures 4c (top) and 4d (bottom). Model-measurement comparison of soil-gas radon depletion with structure depressurization. Model case descriptions are found in Table II. Measurements are for probe locations low(E-s) and low(N-s), short probes located in low-wall-level soil on the east and north sides of the structure, respectively.

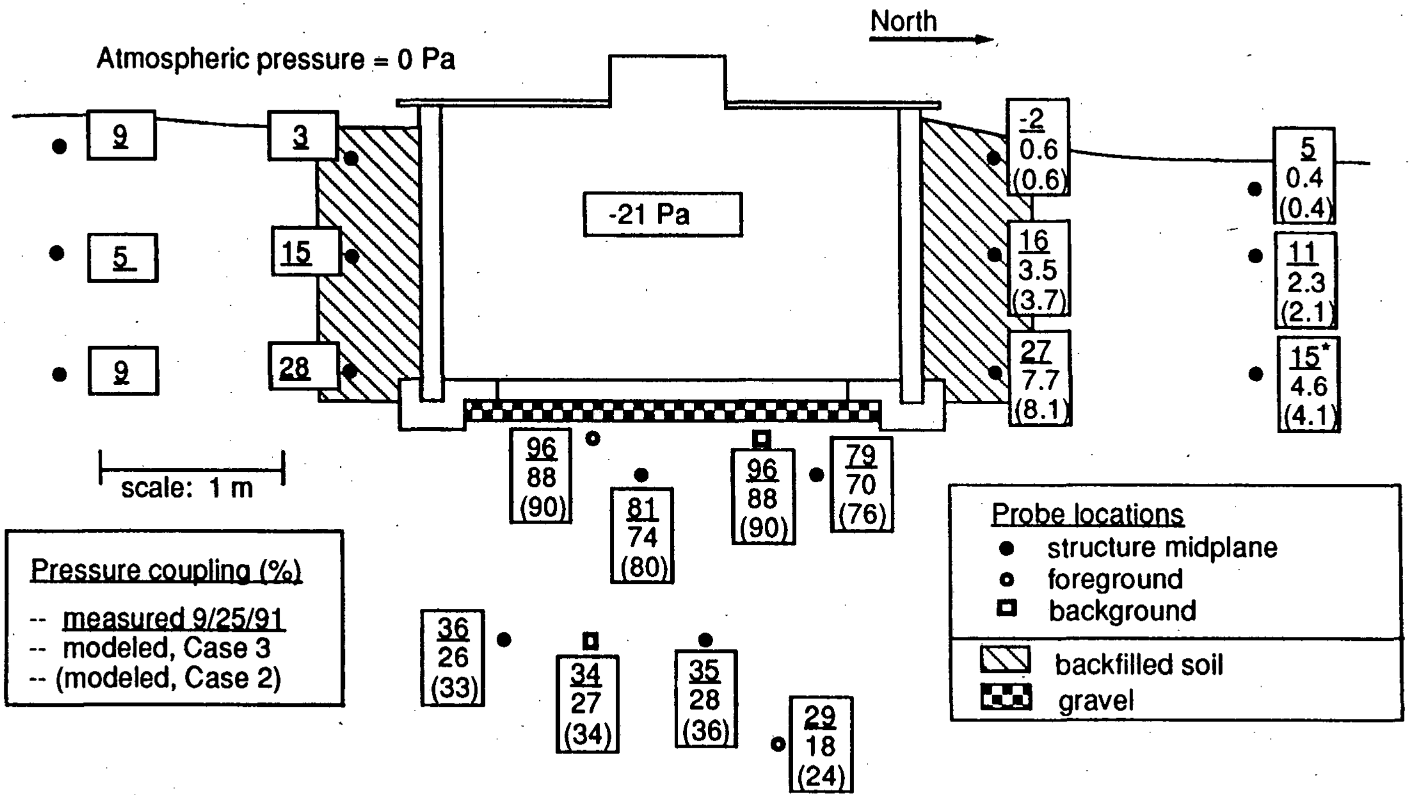

Figure 5. North/south cross section of the site showing measured and predicted pressure coupling at the indicated probe locations. Measured values are from an experiment carried out on September 25, 1991 at 21-Pa structure depressurization. The one measurement marked with an asterisk is from an experiment run at -18 Pa carried out on May 15, 1991. The model was run at 21-Pa depressurization given the two different assessments of soil permeability represented by Cases 3 and 2, Table II. The measured values have an uncertainty of ± 4%. Model predictions for the south side are identical to model predictions for the north side.

APPENDIX

Diffusion as a Source of ^{222}Rn in the Ben Lomond West Structure

INTRODUCTION

^{222}Rn may enter the structure by diffusion from several different sources and pathways. Radon originating from decay of ^{226}Ra in the concrete walls and floor may diffuse from the concrete into the structure. Radon originating in the soil may diffuse through the walls and floor or through the open slots during an advection experiment. This appendix describes measurements used to determine the contributions to ^{222}Rn concentration in the structure from these different sources. These estimations are applied in the radon mass balance estimates of the soil gas and radon entry rates to distinguish the contributions of advection from those of diffusion.

RADON EMANATION FROM CONCRETE

We begin by examining the concrete as a source of radon in the structure.

Theory

Because the walls (and floor) have far greater areal extent than thickness, we can consider diffusion from the concrete as a one dimensional problem (see Figure A-1). We use a coordinate system with its origin in the middle of the concrete. The concrete thickness is 2w and the concentration is assumed to be zero at x = w and -w.

The flux of radon through a cross sectional area of concrete is governed by Fick's law

$$F_c = -\varepsilon D_{c,e} \frac{dC}{dx} , \qquad (1)$$

where F_c (Bq m^{-2} s^{-1}), $D_{c,e}$ is the effective diffusion coefficient of radon in concrete that relates the gradient of the interstitial radon concentration to the flux across the pore area, ε is the air-filled porosity of the soil (air-filled volume/total volume), and C is the activity concentration of radon in the pore space (Bq m^{-3}).

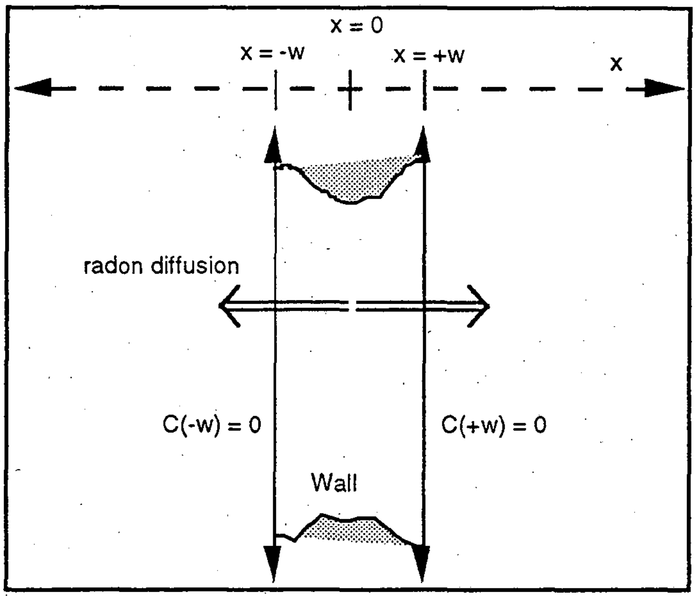

Figure A-1. Geometry of radon diffusion from wall.

In steady-state, the ^{222}Rn activity entering a volume element of concrete in time Δt by diffusion and by decay of ^{226}Ra will equal that leaving by diffusion and by decay of ^{222}Rn. The volume element of concrete is given by $A_c\Delta x$, the cross-section area of the volume element perpendicular to the flux time the length of the volume element. If f is the emanation fraction (the fraction of generated radon that ends it recoil in the pore space and is therefore free to diffuse), fG is the rate at which radon is generated per unit of pore volume (Bq m^{-3} s^{-1}), and λ is the decay constant of ^{222}Rn (Bq/s), then the steady-state activity balance can be written:

(2)
$$F_c(x)A_c\Delta t + fG[\varepsilon A_c\Delta x]\Delta t = F_c(x+\Delta x)A_c\Delta t + \lambda C[\varepsilon A_c\Delta x]\Delta t\ .$$

Substituting Eq. 1 for F_c and rearranging terms gives the governing equation for the concentration of radon in the concrete:

(3) $$\frac{d^2C}{dx^2} - \frac{\lambda C}{D_{c,e}} + \frac{fG}{D_{c,e}} = 0 \ .$$

Using the concept of a decay length for radon in concrete

(4) $$L = \sqrt{\frac{D_{c,e}}{\lambda}} \ ,$$

Eq. 3 can be rewritten

(5) $$\frac{d^2C}{dx^2} - \frac{C}{L^2} = -\frac{fG}{D_{c,e}} \ .$$

This non-homogeneous ordinary differential equation is readily solvable using the method of undetermined coefficients [1], yielding

(6) $$C(x) = \frac{fGL^2}{D_{c,e}} \left(1 - \frac{\cosh\left(\frac{x}{L}\right)}{\cosh\left(\frac{w}{L}\right)} \right) \ .$$

From Eq. 1, the flux at the wall is given by

(7) $$F_c\Big|_{x=w} = -\varepsilon D_{c,e} \frac{dC}{dx}\Big|_{x=w} \ .$$

Substituting Eq. 6 into Eq. 7, the flux of ^{222}Rn at the surface of the wall due to the content of ^{226}Ra in the concrete is:

(8) $$\boxed{F_c = \varepsilon fGL \tanh\left(\frac{w}{L}\right)} \ .$$

Results

Gamma spectroscopy measurements were made to determine the ^{238}U content of four concrete samples, two from the east structure and two from the west structure.* These samples were slices of cores taken from the north walls of each structure. (The holes remaining after the cores were removed were used as points of entry for conduits that contain sampling lines that pass between the structures and the trailer holding the detectors and other instrumentation.) Gamma spectroscopy was also used to determine the emanation fractions of the samples. The analysis assumes secular equilibrium between ^{238}U and its progeny under the measurement conditions. That is, it is assumed that the parent and progeny all have equal activity concentrations ([2], Ch. 15). The results are given in Table A-I.

Table A-I. Uranium content and emanation fraction of concrete core samples.

Core ID	Structure	$^{238}U_{tot}$ (ppm)	f
Core 2	west	2.15±0.05	0.11
Core 3	west	2.37±0.04	0.10
Core 1	east	2.13±0.05	0.094
Core 4	east	2.24±0.05	0.10
Average		2.24±0.02[a]	0.1

[a] Weighted arithmetic mean ± standard error of the mean.

The small range of values for the uranium contents and emanation fractions of all of the samples indicates that the concrete can be considered homogeneous for our purposes. We therefore use the average value of ^{238}U content of 2.2 ppm (by weight) and an emanation fraction of 0.1.

From these data, the radon source term for the concrete (G) can be determined. ^{222}Rn atoms are being generated at the same rate at which ^{226}Ra atoms are decaying. If N_{Ra} is the number of ^{226}Ra atoms per gram of concrete, then $N_{Ra}\lambda_{Ra}$ is the number of ^{222}Rn atoms generated per gram of concrete per second. The activity density of ^{238}U, $N_U\lambda_U$ (Bq/g-concrete), can be calculated from the data in Table A-I given the half life of ^{238}U (λ_U) of 4.47×10^9 yr, and the relationship that

---

* All gamma spectrometry measurements were performed by Al Smith at Lawrence Berkeley Laboratory, Earth Sciences Division.

(9) $$\lambda = \frac{\ln 2}{T_{1/2}},$$

where $T_{1/2}$ is the radioactive half life. The ^{238}U activity density is

(10) $$\left(\frac{2.2\ \text{g}\ ^{238}\text{U}}{10^6\ \text{g - concrete}}\right)\left(\frac{6.022\text{x}10^{23}\ \text{atoms}\ ^{238}\text{U}}{238\ \text{g}\ ^{238}\text{U}}\right)\left(\frac{\ln 2}{4.47\text{x}10^9\ \text{yr}}\right)\left(\frac{\text{yr}}{3.15\text{x}10^7\ \text{s}}\right)$$
$$= 2.74\text{x}10^{-2}\ \frac{\text{Bq}}{\text{g - concrete}}\ .$$

But, secular equilibrium between ^{238}U and ^{226}Ra in the concrete requires that

(11) $$N_U\lambda_U = N_{Ra}\lambda_{Ra}\ ,$$

which is also equal to the rate at which ^{222}Rn atoms are being generated per gram of concrete. The ^{222}Rn radon activity density is, therefore:

(12) $$\lambda_{Ra}N_{Ra}\lambda_{Rn} = 5.75\text{x}10^{-8}\ \frac{\text{Bq}}{\text{s g - concrete}}\ .$$

Multiplying by the measured density of concrete ($2.4\text{x}10^6$ g m^{-3}) gives the radon source per unit volume of concrete (G_C); and dividing by the porosity gives the radon source per unit pore volume (G):

(13) $$\varepsilon G = G_c = 0.138\frac{\text{Bq}}{\text{s m}^3}\ .$$

Substituting Eq. 13 into Eq. 8, gives

(14) $$\boxed{F_c = fG_cL\tanh\left(\frac{w}{L}\right)}\ .$$

The last parameter that is required to estimate the emanation of radon from the wall is L, the diffusion length of radon in concrete. Nero and Nazaroff [3] site values between 0.1 and 0.3 m. Stranden [4] cites values between 0.06 - 0.2 m. Using the full range of these values and Eq. 8 to determine a range of possible diffusive fluxes, we get

(15) $$F_c = \begin{cases} 2.07\text{x}10^{-4} & \text{for } L = 0.06 \\ 1.01\text{x}10^{-3} & \text{for } L = 0.3 \end{cases} \quad \left(\frac{\text{Bq}}{\text{m}^2\text{s}}\right).$$

Using the average of the upper and lower limits on the activity flux densities (Eq. 15), and given a concrete area in the structure of 26 m^2, the total diffusive emission from the concrete is estimated to be

(16) $$\boxed{S_c = 1.6\text{x}10^{-2}\,\frac{\text{Bq}}{\text{s}} = 57\,\frac{\text{Bq}}{\text{hr}}}.$$

^{222}RN FLUX THROUGH THE WALLS AND FLOOR

Charcoal canister measurements were made of the diffusive flux of ^{222}Rn from the interior of the east structure. These measurements yield the net flux of radon diffusing through the concrete from the soil and from the concrete itself. The east structure was used for these measurements instead of the west structure, on which the other experiments described in this dissertation were conducted, because we did not want to disturb experiments underway in the west structure. This should not result in large errors since the structures were designed to be identical except for the presence or absence of a subslab gravel layer, and because the undisturbed radon concentrations around the two structures are similar. Furthermore, the presence or absence of the gravel layer should not have a significant effect on the results of these measurements since they were conducted under nonadvective conditions.

Six sampling pans,[1] containing two charcoal sampling canisters each, were sealed to the walls and floor of the structure in the following locations: two on the east wall, one near the top and one near the floor; two similarly placed on the west wall; and two on the floor, one near the north wall and one near the south wall. The samplers are designated ET, EB, WT, WB, FN, and FS, respectively. They were left in place for approximately 76 hours, with the structure hatch left open to maintain a neutral pressure. Because of radon sorption to the charcoal, the radon concentration in the air space of the pans remains nearly zero, thus maintaining a fixed concentration gradient across the wall.

---

[1] We used 8"(.20 m) diameter by 2"(0.05 m) high, circular cake tins made of aluminum.

The canisters were analyzed for their radon concentrations using gamma spectrometry. Given the sample collection time, the time between sampling and measurement, and the decay rate of radon sorbed on the charcoal, the diffusive fluxes at each of the locations were calculated. The results are given in Table A-II. Note that these measurements will reflect both diffusion from and through the wall.

To calculate the total diffusive flux through intact concrete and into the chamber, the average flux density in each of the regions was multiplied by the regional area and summed. The contribution from the floor was handled in the same way. The total diffusive flux through the concrete (S_W) is estimated to be

$$\boxed{S_w = 330\ \frac{Bq}{hr} = 0.092\frac{Bq}{s}} . \tag{17}$$

This value represents an estimate of the *maximum* contribution of radon diffusion from the walls and floor that can occur during a steady-state experiment since, during the canister measurements, the structure radon concentration is effectively zero and soil-gas radon concentrations are not depleted as they would be during a depressurization experiment.

Table A-II. Diffusive radon fluxes from the interior walls of the east structure.

Sampler	^{222}Rn flux (Bq m^{-2} s^{-1})
ET	2.74 (± 0.01) x10^{-3}
WT	1.88 (± 0.02) x10^{-3}
EB	4.01 (± 0.05) x10^{-3}
WB	4.00 (± 0.05) x10^{-3}
FN	4.17 (± 0.05) x10^{-3}
FS	4.44 (± 0.04) x10^{-3}

DIFFUSION THROUGH THE SLOTS

Another source of diffusive entry of radon during advection experiments is through the slots themselves. Again, the flux F is estimated from Fick's law. Given the area, A, of the slots, the source [in Bq/s] is given by:

$$S_s = -AD_a \frac{\Delta C}{h} , \tag{18}$$

where ΔC is the concentration difference across the slots, h is the height of the slots (which is the same the thickness of the concrete slab), and D_a is the diffusivity of ^{222}Rn in air. The concentration difference across the slots, ΔC, is estimated from the concentration of ^{222}Rn in the structure, minus the concentration measured in the slots. This is only an approximation because the needles sampling slot air do not extend to the bottom of the slot (resulting in a possible underestimation of the flux). On the other hand, because we are estimating diffusive flux occurring during pressure-driven entry experiments, the average concentration gradient through the slots is not going to be as large as if entry were occurring by diffusion alone.

The values of the parameters in Eq. A-16 are as follows:

D_a = 1.2×10^{-5} m^2 s^{-1} (diffusion constant of ^{222}Rn in air) [5]
A = 1.92×10^{-5} m^2 (area of slots)
h = 0.15 m (thickness of the slab) .

Table A-III shows estimates of the diffusive source from the slots for different experiments, arranged in order of increasing structure depressurization. For comparison with estimates of diffusion from the concrete and through the walls, S_s is expressed in Bq/hr. The estimates of diffusion through the slots are uniformly small, approximately a factor of 100 smaller than diffusive entry through the walls, with all values less than 4 Bq/hr.

Table A-III. Estimation of ^{222}Rn Diffusion Through the Slot.

Experiment ID	Structure pressure [Pa]	Structure Rn [Bq/m^3]	Slot Rn [Bq/m^3]	S_s Diffusion across slots [Bq/hr]
BLW099	-9.4	38.3 x 10^3	80.6 x 10^3	3.9
BLW068	-18.0	37.3 x 10^3	53.5 x 10^3	1.5
BLW072	-18.0	35.0 x 10^3	63.3 x 10^3	2.6
BLW079	-21.1	45.6 x 10^3	61.2 x 10^3	1.4
BLW030	-70.3	35.3 x 10^3	49.7 x 10^3	1.3
BLW087	-65.1	38.5 x 10^3	57.2 x 10^3	1.7

SUMMARY AND CONCLUSIONS

Table A-IV compares the magnitudes of the different diffusive sources of radon entry and the radon entry rate by advection. Among the contributions of diffusion, diffusion through and from the wall is the largest source. Diffusion from the soil through the wall appears to the largest contribution, yielding an estimated 80% of radon emanating from the walls. Diffusion of radon through the cracks is negligible by comparison.

When compared to the advective contribution of radon during a typical 20 Pa structure depressurization experiment, all sources of diffusion are negligible. Under those conditions, radon entry by advection is at least 200 times larger than entry by diffusion via any pathway.

Table A-IV. Comparison of radon entry into the structure by advection and diffusion.

Source of Radon	Approximate Source Rate	
advection[a]	1.	Bq s^{-1} Pa^{-1}
diffusion through and from wall	0.09	Bq s^{-1}
diffusion from concrete	0.02	Bq s^{-1}
diffusion through slot	0.0009	Bq s^{-1}

[a] Estimated from Figure 2, Chapter 6, for depressurization < ~20 Pa.

REFERENCES

1. Ross, S.L., *Introduction to Ordinary Differential Equations,* John Wiley and Sons: New York, 1980.

2. Evans, R.D., *The Atomic Nucleus,* McGraw Hill: New York, 1955.

3. Nero, A.V. and Nazaroff, W.W., Characterizing the source of radon indoors, *Radiation Protection and Dosimetry,* 1984, 7: 23-39.

4. Stranden, E., Building materials as a source of indoor radon. In: *Radon and Its Decay Products in Indoor Air,* Nazaroff, W. W. and Nero, A. V. J., Ed. John Wiley and Sons: New York, 1988, 113-130.

5. Hirst, W. and Harrison, G.E., The diffusion of radon gas mixtures, *Proc. Roy. Soc. London (A),* 1939, 169: 573.

CHAPTER VII

Conclusions

> *The often quoted statement that soil is the complex product of the interaction of parent materials, climate, hydrology, relief and biological activity acting over time, glosses over the point that each of these soil factors may act over a different spatial scale, and that within each soil-forming factor there can be many spatial scales of interaction.*
>
> P.A. Burrough [1]

OVERVIEW

This chapter discusses the significance of the results of the work described in this dissertation. The work makes a contribution in two distinct areas. First, geotechnical assessment of soils is advanced by the capabilities of the new dual-probe dynamic pressure technique. Second, our understanding of radon entry into houses is advanced by the results of the studies carried out at the radon-transport test facility in Ben Lomond, California.

The material in this chapter is organized in the following manner:

- The first section summarizes the capabilities and significance of the new dual-probe dynamic pressure technique for measuring soil air-permeability.
- The second section discusses the resolution of the model-measurement discrepancies in radon and soil-gas entry at the Ben Lomond radon-transport test facility.
- The third section explores the implications of the finding of scale-dependent permeability of soil to air with regard to site assessment and modeling of the transport of gas-phase contaminants through soil.
- The last section discusses possible directions for future research.

THE DUAL-PROBE DYNAMIC PRESSURE TECHNIQUE

Chapters III and IV of this dissertation describe the development and testing of a new technique for measuring soil permeability to air, the dual-probe dynamic pressure (DPD) technique. The most important advance of this technique is its ability to make measurements over a significant range of length scales. An additional contribution of the current technique is that it allows unambiguous detection of anisotropy of permeability, because the source and detector probes can be placed in arbitrary locations.

The development of the DPD technique permitted the first comprehensive study and demonstration of the scale dependence of soil permeability to air in soils. The veracity of earlier findings of scale-dependent hydraulic conductivity in aquifers had been questioned because measurements at different length scales were made using different techniques (see conclusions of Bradbury and Muldoon [2]). A single earlier study which found scale dependence of vertical air-permeability from measurements performed at 3 different length scales in natural soil had the same limitation [3].

Using the DPD technique, I was able to make measurements over a range of length scales (0.5 – 3.5 m) with a single technique, thereby demonstrating unambiguously strong scale dependence of soil permeability to air over a relatively small range of scales (Chapter V). Furthermore, DPD measurements were found to be consistent with smaller-scale static measurements of permeability, given the observed scale dependence.

Although the scale dependence of permeability is now an accepted phenomenon in hydrogeology, it has not been a recognized issue in gas-phase transport through soils. The finding is important because it requires that we rethink our methods of site assessment, data interpretation, and modeling of the gas-phase transport of contaminants though soils.

RESOLVING THE MODEL-MEASUREMENT DISCREPANCY OF RADON ENTRY INTO HOUSES

The introduction to this dissertation pointed out that mathematical models consistently and significantly underpredict measured rates of soil-gas and radon entry into real houses. In the past, these discrepancies had been consistently attributed to a poor understanding of complex field sites. Experiments, described in Chapter II, confirmed the existence of the model-measurement discrepancy and generated a hypothesis about its source. Verification of the model-measurement discrepancy at the intensively monitored and carefully controlled experimental basement in Ben Lomond, California, indicated that the problem was deeper than a poor understanding of complex field sites. It indicated a problem with our conceptual model of soil that has resulted in misinterpretation of field assessments of contaminant transport potential and inaccurate representation in mathematical models.

The hypothesis derived from these experiments was that field assessments of soil permeability that are based on multiple small-scale (0.1 – 0.5 m) probe measurements underestimate effective permeability for flows that occur at the experimental basement (and are likely to occur at real houses) at a scale of ~several meters or more. Such empirical assessments of regional soil permeabilities are critical inputs to numerical transport models; a low input of soil permeability will result in a low prediction of radon entry rate. Reworded, the hypothesis claims that soil permeability to air depends on length scale.

A detailed investigation of the nature of soil air-permeability at the Ben Lomond field site found that soil permeability is strongly dependent on length scale (Chapter V). An independent confirmation of this finding was provided by model-measurement comparisons of soil-gas radon depletion with structure depressurization (Chapter VI).

In Chapter VI, the argument was made that, because of its geometry, the experimental structure must operate at a scale greater than ~2 m. A length scale of 3 m was selected, somewhat arbitrarily, as being representative of the structure's interaction with the soil. To obtain an approximate measure of the extent to which the finding of scale-dependent permeability resolves the model-measurement discrepancy in radon entry, the model was rerun given the 3-m-scale permeability as input. The results were compared with the original model simulations that used as input regional permeabilities based on averages of the smaller-scale (0.5 m) probe measurements. The new assessment of soil permeability reduced the model-measurement discrepancy in the soil-gas entry rate from a factor of ~9 to a factor of 2.5. It reduced the discrepancy in the radon entry rate from a factor or 7 to a factor of 1.5. The fact that measured pressure coupling in the soil adjacent to the structure continues to be considerably larger than the predicted value suggests that the remaining soil-gas-entry discrepancy may be due to enhanced flow occurring at the structure-soil interface.

The finding of scale-dependent permeability significantly resolves the model-measurement discrepancy of radon entry into the Ben Lomond test structure. It also holds the promise of significantly resolving the large discrepancies observed at real houses. That possibility will depend on a future finding that soils in general tend to have scale-dependent permeability between scales of about 10 cm to a few meters.

An additional complication in the resolution of the model-measurement discrepancy in real houses arises from the multiple factor that determine the scale at which a house interacts with the soil. Scale-dependent permeability will only resolve previous model-measurement discrepancies observed at real houses if the houses themselves do indeed interact with soils at scales larger than that at which the field permeabilities were determined (*i.e.*, the probe sampling scale). For field studies prior to the current work, that would tend to be at length scales ~ 0.1 m.[1] Factors that contribute to determining the length scale at which a house interacts with the soil include: the distance between the soil surface and the penetrations through which entry occurs, the geometry of the penetration(s), and the structure of the soil.

The actual operating scale of the system is not necessarily obvious. It is possible, for example, to have a large distance between the soil surface and the entry point into the building and still have a small effective scale for soil permeability. Consider the effective length scale if the penetration itself is small and the soil is homogeneous and in good contact with the building. In that case, the penetration itself would behave similarly to a small soil probe, with flow lines converging approximately radially to the entry point. That is, the effective sampling region, and hence the effective length scale, would be small. For identical soils, the larger the penetration, the larger the relevant length scale. In the case of the Ben Lomond west structure, the reason that the effective length scale was a large as it was is because of the presence of the gravel layer beneath the entry slots. This effectively enlarges the sampling region to the size of the structure floor.

---

[1] The cylindrical probe, having a integration length scale of ~0.5 m, was specially developed to have such a large effective sampling area for the studies conducted at the Ben Lomond Structures [4, 5].

This line of argument suggests that houses that possess a subsurface gravel layer will have increased radon entry rates not only because the gravel layer makes a larger effective source that drives entry [6], but because the size of that source makes the soil itself appear more permeable. The results presented in Chapter V proves that the latter effect can be large.

IMPLICATIONS FOR SITE ASSESSMENT AND MODELING

The finding of scale-dependent soil permeability to air suggests that both site assessment and modeling of radon transport will be more complicated and have greater uncertainty than was previously believed. For site assessment of contaminant transport potential to produce meaningful results, either the scale at which the system operates must be known *a priori* (which is unlikely in most circumstances) so that the system can be sampled at a single scale, or the site assessment must include an analysis of the scale dependence of permeability. Unfortunately, even if it is known how permeability changes with length scale, the problem is not solved. A model is still required to predict the transport of radon or other contaminants, given information about the soil structure, the geometry of the system, and the boundary conditions for flow and pressure. The best choice of an appropriate model is not immediately clear.

It is useful at this point to digress to a discussion of conceptual models of soils: how these models influence our interpretation of field data; and the implications of the finding of scale-dependent permeability for selecting among different types of models those that best reflect the nature of gas-phase transport through soils.

The dominant conceptual model of a heterogeneous soil represents the permeability field by a grid of randomly distributed representative elementary volumes (REVs), each with a well-defined homogeneous permeability. The implication of such a model is that an effective regional permeability can be inferred from a random sampling of spatially distributed measurements by taking some kind of average of the measurements, given some assumption (or measure) of the probability distribution.[2] Implicit in the data interpretation is the assumption that the sampling scale (*i.e.*, the effective integration area of the probe) is the same size as the REV. In other words, it is assumed that, at scales smaller than the sampling scale, the medium can be considered homogeneous; and that the behavior of fluid flow at larger scales can be inferred from the statistical properties of the data.

Yet, it is now clear that if the permeability of the medium is in fact scale dependent then any mean (arithmetic, geometric, harmonic) of the samples can reflect permeability only at the sampling scale. There is no possibility that information at larger (or smaller) scales is captured. In other words, the sampling scale uniquely determines the estimated permeability.

If permeability is in fact continuously scaling, then this suggests that the REV-grid concept of the soil itself fails since there is no scale at which the medium can be considered purely homogeneous.[3] This was also the conclusion of Neuman [8] in his theoretical investigation of the scaling of dispersivity and hydraulic conductivity in geologic media: "Since homogeneity is at best a local phenomenon limited to random and relatively narrow intervals of scale, one must question the utility of associating medium properties with representative elementary volumes (REVs) as has been the custom in subsurface hydrology for decades."

A newer class of models has emerged that treats porous media as a multiscale continua. These fractal models have been used to explore many aspects of fluid flow through porous media [9-14] and to describe observed spatial variability [1, 15, 16]. Wheatcraft and Tyler [17] and Neuman [8] have found that fractal models can successfully simulate dispersivity of contaminant flow through porous media. Menduni [18] has shown a fractal model successfully simulates scale dependence of permeability of fractured rock systems.

Although the scale-dependent permeability data from the Ben Lomond site (Figure 3, Chapter V) could be interpreted, by either a stochastic REV-type

---

[2] A typical assumption is that the REV permeabilities are distributed lognormally and therefore that the geometric mean of the measurements gives a measure of the effective regional permeability.

[3] For a discussion of the treatment of heterogeneous porous media using the REV-grid concept, see Dagan [7].

model or fractal model, the fractal models are conceptually appealing because their very nature incorporates scale dependence. The REV-type models must invoke spatially correlated statistical properties to produce scale dependence. In these models, scale dependence ceases beyond the correlation length scale, and is absent below the scale of the REV. In contrast, scale dependence is inherent in the structure of fractals, which are comprised of a continuum of scales of heterogeneity.

If root structures, animal burrows, and leaching channels are responsible for the observed scale dependence of heterogeneity, then fractal models appear to be a particularly desirable choice, since these structures are likely to have fractal-like form. Consider the root structures observed in the Ben Lomond soil down to several meters depth. Root systems appear to consist of a nested hierarchy of networks formed at different length scales. Roots having finer structures tend to branch at shorter distances than roots having heavier structures.

On the other hand, a real soil is probably not a perfect fractal structure. Logic dictates that the increasing scales of possibly fractal-like heterogeneity will discontinue at some upper limit of length scale (in the Ben Lomond soil that might be determined by the scale of the larger Oak tree roots). (In a perfect fractal system, the continuum persists up to infinite scale.) In addition, the nested scales of heterogeneity probably do not form a perfect continuum. One could imagine a system in which fast paths in the soil were dominated by grass and Oak trees roots each operating over a finite range of scales, and reaching down to different distances in the soil. The relevant question is: Which models capture the salient features of gas-flow through soils in a simpler fashion. The answer to this will require further study.

Based on this discussion, an obvious advantage of the dual-probe dynamic pressure technique for exploring the nature of the permeability field is that it does not lock the experimenter into an REV-grid interpretation of the data. The medium can be explored at arbitrary scale lengths (and orientations) to determine if there is some suitable volume which can be considered as a homogeneous representative volume element.

FUTURE RESEARCH DIRECTIONS

The work presented here suggests several profitable directions for future research. With regard to the dual-probe dynamic pressure measurements of soil permeability, it would be useful to develop a model for quantitative interpretation of field measurements in strongly anisotropic soils. There is currently no technique available that gives reliable quantitative assessments of anisotropy from *in situ* measurements. If such a model can be developed for the dual-probe measurements it will represent a significant advance in geotechnical assessment of soils. It will also offer the additional advantage that anisotropy could then be determined as a function of scale.

A second area of research is the investigation of the nature of soil structure that causes scale-dependent heterogeneity. It was suggested in Chapter V that scale-dependent permeability might result from the natural evolution of the soil structure due to the growth of plant roots, animal burrows, and the creation of cracks and channels by water movement and by the shrinkage and swelling of soils. This conjecture was supported by model-measurement comparisons of soil-gas radon concentrations in Chapter VI, which found a better fit of the model to measurements when the soil in the backfill-zone adjacent to the walls of the structure was assumed to have lower permeability than the surrounding natural soil. The backfill zone—having been seriously disturbed by soil removal and repacking during structure installation—may not have had the time for these scale-dependence-causing features to become fully developed.

Experiments to determine the nature of soil heterogeneity include correlating the magnitude and existence of scale-dependent permeability with observable surface features such as vegetation density and cover and soil cracking, and with data on soil-type, clay content, and rainfall. It would be particularly useful to conduct measurements of scale-dependent permeability in adjacent plots containing different vegetation and watering treatment.

To determine if soil-gas flow occurs preferentially along networks of preferred-flow channels in the soil, a gas injection experiment could be carried out with a strongly adsorbing tracer. Subsequent dissection and examination of the soil/root matrix could determine the regions of maximum exposure (*i.e.*, the dominant flow paths). Finally, if plant roots are determined to be an important factor in the generation of scale-dependent permeability, their morphology should be examined, for example, for fractal structure.

The most obvious need, with regard to future research in this area, is to determine the prevalence and magnitude of scale-dependent permeability in other soils. This task could be accomplished by using the dual-probe dynamic pressure technique to investigate other soils. Regarding the radon entry problem, it would be most profitable to study the soil around existing houses, and over the range of scales that houses are likely to interact with soils. It would be sensible to do so in areas where soils are sufficiently permeable that radon concentrations indoors are high enough to be of concern. If scale-dependent permeability is found to be prevalent in other soils at the magnitude at which it was observed at the Ben Lomond site, it will require that we reevaluate our designs both for site assessment and modeling gas-phase transport of contaminants in soils.

REFERENCES

1. Burrough, P.A., Multiscale sources of spatial variation in soil. I. The application of fractal concepts to nested levels of soil variation., *Journal of Soil Science*, 1983, 34: 577-597.

2. Bradbury, K.R. and Muldoon, M.A., Hydraulic Conductivity Determinations in Unlithified Glacial and Fluvial Materials. In: *Ground Water and Vadose Zone Monitoring*, Nielson, D. M. and Johnson, A. I., Ed. American Society for Testing and Materials: Philadelphia, 1990, 138-151.

3. Schery, S.D. and Siegel, D., The role of channels in the transport of radon from the soil, *Journal of Geophysical Research*, 1986, 91: 12366-12374.

4. Fisk, W.J., Flexser, S., Gadgil, A.J., Holman, H.Y., Modera, M.P., Narasimhan, T.N., Nuzum, T., Revzan, K.L., Sextro, R.G., Smith, A.R., Tsang, Y.W. and Wollenberg, H.A., *Monitoring and Modeling for Radon Entry into Basements: A Status Report for the Small Structures Project.* LBL-27692, Lawrence Berkeley Laboratory: Berkeley, CA: 1989.

5. Fisk, W.J., Modera, M.P., Sextro, R.G., Garbesi, K., Wollenberg, H.A., Narasimhan, T.N., Nuzum, T. and Tsang, Y.W., *Radon Entry into Basements: Approach, Experimental Structures, and Instrumentation of the Small Structures Project.* LBL-31864, Lawrence Berkeley Laboratory: Berkeley, CA: 1992.

6. Revzan, K. and Fisk, W., Modeling radon entry into houses with basements: The influence of structural factors, *Indoor Air*, 1992, 2: 40-48.

7. Dagan, G., *Flow and Transport in Porous Formations*, Springer-Verlag: Berlin, 1989.

8. Neuman, S.P., Universal scaling of hydraulic conductivities and dispersivities in geologic media, *Water Resources Research*, 1990, 26: 1749-1758.

9. Rieu, M. and Sposito, G., Fractal fragmentation, soil porosity, and soil water properties: I. Theory, *Soil Science Society of America,* 1991, 55: 1231-1238.

10. Rieu, M. and Sposito, G., Fractal fragmentation, soil porosity, and soil water properties: II. Applications, *Soil Science Society of America,* 1991, 55: 1239-1244.

11. Tyler, S.W. and Wheatcraft, S.W., Application of fractal mathematics to soil water retention estimation, *Soil Science Society of America Journal,* 1989, 53: 987-989.

12. Tyler, S. and Wheatcraft, S., Fractal processes in soil water retention, *Water Resources Research,* 1990, 26: 1047-1054.

13. Wheatcraft, S.W., Sharp, G.A. and Tyler, S.W., Fluid flow and solute transport in fractal heterogeneous porous media. In: *Dynamics of Fluids in Hierarchical Porous Media,* Cushman, J. H., Ed. Academic Press: London, 1990, 305-326.

14. Barton, C.C., Fractal scaling of fluid movement in fracture networks in rock. In: *1992 Fall Meeting of the American Geophysical Union.* San Francisco: American Geophysical Union, Washington DC, 1992 (December 7 - 11).

15. Burrough, P.A., Multiscale sources of spatial variation in soil. II. A non-Brownian fractal model and its application in soil survey., *Journal of Soil Science,* 1983, 34: 599-620.

16. Young, I. and Crawford, J., The analysis of fractal profiles in soil using fractal geometry, *Australian Journal of Soil Research,* 1992, 30: 291-295.

17. Wheatcraft, S.W. and Tyler, S.W., An explanation of scale-dependent dispersivity in heterogeneous aquifers using concepts of fractal geometry, *Water Resources Research,* 1988, 24: 566-578.

18. Menduni, G., Scaling permeability in fractured rocks, *EOS, Transactions of the American Geophysical Union*, 1992, 73: 214.

LAWRENCE BERKELEY LABORATORY
UNIVERSITY OF CALIFORNIA
TECHNICAL INFORMATION DEPARTMENT
BERKELEY, CALIFORNIA 94720